

March 2022

Soft Magnetic Composite Substrates for RF/Microwave Applications

Poonam Lathiya
University of South Florida

Follow this and additional works at: <https://digitalcommons.usf.edu/etd>



Part of the [Electrical and Computer Engineering Commons](#), [Materials Science and Engineering Commons](#), and the [Physics Commons](#)

Scholar Commons Citation

Lathiya, Poonam, "Soft Magnetic Composite Substrates for RF/Microwave Applications" (2022). *USF Tampa Graduate Theses and Dissertations*.
<https://digitalcommons.usf.edu/etd/10333>

This Dissertation is brought to you for free and open access by the USF Graduate Theses and Dissertations at Digital Commons @ University of South Florida. It has been accepted for inclusion in USF Tampa Graduate Theses and Dissertations by an authorized administrator of Digital Commons @ University of South Florida. For more information, please contact digitalcommons@usf.edu.

Soft Magnetic Composite Substrates for RF/Microwave Applications

by

Poonam Lathiya

A dissertation submitted in partial fulfillment
of the requirements for the degree of
Doctor of Philosophy
Department of Electrical Engineering
College of Engineering
University of South Florida

Major Professor: Jing Wang, Ph.D.
Sylvia Thomas, Ph.D.
Arash Takshi, Ph.D.
John N. Kuhn, Ph.D.
Dario Arena, Ph.D.

Date of Approval:
October 27, 2021

Keywords: Soft Magnetic Ferrites, Complex Permeability, Complex Permittivity, Resonance
Frequency, Patch Antenna, Reflection Coefficient

Copyright © 2022, Poonam Lathiya

Dedication

To my parents, husband, loving son, family and friends for their unwavering support and encouragement.

Acknowledgments

I would like to sincerely thank my advisor, Dr. Jing Wang, for providing constant support and guidance throughout my research. I have learned many lessons under his mentorship that would be helpful forever in my life. I am very grateful for the effort spent by my dissertation committee members Dr. Sylvia Thomas, Dr. Arash Takshi, Dr. John N. Kuhn and Dr. Arena Dario in helping me reach my goal.

Special thanks to my husband and my son Aavek for giving me strength and love throughout my PhD journey. I would like to thank my friends Gaurav Verma, Shruti Padhee, Debtanu Maiti, Harsha Vardhan, and Swamy Rakesh for their steadfast support throughout my life as a graduate student. Many thanks to all my colleagues in RF MEMS transducer group at USF.

To my parents and my family, thank you for your endless patience and encouragement throughout my life. I will forever be in your debt for your unconditional love, prayers and confidence in me.

Table of Contents

List of Tables	iv
List of Figures	vi
Abstract	xii
Chapter 1: Introduction and Background.....	1
1.1 Overview.....	1
1.2 Background and Literature	3
1.2.1 Wireless Communication Based on RFID and NFC	3
1.2.1.1 RFID	3
1.2.1.2 NFC.....	4
1.3 Magnetic Materials Consideration.....	7
1.3.1 Ni-Cu-Zn Ferrite for NFC.....	7
1.3.2 Ni-Co-Zn Ferrite for RFID and MICS Band	8
1.4 Magnetic Composite Substrates.....	10
1.5 Contributions.....	12
1.6 Organization.....	13
Chapter 2: Synthesis and Characterization of Soft Magnetic Ferrite Powders and Ferrite Composites	15
2.1 Introduction.....	15
2.2 Methods and Procedure for Ferrite Powder Synthesis.....	15
2.2.1 Ferrite Powder Synthesis Method.....	15
2.2.1.1 Ni-Cu-Zn Ferrite	17
2.2.1.2 Ni-Co-Zn Ferrite	18
2.3 Preparation of Magnetic Composite Sheets	19
2.3.1 Materials	19
2.3.1.1 MED-302-3M	19
2.3.2 Magnetic Composite Sheet Formulation	19
2.3.2.1 Tape Casting Technique	19
2.3.2.2 Compression Molding.....	20
2.4 Characterization	22
2.4.1 X-ray Diffraction	22
2.4.2 Scanning Electron Microscopy	22
2.4.3 RF/Impedance Analysis	22
2.5 Summary	23

Chapter 3: Microwave and Structural Properties of Ni-Cu-Zn Ferrite Powders	24
3.1 Note to Reader	24
3.2 Introduction.....	24
3.3 Effect of Sintering Temperature and Doping on Ni-Cu-Zn Ferrite Powder.....	25
3.3.1 Microstructure Characterization	25
3.3.1.1 X-Ray Diffraction (XRD) Analysis.....	25
3.3.1.2 Scanning Electron Microscopy (SEM) Analysis	26
3.3.2 Dynamic Magnetic Properties.....	28
3.3.3 Summary	31
3.4 Effect of Hydraulic Pressures at Different Sintering Temperature on Ni-Cu-Zn Ferrite Powders	32
3.4.1 Microstructure Characterization	33
3.4.1.1 X-Ray Diffraction (XRD) Analysis.....	33
3.4.1.2 Scanning Electron Microscopy (SEM) Analysis	33
3.4.2 Dynamic Magnetic Properties.....	36
3.4.3 Summary	40
3.5 Effect of Hydraulic Pressures and Durations on Ni-Cu-Zn Ferrite Powders.....	41
3.5.1 Microstructure Characterization	42
3.5.1.1 X-Ray Diffraction (XRD) Analysis	42
3.5.1.2 Scanning Electron Microscopy (SEM) Analysis	43
3.5.2 Dynamic Magnetic Properties.....	45
3.5.3 Summary	50
 Chapter 4: Microwave and Structural Properties of Ni-Co-Zn Ferrite Powders	 52
4.1 Note to Reader	52
4.2 Introduction.....	52
4.3 Effect of CuO on Ni-Co-Zn Ferrite Powders.....	53
4.3.1 Microstructure Characterization	53
4.3.1.1 X-Ray Diffraction (XRD) Analysis.....	53
4.3.1.2 Scanning Electron Microscopy (SEM) Analysis	56
4.3.2 Dynamic Magnetic Properties.....	58
4.3.3 Dielectric Properties.....	64
4.3.4 Summary	66
4.4 Effect of Cobalt Oxide (Co ₂ O ₃) Substitution on Ni-Co-Zn Ferrite Powders.....	67
4.4.1 Microstructure Analysis.....	67
4.4.1.1 X-Ray Diffraction (XRD) Analysis.....	67
4.4.1.2 Scanning Electron Microscopy (SEM) Analysis	68
4.4.2 Dynamic Magnetic Properties.....	69
4.4.3 Dielectric Properties.....	71
4.4.4 Summary	76
 Chapter 5: Ni-Co-Zn Composites Characterization and Their Application in Ultra High Frequency Antennas.....	 78
5.1 Introduction.....	78
5.2 Measured Microwave Properties of Ni-Co-Zn Ferrites and Ni-Co-Zn/Epoxy Composite Substrate	79

5.3 Theoretical Models for Effective Permeability and Permittivity of Ni-Co-Zn/Epoxy Soft Magnetic Composites	82
5.3.1 Bruggeman Mixture Equation.....	82
5.3.2 Maxwell-Garnett Mixture Equation.....	83
5.3.3 QCA-CP Mixture Equation.....	83
5.3.4 Lichtenecker Mixture Equation	83
5.3.5 Logarithm Mixture Equation	83
5.4 Comparison Between Measured and Calculated Effective Microwave Properties of Ni-Co-Zn/Epoxy Composite Substrate	84
5.5 Design, Fabrication and Characterization of Microstrip Patch Antennas for Ultra High Frequency Band (MICS Band)	88
5.5.1 Parametric Analysis for the Design of Patch Antennas	88
5.5.1.1 Figure of Merit and Measurement Techniques.....	90
5.5.2 Simulations and Design of Microstrip Patch Antenna Using Dielectric and Magnetic Composite Substrates	90
5.5.3 Fabrication and Measurement of Microstrip Patch Antenna Using the Dielectric Core of RO3010 Laminate and Magnetic Composite (Ni-Co-Zn/Epoxy-47 Vol%) Substrate	95
5.5.3.1 Dielectric Substrate (Rogers RO3010) Patch Antenna Results.....	97
5.5.3.2 Magnetic Composite Substrate (Ni-Co-Zn/Epoxy) Patch Antenna Results	99
5.5.3.3 Comparison in Performance between Dielectric Substrate (Rogers RO3010) and Magnetic Composite Substrate (Vol 47%) Antennas.....	101
5.5.4 Effect of Substrate Thickness and Material Properties on the Performance of Dielectric Substrate and Magnetic Composite Substrate Patch Antennas	103
5.5.4.1 Dielectric Substrate (RO3010) Antenna Performance with Varied Substrate Thickness.....	103
5.5.4.2 Magnetic Antenna Performance with Varying Substrate Thickness	105
5.5.4.3 Effect of Ferrite Volume Loading on Performance of Magnetic Composite Antennas	107
5.6 Summary	109
Chapter 6: Conclusion and Future Work	111
6.1 Conclusion	111
6.2 Future Research	112
References.....	115
Appendix A: Copyright Permissions	125

List of Tables

Table 1-1 RFID frequency bands and ranges	4
Table 2-1 Physical properties of MED-302-3M epoxy	19
Table 3-1 Real and imaginary parts of complex permeability, magnetic loss tangent, Q-factor and resonance frequency of ferrite samples at 13.56 MHz	30
Table 3-2 Bulk densities and grain size parameters of the toroidal NiCuCoZn ferrite samples that were pressed manually during the compression molding process but sintered at different temperatures	35
Table 3-3 The comparisons of the complex permeability, magnetic loss and Q-factor at 13.56 MHz for test specimens prepared by using varied sintering temperatures and hydraulic pressures	38
Table 3-4 Different toroidal samples pressed under different hydraulic force levels and different durations	42
Table 4-1 X-ray density, d-spacing, lattice constant, average crystallite size, and porosity of $\text{Ni}_{0.4}\text{Co}_{0.25}\text{Zn}_{0.35}\text{Fe}_2\text{O}_4$ samples sintered at 1100 °C for 2 hours for x= 0 wt% to 20 wt%	56
Table 4-2 Bulk density and grain size of $\text{Ni}_{0.4}\text{Co}_{0.25}\text{Zn}_{0.35}\text{Fe}_2\text{O}_4$ samples sintered at 1100 °C, 2 hours for different CuO concentrations (x= 0 wt% to 20 wt%)	58
Table 4-3 Fitted parameters extracted from the $\text{Ni}_{0.4}\text{Co}_{0.25}\text{Zn}_{0.35}\text{Fe}_2\text{O}_4$ samples for x= 0 wt% to 20 wt%	63
Table 4-4 Magnetic and dielectric properties of $\text{Ni}_{0.4}\text{Co}_{0.25}\text{Zn}_{0.35}\text{Fe}_2\text{O}_4$ samples sintered at 1100 °C for 2 hours for x= 0 wt% to 20 wt% measured at different frequencies	65
Table 4-5 Grain size of $\text{Ni}_{0.65-x}\text{Co}_x\text{Zn}_{0.35}\text{Fe}_2\text{O}_{4.1}$ samples sintered at 1100 °C, 2 hours for different Co_2O_3 concentrations (x= 0.10 to 0.25)	69
Table 4-6 Magnetic and dielectric properties of $\text{Ni}_{0.65}\text{Co}_x\text{Zn}_{0.35}\text{Fe}_2\text{O}_4$ samples sintered at 1100 °C for 2 hours for x= 0.10 to 0.25 measured at different frequencies	72

Table 4-7 Measured magnetic and dielectric parameters for all Co ₂ O ₃ doped samples (x=0.10 to 0.25) at 500 MHz	75
Table 5-1 Microwave properties of Ni-Co-Zn/Epoxy magnetic composite measured at 400 MHz	81
Table 5-2 Measured vs. model predicted properties of Ni-Co-Zn/Epoxy magnetic composites.....	86
Table 5-3 Patch antenna design parameters for devices over different substrates.....	91
Table 5-4 Antenna substrate properties.....	91
Table 5-5 Performance parameters for antennas designed based on dielectric core of a Rogers RO3006 laminate, dielectric core of a Rogers RO3010 laminate and Ni-Co-Zn/Epoxy substrate	95
Table 5-6 Performance parameters of dielectric (RO3010) antenna.....	99
Table 5-7 Performance parameters of magnetic composite (vol 47 %) antenna.....	100
Table 5-8 Measured parameters of dielectric substrate and magnetic composite patch antennas	102
Table 5-9 Performance parameters for dielectric substrate patch antennas of varied thickness.....	104
Table 5-10 Optimized performance parameters for 6 mm-thick dielectric substrate patch antennas.....	105
Table 5-11 Performance parameters of magnetic composite antenna of varied thickness.....	106
Table 5-12 Performance parameters of magnetic composite antenna with different Ni-Co-Zn ferrite particle loading volume fractions	108
Table 5-13 Summary of prior works reported in literatures and the present work for the magnetic composite antenna performance and microwave properties	108

List of Figures

Figure 1-1 Inductive coupling between transmitter and receiver coils.....	5
Figure 2-1 Synthesis steps for NiCuZn ferrite powder with solid state synthesis method.....	17
Figure 2-2 Solid-state synthesis for preparation of ferrite powders and test specimen.....	17
Figure 2-3 NiCuZn ferrite slurry with unsintered and sintered sheet.....	20
Figure 2-4 Ni-Co-Zn/Epoxy composite sheet preparation steps	21
Figure 2-5 Disc and squared shaped samples for the dielectric measurements.....	23
Figure 2-6 Toroidal shaped samples for magnetic measurements.....	23
Figure 3-1 X-ray diffraction patterns of $\text{Ni}_{0.33}\text{Cu}_{0.2}\text{Co}_{0.014}\text{Zn}_{0.456}\text{Fe}_{1.96}\text{O}_{3.94}$ powders sintered at (a) 1100 °C for doped (0.2 wt% Bi_2O_3 , red curve) and (b) undoped (no Bi_2O_3 , blue curve) samples.....	26
Figure 3-2 SEM images of NiCuCoZn ferrite sintered (a) doped, (b) undoped at 1100 °C and; (c) doped, (d) undoped at 1120 °C.....	28
Figure 3-3 Complex permeability spectra of NiCuCoZn ferrite sintered at 1100 °C (a) complex permeability, (b) magnetic loss tangent for doped and undoped sample and 1120 °C (c) complex permeability, (d) magnetic loss tangent for doped and undoped sample.....	29
Figure 3-4 Comparison of (a) complex permeability spectra and (b) magnetic loss of NiCuZn ferrite sintered at 1100 °C and 1120 °C for doped and undoped samples.....	31
Figure 3-5 XRD patterns of samples sintered at 1080 °C, 1100 °C and 1120 °C.....	33
Figure 3-6 Top-view SEM images of the surface of toroidal samples sintered at (a) 1080 °C, (b) 1100 °C and (c) 1120 °C	34

Figure 3-7 Cross sectional images of toroidal samples prepared under varied magnitude of hydraulic press and sintered at 1100 °C for 2 hours, including (a) sample prepared under a hydraulic pressure of 4 MPa; (b) sample prepared under a hydraulic pressure of 8 MPa; and (c) sample prepared under a hydraulic pressure of 12 MPa	36
Figure 3-8 Measured complex permeability spectra of NiCuCoZn toroidal samples sintered at 1080°C, 1100°C and 1120°C under different hydraulic pressures: a) complex permeability for samples sintered at 1080°C; (b) magnetic loss tangent for samples sintered at 1080 °C; (c) complex permeability for samples sintered at 1100 °C; (d) magnetic loss tangent for samples sintered at 1100 °C; (e) complex permeability for samples sintered at 1120 °C; and (f) magnetic loss tangent at 1120 °C	37
Figure 3-9 Dependence of complex permeability spectra on the varied sintering temperature at a fixed hydraulic pressure of 4 MPa: (a) real and imaginary parts of permeability; (b) magnetic loss tangent at different sintering temperatures including 1080 °C, 1100 °C and 1120 °C	38
Figure 3-10 Dependence of extracted Q-factor on the frequency, showing (a) measured Q-factors for specimens sintered at 1100 °C under different hydraulic pressures; (b) measured Q-factors for samples prepared under a fixed hydraulic pressure of 4 MPa along with different sintering temperatures.....	39
Figure 3-11 X-ray diffraction pattern of Ni _{0.35} Cu _{0.19} Zn _{0.46} Fe ₂ O ₄ powder	42
Figure 3-12 Cross-sectional SEM images of toroidal samples prepared under varied amplitude and duration of hydraulic press (a) sample prepared by manual press without hydraulic force applied; and three other samples pressed under 12 MPa hydraulic pressure for different durations: (b) pressed for 30 sec; (c) pressure applied for 2 min; (d) pressed for 5 min	43
Figure 3-13 Cross-sectional SEM images of toroidal samples prepared under varied amplitude and 30 seconds of applied hydraulic press (a) sample prepared by manual press without hydraulic force applied; (b) sample pressed under 8 MPa hydraulic pressure; (c) sample pressed under 12 MPa	44
Figure 3-14 The density data of different toroidal samples: (a) pressed under 12 MPa hydraulic pressure for different time durations; (b) pressed for 30 secs at different hydraulic pressures.....	45

Figure 3-15 Measured RF complex permeability spectra of NiCuZn ferrite toroidal samples: (a) complex permeability of samples pressed under applied hydraulic pressure of 4 MPa for different time durations (b) magnetic loss tangent for the 4 MPa pressed samples (c) complex permeability of samples pressed under applied hydraulic pressure of 8 MPa for different time durations; (d) magnetic loss tangent for 8 MPa pressed samples; (e) complex permeability of samples pressed under applied hydraulic pressure of 12 MPa for different time durations; (f) magnetic loss tangent for under 12 MPa pressed samples	47
Figure 3-16 Measured RF complex permeability spectra of NiCuZn ferrite toroidal samples: (a) complex permeability of samples pressed for 30 seconds under different applied hydraulic pressures (b) magnetic loss tangent for the 30 second pressed samples.....	48
Figure 3-17 (a) Real part of complex permeability versus varied hydraulic press duration under different hydraulic pressures applied; (b) imaginary part of complex permeability versus varied hydraulic press duration under different hydraulic pressures applied; (c) magnetic loss tangent versus hydraulic press duration under different hydraulic pressures applied; (d) Q-factor versus hydraulic press duration under different hydraulic pressures	49
Figure 4-1 XRD patterns of CuO (x=0, 1, 3 5, 10 and 20 wt%) doped Ni _{0.4} Co _{0.25} Zn _{0.35} Fe ₂ O ₄ ferrite ceramics sintered at 1100 °C for 2 hours	55
Figure 4-2 Variation of (A) lattice constant and average crystallite size in response to varied CuO concentrations; (B) X-ray density and bulk density with respect to CuO concentration for Ni _{0.4} Co _{0.25} Zn _{0.35} Fe ₂ O ₄ ferrite.....	55
Figure 4-3 SEM micrographs of CuO (x=0, 1, 3 5, 10 and 20 wt%) doped Ni _{0.4} Co _{0.25} Zn _{0.35} Fe ₂ O ₄ ferrite ceramics sintered at 1100 °C for 2 hours, including ferrite doped with CuO at varied levels: (A) x=0 wt% (undoped); (B) x=1 wt%; (C) x=3 wt%; (D) x=5 wt%; (E) x=10 wt%; (F) x=20 wt%	57
Figure 4-4 Relative complex permeability spectra of Ni _{0.4} Co _{0.25} Zn _{0.35} Fe ₂ O ₄ samples sintered at 1100 °C for 2 hours: (A) real part of complex permeability; (B) imaginary part of complex permeability; (C) magnetic loss tangent.....	59
Figure 4-5 Real part of permeability and magnetic loss tangent of Ni _{0.4} Co _{0.25} Zn _{0.35} Fe ₂ O ₄ samples sintered at 1100 °C for 2 hours with respect to CuO concentrations at different frequencies of: (A) 300 MHz; (B) 500 MHz; and (C) 800 MHz	59
Figure 4-6 Fitted complex permeability spectra of the Ni _{0.4} Co _{0.25} Zn _{0.35} Fe ₂ O ₄ samples with varied CuO dopant concentrations, where solid lines are fitting curves: (A) x= 3 wt%; (B) x= 5 wt%; (C) x= 20 wt%	62

Figure 4-7 Permittivity spectra of $\text{Ni}_{0.4}\text{Co}_{0.25}\text{Zn}_{0.35}\text{Fe}_2\text{O}_4$ samples sintered at 1100 °C for 2 hours: (A) dielectric permittivity; (B) dielectric loss tangent	64
Figure 4-8 Real part of permittivity and dielectric loss tangent of $\text{Ni}_{0.4}\text{Co}_{0.25}\text{Zn}_{0.35}\text{Fe}_2\text{O}_4$ samples sintered at 1100 °C for 2 hours with respect to CuO concentration at different frequencies: (A) 300 MHz; (B) 500 MHz; (C) 1 GHz.....	64
Figure 4-9 X-ray diffraction patterns of $\text{Ni}_{0.65-x}\text{Co}_x\text{Zn}_{0.35}\text{Fe}_2\text{O}_{4.1}$ ($x=0.10$ to 0.25) powders sintered at 1100 °C for 2 hours	68
Figure 4-10 SEM micrographs of $\text{Ni}_{0.65-x}\text{Co}_x\text{Zn}_{0.35}\text{Fe}_2\text{O}_{4.1}$ ($x=0.10$ to 0.25) powders sintered at 1100 °C for 2 hours	69
Figure 4-11 Magnetic properties of Co_2O_3 -substituted ($x= 0.10, 0.15, 0.18, 0.20$ and 0.25) $\text{Ni}_{0.65-x}\text{Co}_x\text{Zn}_{0.35}\text{Fe}_2\text{O}_{4.1}$ ferrite toroid samples versus frequency sintered at 1100 °C (a) real and imaginary part of permeability; (b) magnetic loss tangent	70
Figure 4-12 Real part of permeability and magnetic loss tangent of Co_2O_3 -substituted ($x= 0.10, 0.15, 0.18, 0.20$ and 0.25) $\text{Ni}_{0.65-x}\text{Co}_x\text{Zn}_{0.35}\text{Fe}_2\text{O}_{4.1}$ ferrite toroid samples with respect to Co_2O_3 concentrations at different frequencies of: (A) 300 MHz; (B) 500 MHz; and (C) 800 MHz.....	70
Figure 4-13 Dielectric properties of Co_2O_3 -substituted ($x= 0.10, 0.15, 0.18, 0.20$ and 0.25) $\text{Ni}_{0.65-x}\text{Co}_x\text{Zn}_{0.35}\text{Fe}_2\text{O}_{4.1}$ ferrite toroid samples versus frequency sintered at 1100 °C (a) real part of permittivity; (b) dielectric loss tangent	73
Figure 4-14 Real part of permittivity and dielectric loss tangent of Co_2O_3 -substituted ($x= 0.10, 0.15, 0.18, 0.20$ and 0.25) $\text{Ni}_{0.65-x}\text{Co}_x\text{Zn}_{0.35}\text{Fe}_2\text{O}_{4.1}$ ferrite toroid samples with respect to Co_2O_3 concentrations at different frequencies of: (A) 300 MHz; (B) 500 MHz; and (C) 800 MHz	74
Figure 4-15 (a) Measured real part of permeability and permittivity spectra; (b) magnetic and dielectric loss tangent for $x=0.18$ doped sample versus frequency	75
Figure 4-16 (a) Measured real part of permeability and permittivity spectra; (b) magnetic and dielectric loss tangent at 500 MHz for all Co_2O_3 -substituted ($x= 0.10, 0.15, 0.18, 0.20$ and 0.25) $\text{Ni}_{0.65-x}\text{Co}_x\text{Zn}_{0.35}\text{Fe}_2\text{O}_{4.1}$ samples.....	75
Figure 4-17 Calculated normalized impedance and miniaturization factor of Co_2O_3 substituted ($x= 0.10, 0.15, 0.18, 0.20$ and 0.25) $\text{Ni}_{0.65-x}\text{Co}_x\text{Zn}_{0.35}\text{Fe}_2\text{O}_{4.1}$ samples at 500 MHz	76

Figure 5-1 Magnetic properties versus frequency of $\text{Ni}_{0.4}\text{Co}_{0.25}\text{Zn}_{0.35}\text{Fe}_2\text{O}_{4.1}$ ferrite toroid samples sintered at 1100 °C for 2 hours including: (a) real and imaginary part of permeability; (b) magnetic loss tangent	79
Figure 5-2 Dielectric properties versus frequency of $\text{Ni}_{0.4}\text{Co}_{0.25}\text{Zn}_{0.35}\text{Fe}_2\text{O}_{4.1}$ ferrite toroid samples sintered at 1100 °C for 2 hours including: (a) real and imaginary part of permittivity; (b) dielectric loss tangent	80
Figure 5-3 Magnetic and dielectric properties of $\text{Ni}_{0.4}\text{Co}_{0.25}\text{Zn}_{0.35}\text{Fe}_2\text{O}_{4.1}$ /Epoxy composite toroid samples including: (a) permeability; (b) magnetic loss tangent; (c) permittivity; (d) dielectric loss tangent	81
Figure 5-4 Real permeability and permittivity of $\text{Ni}_{0.4}\text{Co}_{0.25}\text{Zn}_{0.35}\text{Fe}_2\text{O}_{4.1}$ /Epoxy magnetic composites using different mixture models versus volume fraction at 400MHz: (a) real permeability; (b) real permittivity	85
Figure 5-5 Comparison between measured and calculated values of real permeability versus frequency for different volume fractions: (a) 0.33; (b) 0.47; (c) 0.66	85
Figure 5-6 Comparison between measured and calculated values of real permittivity versus frequency for different volume fractions: (a) 0.33; (b) 0.47; (c) 0.66	86
Figure 5-7 Schematic illustration of the key design parameters of a microstrip patch antenna	90
Figure 5-8 Schematic diagram of the microstrip patch antenna	92
Figure 5-9 Representative electric field distribution of the microstrip patch antenna.....	93
Figure 5-10 Simulated return loss vs. frequency for designed dielectric and magnetic patch antennas	93
Figure 5-11 Simulated E-Plane radiation patterns for patch antenna design 1, 2 and 3	94
Figure 5-12 Simulated H-Plane radiation patterns for patch antenna design 1, 2 and 3.....	94
Figure 5-13 Micrograph of a dielectric patch antenna designed and milled using Rogers RO3010 laminate as the substrate.....	96
Figure 5-14 Micrograph of the magnetic patch antenna using Ni-Co-Zn/Epoxy as the substrate	97
Figure 5-15 Micrograph of measurement set up for radiation pattern measurement of antenna	97

Figure 5-16 Simulated and measured return loss of custom-designed dielectric substrate patch antenna	98
Figure 5-17 (a) Comparison between simulated E-plane and H-plane radiation patterns and (b) comparison between simulated and measured E-plane radiation patterns for dielectric substrate patch antenna.....	99
Figure 5-18 Simulated and measured return loss of Ni-Co-Zn/Epoxy patch antenna.....	100
Figure 5-19 (a) Comparison between simulated E-plane and H-plane radiation patterns; and (b) comparison between simulated and measured E-plane radiation patterns.....	101
Figure 5-20 Measured return loss for dielectric substrate (RO3010) and magnetic composite substrate (Ni-Co-Zn/Epoxy) patch antennas	102
Figure 5-21 Simulated performance parameters including: (a) return loss; (b) gain and (c) efficiency of the dielectric substrate (RO3010) patch antenna at varied thickness.....	104
Figure 5-22 Simulated return losses for dielectric substrate (RO3010) before and after optimization of parameters.	105
Figure 5-23 Stimulated performance parameters including: (a) return loss; (b) gain and (c) efficiency of the magnetic composite Ni-Co-Zn/Epoxy patch antenna at varied thickness.....	106
Figure 5-24 Stimulated performance parameters including: (a) return loss; (b) gain; (c) bandwidth and (d) patch area of the magnetic composite Ni-Co-Zn/Epoxy patch antenna at different ferrite volume loading	107

Abstract

Novel soft magnetic ferrite materials will play a crucial role in next-generation over one trillion sensors (also known as “trillion sensor economy) related to 5G communications and internet of things, as these materials can achieve improved wireless power and signal transfer efficiency with high operation frequency. In this work, Ni-Cu-Zn and Ni-Co-Zn ferrites with high permeability, high permittivity, and low magnetic and dielectric losses were prepared for RF and microwave device applications. Frequency dispersion of RF complex permeability of Ni-Cu-Zn ferrites prepared under different applied hydraulic pressures and durations have been thoroughly investigated. The $\text{Ni}_{0.35}\text{Cu}_{0.19}\text{Zn}_{0.46}\text{Fe}_2\text{O}_4$ ferrites were prepared by conventional ceramic synthesis process. The obtained ferrite powders were pressed under different hydraulic pressures (4 MPa, 8 MPa, 12 MPa) over different durations (30 sec, 2min, 3min and 5 min). It was found that the complex permeability spectra change considerably with respect to the application of different hydraulic pressures and time duration. Porosity and grain size play an important role in affecting the permeability and magnetic loss tangent of the ferrite samples. A significant increase of the real part of the complex permeability from 96 to 139 is observed due to the application of hydraulic pressure of 12 MPa for 3 min as compared to a manually pressed sample. The magnetic loss tangent also increases from 0.01 to 0.02 as the imaginary part of the complex permeability increases, which is still acceptable for most of the wireless power transfer and wireless communication applications. It is postulated that the effect of elevated hydraulic pressure on ferrite powder-based composites increases the real part of permeability while influencing magnetic loss tangent less severely.

In this work, Ni-Cu-Zn and Ni-Co-Zn ferrites with high permeability and low magnetic loss were prepared and characterized for RF and microwave device applications. Composition and microstructure control is crucial to obtain the desired magnetic and loss properties. CuO and Co₂O₃ dopants were employed during the synthesis of Ni-Cu-Zn and Ni-Co-Zn ferrite specimens to modify the microstructures, thus improving the magnetic properties of the ferrites. High value of measured relative permeability (μ' of 4 -10) and relatively low magnetic loss tangent ($\tan\delta_m$ of 0.01- 0.1) has been achieved at frequency range between in high frequency (HF) and ultra-high frequency (UHF) ranges. Addition of CuO, especially up to 3 wt%, and Co₂O₃ up to 0.25 mole percent can cause a significant increase in permeability, while noticeable reduction in magnetic losses has been observed for the doped ferrite sample. The resonance frequency of synthesized ferrites has also been shifted into the GHz range, when higher concentration of CuO dopants (> 5 wt%) and lower concentrations of Co₂O₃ were employed.

Electromagnetic properties of Ni-Co-Zn/Epoxy magnetic composite substrates filled with different volume fractions of ferrite particles have been studied and were analyzed using different mixture models. Based on the properties of the Ni-Co-Zn/Epoxy magnetic composite substrates, a prototype antenna for MICS band (401 MHz - 406 MHz) have been designed by using 3D EM simulations by ANSYS/HFSS. Subsequently, the antenna design was implemented by compression molding method. The performance of the Ni-Co-Zn/Epoxy substrate based antenna was compared with the dielectric-only substrate antenna fabricated with a commercial microwave laminate (i.e., Rogers RO3010 with a permittivity $\epsilon_r=10.2$). A miniaturization of 16 % in patch antenna area and a 104% enhancement in antenna bandwidth along with an acceptable gain of 1.85 dBi has been achieved by the patch antenna implemented by Ni-Co-Zn/Epoxy magnetic substrate as compared to the reference design fabricated using the dielectric core layer of a Rogers RO3010 laminate.

Chapter 1: Introduction and Background

1.1 Overview

For decades, the soft magnetic materials have been proposed for radio frequency (RF) applications in different areas ranging from electronics to biomedical devices, miniaturization of devices, shielding from electromagnetic waves, and enhancement of antenna sensitivity and range. One such application of soft magnetic materials is wireless power transfer (WPT) technology [1]. This technology is based on the radio frequency identification tag (RFID) and has many applications, such as built-in wireless charging for the latest mobile phones, identity tags and access control, wearable medical sensors, and so on. One of RF applications is biomedical implants or wearable sensors, which requires use of RFID and Near Field Communication (NFC) based wireless power transfer [1]. As our population is growing older, there is strong demand in healthcare sector to come up with new innovative solutions. Thus, research on biomedical implantable diagnostic devices such as pacemaker, retinal implant, wearable sensors, electrocardiogram (ECG) recorders have gained attention [2]. With the advancement in RF technology, utilization of RF in biomedical devices is more widespread than ever before and overcome many associated challenges till now.

Several frequency bands are recommended by the Federal Communication Commission (FCC) for the biomedical devices, some of the most common frequency bands are 13.56 MHz, 433 MHz, 900 MHz, 2.45 GHz, 5.8 GHz ISM bands; 608-614 MHz, 1395-1400 MHz, and 1429-1432 MHz for wireless medical telemetry service (WMTS); 2360-2400 MHz for multiple body area network (MBAN); 413-419 MHz, 426-432 MHz, 438-444 MHz, 451-457 MHz for MedRadio

spectrum; and 401-406 MHz for medical implant communication service (MICS) band [3]. Wireless power transfer based on RFID and NFC have utilized most of these frequency bands. For biomedical implant wireless communications, 401- 406 MHz MICS band is most commonly used. The MICS band recommended by FCC has a decent bandwidth, while providing low interference and less attenuation of EM waves to the body. All these bands operate under high frequency (HF), very high frequency (VHF), ultrahigh frequency (UHF) over a wide microwave frequency range [1].

The main challenge in current biomedical devices is electromagnetic (EM) wave effects generated during communications at these high frequencies. For example, the absorption of EM waves and impedance mismatch of biological tissues with the devices led to the reduction of signal strength and power [1]. Other challenges in biomedical applications are miniaturization of device, improvement in usage of frequency range, and power consumption [3]. Considerable research has been conducted towards the miniaturization of biomedical RF and microwave devices. The key requirements of planar antennas used in biomedical devices to facilitate the proper wireless communication are biocompatibility, broad bandwidth, small size and proper shape [2]. It is well established that for antenna miniaturization high permittivity substrates are required that facilitates shortening of wavelength. For instance, Rogers RO3010 microwave laminates with high dielectric constant dielectric core that has a permittivity $\epsilon_r=10.2$. Miniaturization or size reduction of antenna using high permittivity dielectric substrates comes with reduction in bandwidth and degradation of performance that causes lower efficiency and impedance mismatch with the environment [4-7].

The use of magnetic materials with relative permittivity and permeability greater than unity can address these drawbacks and offer miniaturization along with the enhancement in antenna performance at the same time [8, 9]. To realize this, magnetic material with high permeability and

permittivity are desired and various synthesis parameters must be tuned to achieve desirable high permeability and high permittivity along with low magnetic and dielectric losses. In order to maximize the performance of the antennas, the material should have high permeability and low magnetic losses at the desired operating frequency range [10-12]. In this work, different synthesis conditions have been used to enhance the magnetic-dielectric properties (high permeability and permittivity along with low losses) of the magnetic materials, in order to utilize as magnetic composite substrate for antenna applications. Furthermore, magnetic substrates were fabricated with the optimized magnetic materials and a prototype planar antenna was designed. In the next section, background and literature for wireless communication using RFID and NFC is presented.

1.2 Background and Literature

1.2.1 Wireless Communication Based on RFID and NFC

NFC enables a subset of the Radio Frequency Identification (RFID) technology that works over a wide range of frequencies with three distinct bands — low, high, and ultra-high frequencies. The main difference between NFC and RFID technologies is their operating range. RFID operates in meters range, whereas NFC typically operates within three to five centimeters. [1] All RFID's operate based on the same principle of one-way data transfer from the tag to the receiver and there is no power transfer the other way around [13, 14]. Nevertheless, NFC can transfer data both ways even if the tag is passive.

1.2.1.1 RFID

RFID is one of the oldest technologies that utilize near field magnetic communication. RFID is utilized in various commercial areas such as automobile, agriculture, transport, medical system, payment cards, supply chain, tracking, identification application and short range interactions in the Internet of Things (IoT) [15, 16]. RFID system operates in different frequency

bands such as low frequency (LH), high frequency (HF), very high frequency (VHF), ultra-high frequency (UHF) and microwave frequencies all over the world. Frequencies band issued by government for different applications are- 30 KHz to 500 KHz, 3 MHz to 30 MHz, 300 MHz to 960 MHz and 2.45 GHz. Table 1-1 shows the RFID frequency bands and ranges. However, communications which require initialization at both ends (e.g., Peer-to-peer communication) cannot be supported by RFID technology. NFC is a solution to this shortcoming of RFID, which support peer-to-peer communications also.

Table 1-1 RFID frequency bands and ranges [1]. Permissions in Appendix A.

Frequency	Band	Range
LF	30 KHz to 500 KHz	≤ three feet
HF	3 MHz to 30 MHz	≤ six feet
UHF	300 MHz to 960 MHz	25+feet
Microwave	2.45 GHz	30+feet

1.2.1.2 NFC

NFC is a short-range wireless connectivity technology that operates at high frequency (HF) range with low bandwidth of radio waves mainly at 13.56MHz [17]. NFC comprises of three basic components - an antenna, a reader, and a tag. A reader (transmitter) sends a signal at the standard NFC frequency of 13.56 MHz and the tag antenna receives and processes the interrogation signal and respond with requested information back to the reader that is then interpreted and stored as the data [18].

The magnetic flux strength is inversely proportional to the square of the distance between the NFC device and the tag antenna. Hence, magnetic flux strength decreases quickly as the distance between the NFC device and the tag antenna increases, thus restricting the range and

effectiveness of NFC technology up to a few centimeters only [1]. Wireless power transfer (WPT) technique uses inductive coupling to transfer power wirelessly through the magnetic induction generated by paired coils (also known as loop antennas) [19, 20]. The frequency dispersion of RF complex permeability determines the efficiency of wireless power transfer [21]. For WPT systems, the insertion of a thin sheet made of soft magnetic ferrites between the transmit and receive coil antennas and metal case reduces the eddy currents generated on the metallic surface and extend the range of the magnetic fields, thus enhancing the power transfer efficiency [1]. To enhance the performance, a thin and flexible ferrite sheet of high permeability and low magnetic loss is desired [22].

In wireless communication both RFID and NFC works based on the principle of near field magnetic communication. This principle of inductive coupling is applied to all communications based on near field magnetism between transmitting and receiving devices. Figure 1-1 shows the simplified concept of inductive coupling [1]. When a primary coil generates alternating magnetic field, secondary coil which is placed in the vicinity of the primary coil inductively coupled with the primary coil and generates induced alternating magnetic field according to the Faraday’s law. This is the basic principle in transferring power wirelessly between the devices in near field region.

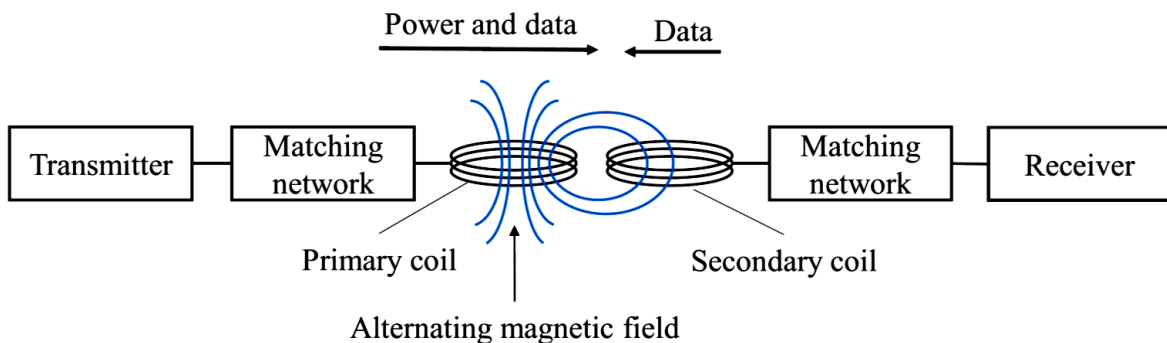


Figure 1-1 Inductive coupling between transmitter and receiver coils [1]. Permissions in Appendix A.

The inductive coupled NFC system can be modeled by using expressions of self-inductance, mutual inductance and resistances [23]. A generalized analytical expression for calculation of self-inductance of circular or rectangular shaped coil is explained below.

The inductance, L_0 , for a single turn circular coil can be given by equation (1) as seen below [24]

$$L_0 = \mu_0 r \ln\left(\frac{2r}{d}\right) \quad (1)$$

where μ_0 is permeability of free space, r is radius of the coil and d is the diameter of the wire. The single turn coil inductance can be utilized to calculate inductance of multiturn coil, L and is given by equation (2).

$$L = N^2 L_0 \quad (2)$$

$$L = N^2 \mu_0 r \ln\left(\frac{2r}{d}\right) \quad (3)$$

where N is number of turns in a coil. This equation provides appropriate approximation for a cylindrical inductor, but for the case of spiral inductor this equation provides general parameter studies. A detailed study for calculation of inductance of spiral inductors is provided by S. Alturi et al. (2004) [25].

Another important figure of merit is mutual inductance of two coupled coils. The mutual inductance between the two coils can be expressed in equation (4).

$$M = \frac{\mu \pi N_1 N_2 r_1^2 r_2^2}{2 \sqrt{(r_1^2 + x^2)^3}} \quad (4)$$

where, N_1 and N_2 are the number of turns in first and second coil, respectively, r_1 and r_2 are the radius of first and second coil, respectively, x is the axial separation and μ is the permeability.

1.3 Magnetic Materials Consideration

As RFID and NFC technology relies on generated mutual inductance between the transmit and receive coil antennas, the amount of magnetic flux between them should be maximized to induce more current, thus increasing data transmission range. However, by placing a NFC or RFID tag on a metal surface, the efficiency of data transmission is greatly suppressed due to the generation of eddy currents within the metal surface [21]. To increase the efficiency and range while minimizing the losses due to eddy currents, a soft magnetic ferrite sheet can be inserted between the metal case and the antenna. To be amenable to WPT, the ferrite sheets should have high permeability and low magnetic loss to concentrate the magnetic flux generated between the transmit and receive coils (antennas) [21, 26].

1.3.1 Ni-Cu-Zn Ferrite for NFC

Ni-Zn ferrites and Mn-Zn ferrites are the two most widely used materials for the preparation of these thin NFC sheets at high frequencies. Ni-Zn ferrites have exhibited a higher operating frequency range up to 100 MHz as compared to that of Mn-Zn ferrites of a few MHz, which limits the use of Mn-Zn ferrites in NFC devices only [27, 28]. Mn-Zn ferrites have been used in mini dc-dc converters, inductors and power inductors due to their high saturation induction and low losses. For NFC applications, Ni-Zn ferrites offer better suited properties because of its high resistivity, high permeability, low magnetic loss, high operation frequency, and chemical stability. In particular, the high permeability and low magnetic loss of Ni-Zn ferrite sheets help to concentrate more magnetic flux and reduces eddy currents via magnetic shielding. Copper oxide acts as sintering aid to lower the sintering temperature, thus promoting the grain growth and densify the microstructure [29]. Ni-Cu-Zn ferrites have exhibited promising soft magnetic properties for both low and high frequency applications at RF and microwave frequencies. The

magnetic properties of Ni-Cu-Zn ferrites can be tailored easily by further optimization of different synthesis parameters such as sintering temperature, Ni/Zn ratio, added dopants and porosity that can lead to more desirable morphology and microstructure of the material [27, 28]. In previous studies, efforts have been made in improving permeability and decreasing magnetic loss via variations of the chemical compositions; by varying the sintering processes such as low temperature sintering, double sintering; or by inclusion of additives like Bi_2O_3 , Co_2O_3 , V_2O_5 and B_2O_3 . Ni-Cu-Zn ferrite is in polycrystalline form, which can be densified at higher sintering temperatures. However, it is quite challenging to control the pore size and grain growth solely by the sintering temperature. Some studies also reported the effect of porosity and grain size on the magnetic properties of Ni-Cu-Zn ferrites by varying the concentrations and amount of binder burnouts in the ferrites [30]. During the formation of thin sheets, optimum amount of hydraulic force can be applied to achieve enhanced magnetic permeability while avoiding cracks in thin sheets. Hence, in this work, effects of hydraulic pressure were studied on structural and magnetic properties of Ni-Cu-Zn ferrites.

1.3.2 Ni-Co-Zn Ferrite for RFID and MICS Band

For wireless communication and information technology, soft magnetic materials, such as ferrites can offer high working frequencies along with tailored magnetic, dielectric and loss properties [31]. One of the most important soft magnetic materials is Ni-Co-Zn spinel ferrite, as it exhibits high permeability, low magnetic losses, chemical stability and high resistivity in the high frequency region well up to few 100 MHz [32]. In recent years, research has been focused on increasing the magnetic permeability, while reducing the losses and shifting the resonance frequency of these soft magnetic ferrites for operation at GHz frequencies [33]. To utilize these Ni-Co-Zn ferrite in practical applications, the requirements of the magnetic and dielectric

properties is diverse. Each device has different requirement of permeability and permittivity over different frequency range [34, 35]. With growing demand in devices, high values of permeability and permittivity together with low losses at higher frequencies are desired.

It is well established that a high sintered density, a large average grain size, a low porosity, and a stress-free grain boundary are the key governing microstructural parameters to achieve high permeabilities and low losses [36]. This was attributed to the fact that the complex permeability spectra is described by two different mechanisms, which are domain wall motion and spin rotation [37]. Domain wall motion is sensitive to both microstructure and sintered density of the ferrites in lower frequency range, while spin rotation contributes to the response at frequencies over 100 MHz and depends only on post-sintering density of the polycrystalline ferrites [31]. Also, in these ferrites, natural resonance exists due to effective anisotropy field, which results in magnetic losses [38, 39]. This restricts the utilization of these ferrites in radiofrequency devices known as the Snoek's limit, that is defined by equation 5 [40].

$$(\mu_i - 1)f_o = Constant \quad (5)$$

where, μ_i is initial permeability and f_o is resonance frequency. Various researches have been conducted for improving magnetic properties and raising of resonance frequency on spinel ferrites and hexaferrites using different dopants such as Cu substituted Ni-Zn ferrite [29, 41, 42], Ca and Cao-SiO₂ doped Ni-Co-Zn [43], Y and La doped Ni-Co-Zn ferrite [44], Co-Ti substituted M-type barium hexaferrite [45], Ir, ZnAl₂O₄, Ca and glass doped Co₂Z hexaferrite [46, 47] [48], and so on at radio frequency region. Ni-Co-Zn composition was chosen as cobalt oxide in spinel lattice of Ni-Zn helps in reducing core loss and contributes to the enhancement of the magneto crystalline anisotropy, thereby achieving better dynamic magnetic properties [49]. It is hypothesized that

migration of cobalt ions in spinel lattice stabilizes the magnetic domain walls because of induced anisotropy.

Copper oxide acts as sintering aid to lower the sintering temperature, thus promoting the grain growth and densify the microstructure [29]. There is no prior report on copper oxide (CuO) doped Ni-Co-Zn ferrite. Previous studies showed that the addition of copper oxide in Ni-Zn ferrites could tune the magnetic properties, hence permeability and magnetic losses can be tailored [49]. It is noteworthy that, in Ni-Co-Zn spinel structure, both Co^{2+} ions and Ni^{2+} ions have inverse spinel structure, which prefer B lattice (octahedral site) while Zn^{2+} ions are a normal spinel structure and prefers A lattice (tetrahedral site) [50]. As Cu^{2+} ions preferably reside at B site, doping the Ni-Co-Zn spinel ferrite by using CuO, it can replace both Ni^{2+} and Co^{2+} depending upon the amount of the CuO [28, 31]. In the present work, the effect of CuO concentration upon complex permeability and permittivity spectra as well as losses over 1 MHz to 1 GHz frequency range and on phase composition and microstructure has been carefully studied.

1.4 Magnetic Composite Substrates

To enhance the performance of wireless communication, the employment of high permeability, permittivity and low magnetic and dielectric loss substrate is highly desirable [28, 31]. The relation between the complex relative permeability and frequency is termed as permeability dispersion. The frequency dependent relative permeability is given by equation 6 [51],

$$\mu_r = \mu' - j\mu'' \quad (6)$$

where μ_r is the ratio of the permeability of the material versus that of the free space (μ_0). μ' and μ'' are real and imaginary parts of the relative permeability, respectively.

The magnetic loss tangent is the ratio between the real and imaginary parts given by equation 7

$$\tan\delta_m = \frac{\mu''}{\mu'} \quad (7)$$

The frequency dependent relative complex permittivity can be given by equation 8

$$\epsilon_r = \epsilon' - j\epsilon'' \quad (8)$$

where ϵ_r is known as relative permittivity and ϵ' and ϵ'' are real and imaginary parts of the complex permittivity.

The dielectric loss tangent is given by equation 9

$$\tan\delta_\epsilon = \frac{\epsilon''}{\epsilon'} \quad (9)$$

The size of the planar microstrip antenna which has been used in these frequency bands is directly proportional to the guided wavelength of the microstrip antenna which is given by equation 10 [52].

$$\lambda = \frac{c}{f\sqrt{\mu_{eff}\epsilon_{eff}}} \quad (10)$$

where, c is speed of light, f is frequency of the patch antenna, λ is guided wavelength of patch, ϵ_{eff} is effective permittivity and μ_{eff} is effective permeability.

It is evident from the equation, that size reduction of antenna can be done by using substrate with permeability and permittivity of greater than 1 [53-55].

For the bio medical implants and testing/diagnostic devices in HF and UHF bands, wireless communication is far field communication which is different from what is shown in Figure 1-1. For these applications, unless like NFC, there is no inductive coupling between transmitter and receiver antennas. The antennas utilized are planar antennas of different shape and sizes [22, 55-58]. For these frequency bands, a planar antenna is an antenna with metal patches on the top and

bottom of the dielectric substrate. To enhance the performance of the antenna and reduce antenna size, a magnetic material substrate is used instead of pure dielectric substrate in this work.

1.5 Contributions

In this Ph.D. work, novel ferrite materials have been synthesized and characterized for RF and microwave frequency applications.

- The main contribution of this work is the development of soft magnetic ferrite composite substrates for the miniaturization and bandwidth enhancement of microstrip patch antennas for RFID and NFC based biomedical devices.
- Bi₂O₃ doped Ni-Cu-Zn ferrite powders were synthesized under different sintering temperature profiles to achieve a high value of relative permeability (110 and 125) and low magnetic loss tangent (0.018 and 0.024) for targeted NFC applications at 13.56 MHz.
- Electromagnetic properties of Ni-Cu-Zn ferrite specimens were tested under different levels of hydraulic pressures and time durations. This parametric study helps elucidate the role of hydraulic pressure and press duration for improving magnetic properties of ferrite powder-based substrates for wireless power transfer applications at high frequencies (HF).
- CuO doped Ni-Co-Zn spinel ferrites with a wide range of CuO dopant concentrations from 0 wt% to 20 wt% have been prepared to achieve high permeability and permittivity along with low magnetic and dielectric losses for MICS band (401-406 MHz) antennas.
- Co₂O₃-substituted Ni-Co-Zn ferrites at very high frequency (VHF) and ultrahigh frequency (UHF) ranges have been studied to achieve high permeability and low dielectric losses for wireless communication applications at VHF and UHF frequency ranges.
- CuO doped Ni-Co-Zn/epoxy magnetic substrates have been fabricated and studied systematically by characterizing the electromagnetic properties of the magnetic substrates.

- Several mixture models have been used to evaluate the effective electromagnetic properties of the Ni-Co-Zn/epoxy composite magnetic substrate.
- To the best of my knowledge, first time CuO doped Ni-Co-Zn/epoxy magnetic substrates have been fabricated for biomedical antenna applications (e.g., wearable body networked devices). Evaluated the performance using sustained phonations for classification.
- A microstrip patch antenna on the Ni-Co-Zn/Epoxy magnetic composite substrate has been designed, fabricated, and characterized for the MICS band (401-406 MHz) applications.

1.6 Organization

This dissertation is organized into six chapters. The first chapter presents an overview and background of magnetic composites and their wireless power transfer (WPT) applications, with a special focus on usage of such materials in biomedical devices, such as wearable sensors and body networked devices.

In Chapter 2, synthesis methods of ferrite powders and ferrite/epoxy composites have been described in detail. Different characterization techniques to study the electromagnetic, morphology and microstructure properties of synthesized ferrite powders and magnetic composite sheets are also discussed.

In Chapter 3, the effect of bismuth oxide (Bi_2O_3), sintering temperature and hydraulic pressure on Ni-Cu-Co-Zn ferrite powders has been investigated for the near field communication (NFC) and wireless power transfer (WPT) applications. Optimized results in terms of magneto-dielectric properties are presented in this chapter.

In Chapter 4, the effects of CuO and Co_2O_3 as dopants in Ni-Co-Zn polycrystalline ferrites have been investigated for biomedical applications. Solid-state synthesis method is used for the synthesis of these doped powders. Subsequently, the effect of CuO or Co_2O_3 dopant concentration

upon complex permeability and permittivity spectra as well as losses over the frequency range of 1 MHz-1 GHz has been carefully studied. The effect of CuO or Co₂O₃ dopant concentration on the phase composition and microstructure have also been systematically studied and correlated with dynamic magnetic and dielectric properties.

In Chapter 5, the electromagnetic (EM) properties of magnetic composite substrates and theoretical modelling of magnetic and dielectric properties have been presented. The design and implementation of MICS band patch antennas based on soft magnetic ferrite composite substrates has been investigated.

In Chapter 6, future directions for further improving the properties of magnetic composites and perspective future improvements in design of antenna and other WPT devices using advance technology such as 3D printing (also known as additive manufacturing) have been discussed.

Chapter 2: Synthesis and Characterization of Soft Magnetic Ferrite Powders and Ferrite Composites

2.1 Introduction

The main goal of this chapter is to discuss synthesis and characterization methods of soft magnetic ferrite powders and ferrite composites prepared with a strategically chosen epoxy (302-3M). Synthesis of two different compositions: Ni-Cu-Zn and Ni-Co-Zn ferrites doped with different dopants such as bismuth oxide (Bi_2O_3), copper oxide (CuO), or cobalt oxide (Co_2O_3) are discussed in this chapter. Fabrication technique of magneto-dielectric composites composed of Ni-Co-Zn ferrites and epoxy is also presented. The microstructure of ferrite powders is analyzed with X-Ray diffraction (XRD) and scanning electron microscopy (SEM). Microwave properties such as magnetic and dielectric properties of the ferrite powders and magnetic composites are characterized up to 1 GHz frequency using commercial material test fixtures based on inductance measurement method and parallel plate method, respectively.

2.2 Methods and Procedure for Ferrite Powder Synthesis

2.2.1 Ferrite Powder Synthesis Method

Ni-Cu-Zn and Ni-Co-Zn ferrite powders were prepared via top-down approach in bulk quantity [59]. All the starting raw materials such as Fe_2O_3 , ZnO , CuO , Co_2O_3 and NiO in powder form were weighed according to their respective molecular weight percentages and wet mixed in DI water together via a planetary ball milling process for (exact time depends on the composition) hours. Ball milling method was used to mix and grind powders to small size as well as for reaction of individual chemicals to form structure. In this process powders were poured in stainless steel

container with grinding media (stainless ball) in dry or liquid condition. The optimal ball milling conditions (i.e., duration, ball media-to-particle ratio, and rotation speed) mainly depend on the targeted particle (grain) sizes; the longer the ball milling duration, the smaller the particle (grain) sizes will be [60]. After drying the milled powders, calcination was conducted at high temperatures in a temperature controlled furnace, typically at 800 °C to 950 °C, depending on the temperature of the subsequent sintering step at a heating rate of 10 °C per minute. The calcinated powders were then doped with 0.2 wt% of Bi₂O₃ and milled in ball milling for number of hours. Bi₂O₃ act as a sintering aid helps to lower the sintering temperature, thus resulting in better magnetic properties of ferrites. The doped powders were mixed with 5 to 10 weight percent of polyvinyl alcohol (PVA) binder to make toroidal (outer diameter of 8 mm, an inner diameter of 3.1 mm and a height of 3 mm) and disc (diameter 15 mm and thickness 2 mm) shaped test specimens for microwave characterizations [28]. Finally, the compression molded specimens were sintered by a conventional sintering technique in a furnace under ambient air at sintering temperatures of 900 °C to 1200 °C for 2 hours. For the proper sintering and burning out of PVA, ferrite samples were heated at 500 °C for 2 hours and then temperature was increased to final sintering temperature. The heating ramp rate for sintering was 2 °C per minute and cooling was done at 10 °C per minute. These toroidal and disc shaped samples were used for the measurement of the complex permeability and permittivity to extract the real and imaginary parts, and magnetic and dielectric loss of the samples using a RF impedance analyzer and required test fixtures. There are many synthesis parameters that can affect the magnetic properties of the test samples. Results will be detailed subsequently in the next chapter. Flow chart for synthesis of Ni-Cu-Zn ferrite powders is shown in Figure 2-1. Fig. 2.2 shows the pictures of ball milled machine, ferrite powders and test specimens made of synthesized Ni-Cu-Zn ferrite powders.

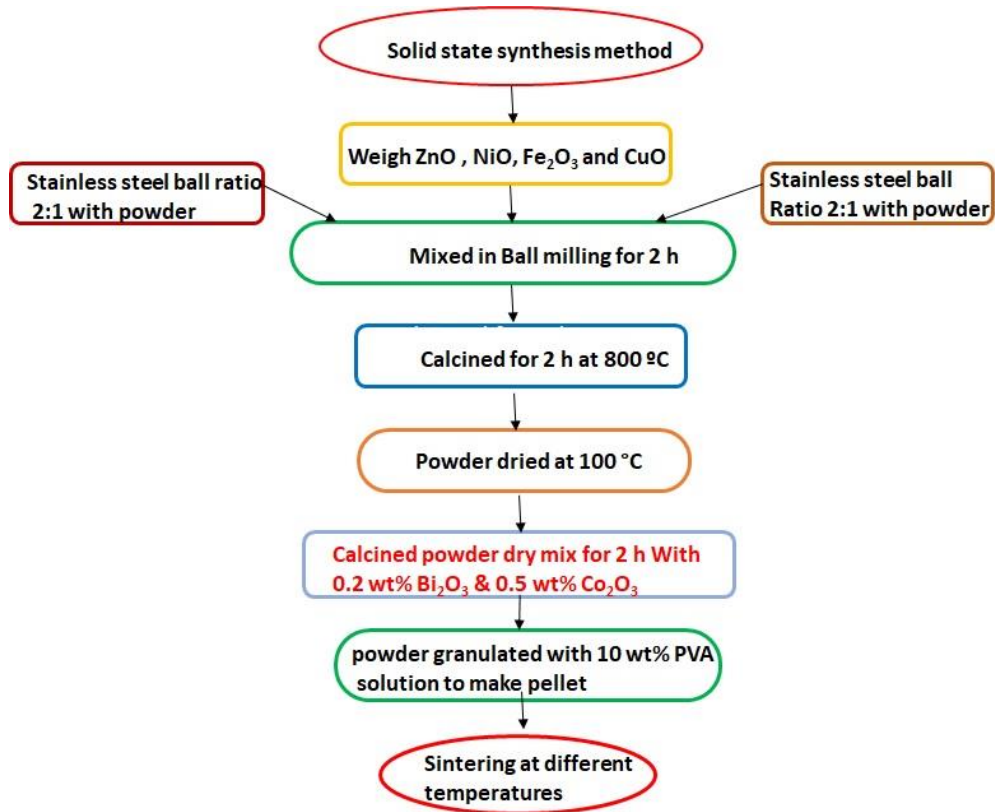


Figure 2-1 Synthesis steps for NiCuZn ferrite powder with solid state synthesis method.

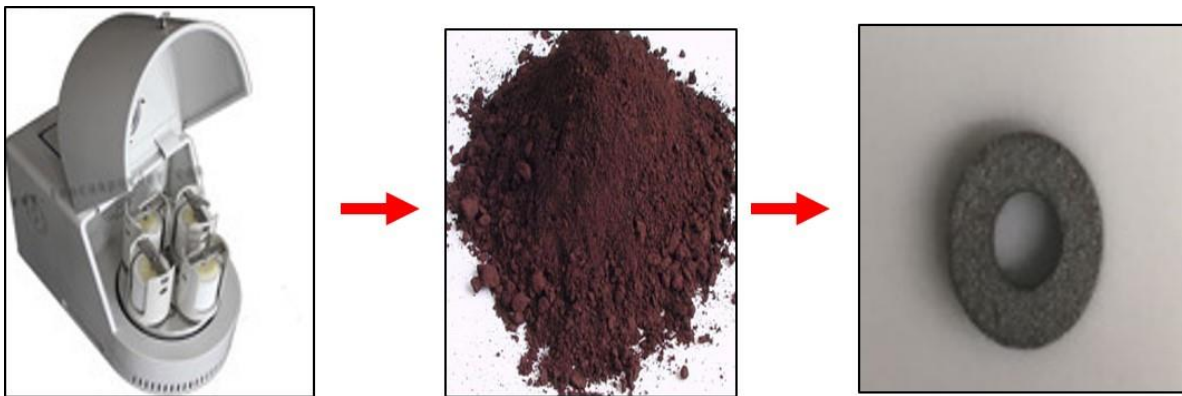


Figure 2-2 Solid-state synthesis for preparation of ferrite powders and test specimen.

2.2.1.1 Ni-Cu-Zn Ferrite

Ni-Cu-Zn ferrites were prepared by solid state synthesis method [60]. All constituent raw powder materials (Fe_2O_3 , ZnO , CuO , NiO) were weighed according to their respective molecular weight percentages. All powders were wet milled together in a planetary ball mill for 2 hours with

a milling speed of 560 rpm. The powder-ball-distilled water ratio of 1: 2: 2.5 was used for the powder mixture. After drying the milled powders, calcination was done at 800 °C for 2 hours. The powders were doped with 0.2 wt% Bi₂O₃ and 0.5 wt% Co₂O₃ and dry milled at 560 rpm. The resultant fine powders were then, granulated along with 10wt% PVA (Polyvinyl Alcohol) binder to prepare toroidal test samples of an outer diameter of 8 mm, an inner diameter of 3.1 mm, and a height of 3 mm under different levels of hydraulic pressure (0 MPa, 4 MPa, 12 MPa and 16 MPa). Before complex permeability measurements, all the toroidal samples were sintered in the air at 1100 °C for 2 hours.

2.2.1.2 Ni-Co-Zn Ferrite

The Ni_{0.4}Co_{0.25}Zn_{0.35}Fe₂O₄ ferrite powders were synthesized using conventional solid-state synthesis method [31]. Commercially available analytical grade oxides were used. Stoichiometric amounts of oxides, including NiO, ZnO, Co₂O₃ and Fe₂O₃ (phase purities > 99%), were weighed according to the composition. All the powders were mixed by using a Retsch planetary ball milling tool for 6 hours along with deionized (DI) water. Thereafter, drying was done on a hot plate at 100 °C for 1 hour. The dried powders were calcined at 950 °C for 2 hours at a ramp rate of 10 °C per minute. The calcinated powders were doped with 0.2 wt% of Bi₂O₃ and different wt% of CuO, respectively. These samples were subsequently dry milled at 560 rpm for 2 hours. The resultant fine powders were then, granulated along with 5 wt% Polyvinyl Alcohol (PVA) binder to prepare toroidal test specimens of an outer diameter of 8 mm, an inner diameter of 3.1 mm, and a height of 3 mm. All the toroidal samples doped with CuO were sintered for 2 hours under an ambient air atmosphere at 1100 °C.

2.3 Preparation of Magnetic Composite Sheets

2.3.1 Materials

For the preparation of ferrite/epoxy composites, doped ferrite powders were used in epoxy matrix. Different volume percentages of ferrite powder in epoxy matrix were investigated to study the optimum magnetic and dielectric properties of the ferrite composites.

2.3.1.1 MED-302-3M

EPO-TEK MED-302-3M is a two-component epoxy used for biomedical, optics and electronics industry. It is biocompatible and has low viscosity which can be cured at 80 °C for 2 hours or at room temperature for 24 hours. Due to its bio compatibility, high dielectric constant 3.39 and low dielectric loss tangent 0.006, this epoxy is chosen as a matrix in the ferrite composite.

Table 2.1 shows the physical properties of 302-3M epoxy from manufacturer.

Table 2-1 Physical properties of MED-302-3M epoxy

Properties	Value
Viscosity	800-1600 cPs
Dielectric Constant	3.39
Dielectric Loss	0.006
Glass Transition Temp.	> 55 °C
Curing Temp.	80 C for 2 hours

2.3.2 Magnetic Composite Sheet Formulation

Ferrite/epoxy composite was formed using two different techniques: compression molding and tape casting technique.

2.3.2.1 Tape Casting Technique

In tape casting, a doctor blade coater (also known as tape caster) is used to fabricate flexible thin ferrite sheets. Figure 2-3 thin Ni-Cu-Zn ferrite sheet synthesized using doctor blade coater. There are two ways to use the doctor blade, known as the stationary blade-moving carrier setup

and the stationary carrier-moving blade setup. We used stationary carrier configuration of the doctor blade coater. A typical feed slurry consists of ferrite powders and multiple additives such as plasticizers, binder, solvent and dispersants. To make the ferrite composite sheet, polyvinyl alcohol as a binder; benzyl-n-butyl-phthalate as a plasticizer, polyethylene glycol and ethanol as a solvent was used.



Figure 2-3 NiCuZn ferrite slurry with unsintered and sintered sheet.

For this work, powder, binder, plasticizer, solvent, and dispersant measured in terms of weight ratio was 100: 8:3:50:0.3. The ferrite powders and all organic additives were typically intermixed by ball milling for 2 to 4 hours and prepared a uniform dispersed slurry for the subsequent, doctor blade coating process. The loaded slurry was carried along the bottom of the doctor blade as the blade drags across a heated sample stage while leaving behind a film of desired thickness. The slurry was deposited on the PET plastic tape base. Final ferrite sheet is dried on the doctor blade coater and then, the PET tape is removed from the ferrite sheet before a sintering step. The organic remains were burnt out at 500°C. Using this method, a large quantity of uniform ferrite sheets can be produced with desired thickness as well as magnetic and mechanical properties. The process can operate in continuous mode.

2.3.2.2 *Compression Molding*

Ni-Co-Zn/ Epoxy based magnetic composites were prepared, first with mixing of two components of epoxy 302-3M-Med in the ratio of 100:45 between resin and curing agent using

planetary centrifugal mixer (ARE-310, THINKY, Japan) at 2000 rpm for 2 minutes, followed by degassing step in vacuum oven for 30 minutes. After that, Ni-Co-Zn ferrite powder was mixed in desired volume ratio with epoxy to form the composite. Small amount of solvent such as ethanol was added in the mixture to facilitate the uniform mixing of epoxy and ferrite powder. Mixing was again done in planetary centrifugal mixer at 2000 rpm for 5 minutes for homogeneous mixing and followed by degassing step in vacuum oven for 30 minutes. The final slurry mixture was poured in molds of specific thickness and cured at 80 °C for 2 hours using an Isotemp 281A vacuum oven. Figure 2-4 shows different steps in Ni-Co-Zn/Epoxy sheet formulation.

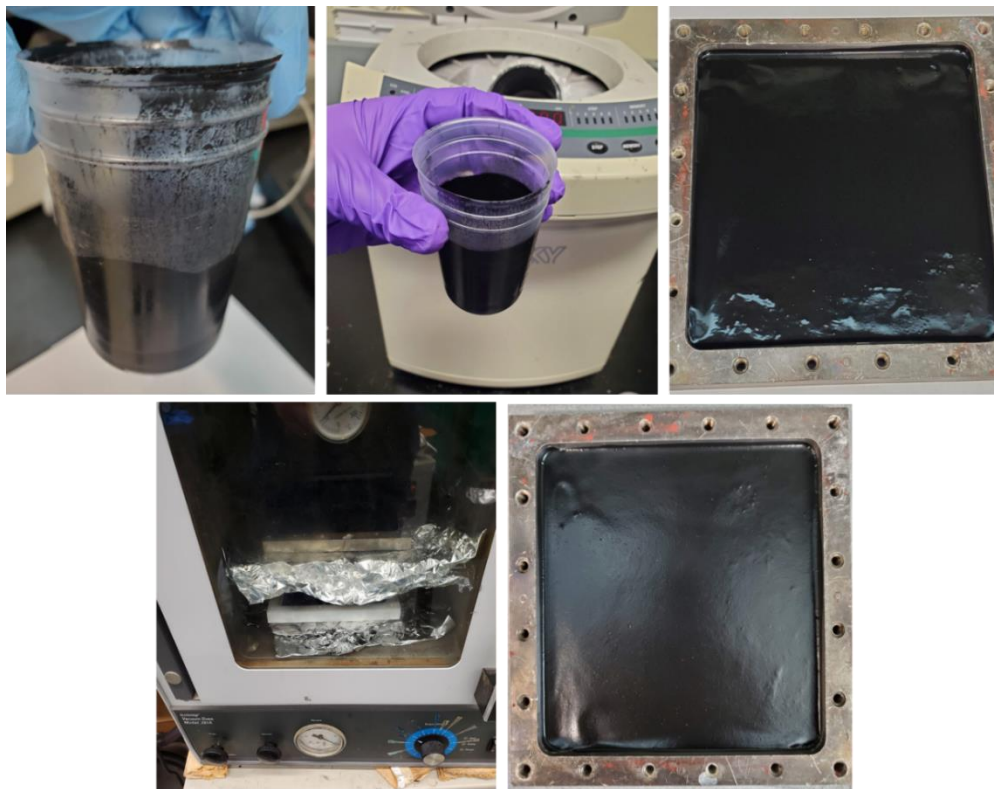


Figure 2-4 Ni-Co-Zn/Epoxy composite sheet preparation steps.

2.4 Characterization

2.4.1 X-ray Diffraction

X-ray diffraction was used to investigate the microstructure of Ni-Cu-Zn and Ni-Co-Zn ferrite powders. The phase composition of calcined and sintered ferrite powders was analyzed by X-ray θ - 2θ diffraction (XRD, X'Pert Pro diffractometer, Panalytical, Netherlands) at room temperature using Cu- $K\alpha$ radiation ($\lambda=0.1542$ nm). The XRD analysis was done to study the effect of different parameters such as additives, sintering conditions, and other synthesis/processing parameters on the crystal structure of the powders [60].

2.4.2 Scanning Electron Microscopy

The grain size and grain morphology of the sintered powders and toroidal samples were examined by scanning electron microscopy (Hitachi S800 SEM, Krefeld, Germany). SEM was used to study the morphology of the ferrite particles. Grain sizes distributions were analyzed using ImageJ software with a sample area consists of 50 grains. Average grain size was analyzed for all Ni-Cu-Zn and Ni-Co-Zn ferrite powders synthesized under different conditions. Bulk densities of the sintered specimens were determined by Archimedes principle.

2.4.3 RF/Impedance Analysis

The complex permeability and permittivity spectra of ferrite samples between 1 MHz and 1 GHz was measured by a RF impedance/material analyzer (E4991A, Keysight, CA, USA) using a magnetic material test fixture (Keysight 16454A, CA, USA) and dielectric test fixture (Keysight 16453A, CA, USA), respectively. To measure the complex permittivity disc and square shaped samples were formed according to the size requirement: disc ($d \geq 15$ mm, 0.3 mm $\leq t \leq 3$ mm) or Square ($d \geq 15$ mm, 0.3 mm $\leq t \leq 3$ mm). To measure the complex permeability toroidal shaped samples were formed according to the size requirement: Toroid ($b \geq \phi 3.1$ mm, $c \leq \phi 20$ mm and

$h \leq 8.5$ mm). Figure 2-5 and 2-6 shows the typical dimension requirements for the dielectric and magnetic samples for testing using impedance analyzer.

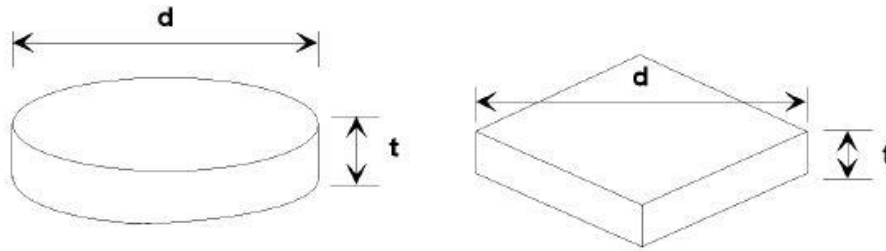


Figure 2-5 Disc and squared shaped samples for dielectric measurements.

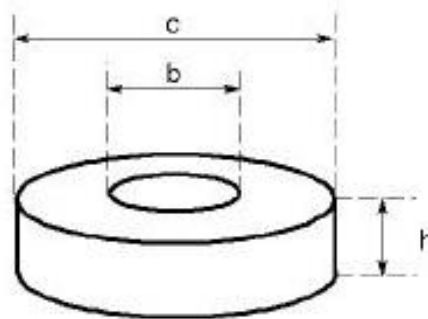


Figure 2-6 Toroidal shaped samples for magnetic measurements.

2.5 Summary

Synthesis method for Ni-Cu-Zn and Ni-Co-Zn ferrite powders are detailed in this chapter. Different synthesis conditions such as hydraulic pressure, press time, temperature and doping were utilized as key parameters in the synthesis method, which serve to optimize the magnetic and dielectric properties of the ferrite powders. Formulation of ferrite/polymer matrix: Ni-Co-Zn/302-3M and Ni-Co-Zn/PDMS is discussed while using two different techniques to make magnetic composite sheets, including compression molding and tape casting technique. Both techniques can be utilized in composite sheet preparation based on the requirements of the substrate. Finally, the different metrology and RF characterization techniques utilized in this work for the study of microstructure, morphology, magnetic and dielectric properties are also discussed.

Chapter 3: Microwave and Structural Properties of Ni-Cu-Zn Ferrite Powders

3.1 Note to Reader

Portions of this chapter, including figures have been previously published in *IEEE Magnetics Letters*, vol. 10, pp. 1-5, 2019 [28]; *IEEE Transactions on Magnetics*, vol. 55, 2, 2019 [60] and *Journal of Magnetism and Magnetic Materials* vol. 499, pp. 166273, 2020 [27]. Permissions are included in Appendix A.

3.2 Introduction

Ni-Cu-Zn ferrites hold desirable properties among all ferrites due to their high resistivity, high permeability and low losses at HF, VHF and UHF frequencies [61]. These properties of Ni-Cu-Zn ferrites depend on the chemical composition, microstructure, choice of additives and preparation method that can be modified easily through different synthesis parameters such as sintering temperature, reactant ratio and added dopants. Enhancement of the magnetic property and Q-factor with varied strategic choice of dopants in Ni-Cu-Zn ferrites has been reported. Addition of dopants such as Co_2O_3 , V_2O_5 , CaO and Bi_2O_3 as a sintering aid helps to lower the sintering temperature, thus resulting in low magnetic loss and better permeability [62-64]. Complex permeability and magnetic loss depend on domain wall motion and spin domain rotation [65]. Domain wall motion, in-turn is influenced by grain growth. High sintering temperature leads to abrupt grain growth, which induces higher magnetic loss in ferrites.

In this work, we demonstrated the effect of sintering temperature on the complex permeability of Ni-Cu-Zn ferrites at RF frequencies with and without addition of Bi_2O_3 as the

sintering aid [60]. The complex permeability and resonance frequency of Ni-Cu-Zn ferrites have followed the predictions of the Globus model given by equation 11 [66].

$$(\mu_i - 1)^2 f_r \approx \text{constant} \quad (11)$$

3.3 Effect of Sintering Temperature and Doping on Ni-Cu-Zn Ferrite Powder

$\text{Ni}_{0.33}\text{Cu}_{0.2}\text{Co}_{0.014}\text{Zn}_{0.456}\text{Fe}_{1.96}\text{O}_{3.94}$ ferrites were prepared via solid state reaction synthesis. The effect of bismuth oxide (Bi_2O_3) and sintering temperature on Ni-Cu-Zn ferrite powders has been investigated for the Near Field Communication (NFC) applications. The powders were prepared by conventional solid-state synthesis method. The microstructure and frequency dependent complex permeability were investigated [60]. Employment of Bi_2O_3 as a sintering aid promotes uniform grain growth and densification in sintered powders, which in turn has affected complex permeability spectra. It has been observed that the addition of Bi_2O_3 decreases permeability and magnetic loss from 147 to 110 and from 0.03 to 0.02, respectively, which were both sintered at 1100 °C and measured at 13.56 MHz frequency as compared to undoped sample (without Bi_2O_3). Also, permeability and magnetic loss increased with sintering temperature.

3.3.1 Microstructure Characterization

Microstructure and morphology of the sintered Ni-Cu-Zn powders were studied by X-ray diffraction and scanning electron microscopy.

3.3.1.1 X-Ray Diffraction (XRD) Analysis

Figure 3-1 presents the XRD patterns of both doped and undoped $\text{Ni}_{0.33}\text{Cu}_{0.2}\text{Co}_{0.014}\text{Zn}_{0.456}\text{Fe}_{1.96}\text{O}_{3.94}$ specimens sintered at 1100 °C. A single phase cubic spinel structure is observed in both the samples, with no secondary phase peak [60]. There is no bismuth peak observed in doped sample as percentage of Bi_2O_3 (0.2 wt%) is too small to be observed. Nevertheless, the intensity of doped sample is stronger as compared to undoped sample as seen in

Figure 3-1. The addition of Bi_2O_3 intensify the spinel phase formation in the reaction, hence the grains were arranged in more crystalline form [63].

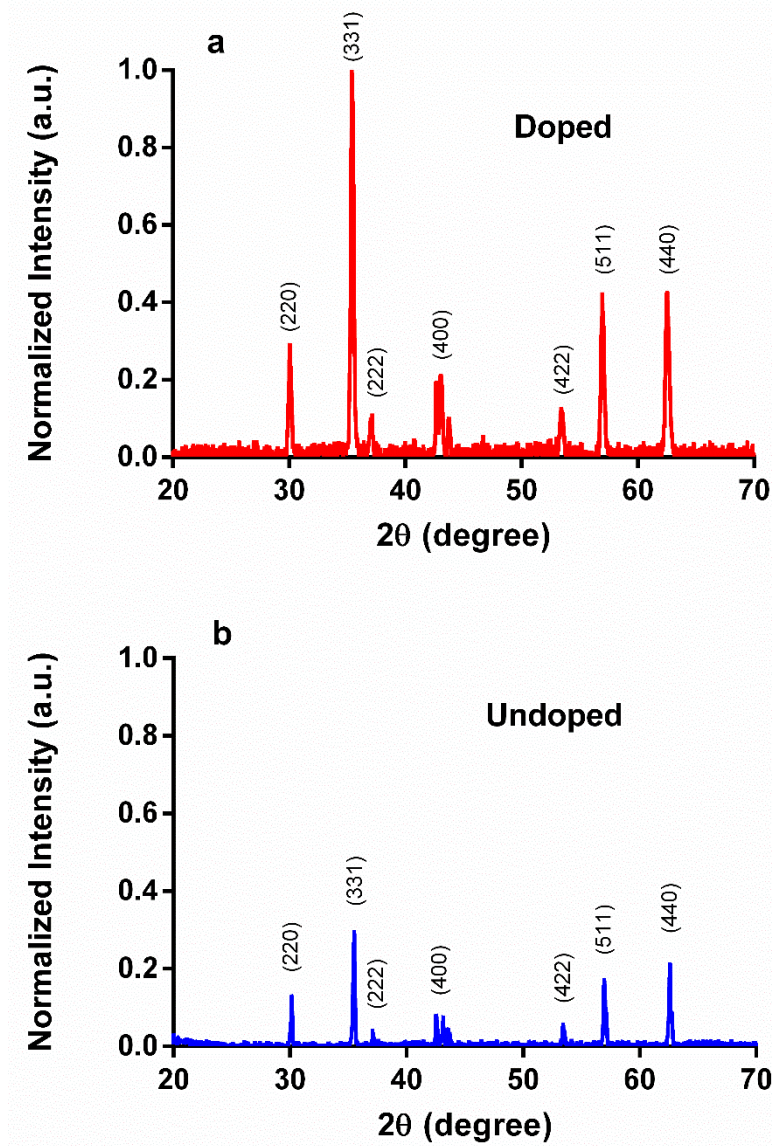


Figure 3-1 X-ray diffraction patterns of $\text{Ni}_{0.33}\text{Cu}_{0.2}\text{Co}_{0.014}\text{Zn}_{0.456}\text{Fe}_{1.96}\text{O}_{3.94}$ powders sintered at (a) 1100 °C for doped (0.2 wt% Bi_2O_3 , red curve) and (b) undoped (no Bi_2O_3 , blue curve) samples [60]. Permissions in Appendix A.

3.3.1.2 Scanning Electron Microscopy (SEM) Analysis

The surface morphology of $\text{Ni}_{0.33}\text{Cu}_{0.2}\text{Co}_{0.014}\text{Zn}_{0.456}\text{Fe}_{1.96}\text{O}_{3.94}$ ferrite samples were characterized using SEM. Figure 3-2. Shows the SEM images of ferrite samples with and without

bismuth dopants sintered at two different temperatures of 1100 °C and 1120 °C [60]. All SEM images were taken from the surface of the sintered toroid specimens. The grain growth and densification of sintered samples are highly dependent on the presence of Bi₂O₃ in the samples [63]. It can be seen from Figure 3-2 (a) and (b) that the addition of 0.2 wt% Bi₂O₃ promotes more uniform grain growth and facilitates densification. As compared to undoped samples (without Bi₂O₃), doped specimens (0.2 wt% Bi₂O₃) exhibited more uniform grain growth and reduction of pores. At 1100 °C, average grain size for doped (with bismuth oxide) samples lies between 15 to 20 μm, while for undoped sample, grain size lies between 15 to 25 micrometers. Bi₂O₃ is a low melting point (820 °C) additive, which forms liquid phase during sintering, as the chosen sintering temperatures of 1100 °C and 1120 °C are much higher than the melting point of Bi₂O₃. Hence, it enhances grain growth that leads to the densification as shown in Figure 3-2.

Additionally, higher densification and more abnormal grain growth were observed with an increase of the sintering temperature as shown in Figure 3-2 (c) and(d). At 1120 °C, average grain size lies between 25 to 30 μm for doped sample. Similar trend was observed for undoped sample at 1120 °C with average grain size lies between 20 to 30 μm. It can be confirmed that sintering at higher temperature induces a more abnormal grain growth and an increase of intragranular porosity. In undoped samples, dual microstructures were observed, consisting of both small grains and uncontrolled large grains. This can be ascribed to non-uniform grain growth and partial burnout of the binder.

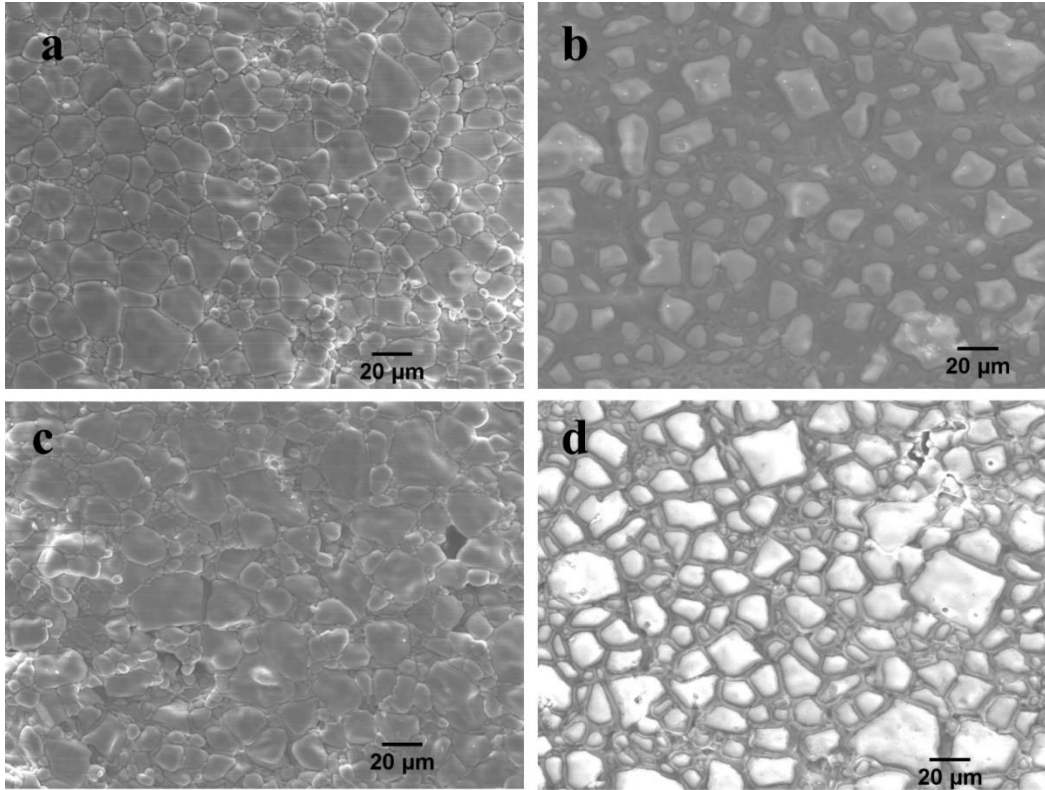


Figure 3-2 SEM images of NiCuCoZn ferrite sintered (a) doped, (b) undoped at 1100 °C and; (c) doped, (d) undoped at 1120 °C [60]. Permissions in Appendix A.

3.3.2 Dynamic Magnetic Properties

The measured frequency dependent complex permeability spectra and magnetic loss tangent of the doped and undoped $\text{Ni}_{0.33}\text{Cu}_{0.2}\text{Co}_{0.014}\text{Zn}_{0.456}\text{Fe}_{1.96}\text{O}_{3.94}$ samples, which are sintered at 1100 °C and 1120 °C, are depicted in Figure 4- [60] 3. It is noticed that addition of 0.2 wt% of Bi_2O_3 in the ferrite powders decreases real and imaginary part of permeability and the magnetic loss tangent as compared to undoped samples as shown in Figure 3-3 (a) and (b) for 1100 °C. The relative permeability decreases from 147 to 110, while the specimen is doped by 0.2 wt% of bismuth at 1100 °C measured at 13.56 MHz. Meanwhile, magnetic loss tangent is also lowered from 0.026 to 0.018 due to the addition of bismuth that promoted more uniform grain growth and pore size reduction as compared to undoped samples.

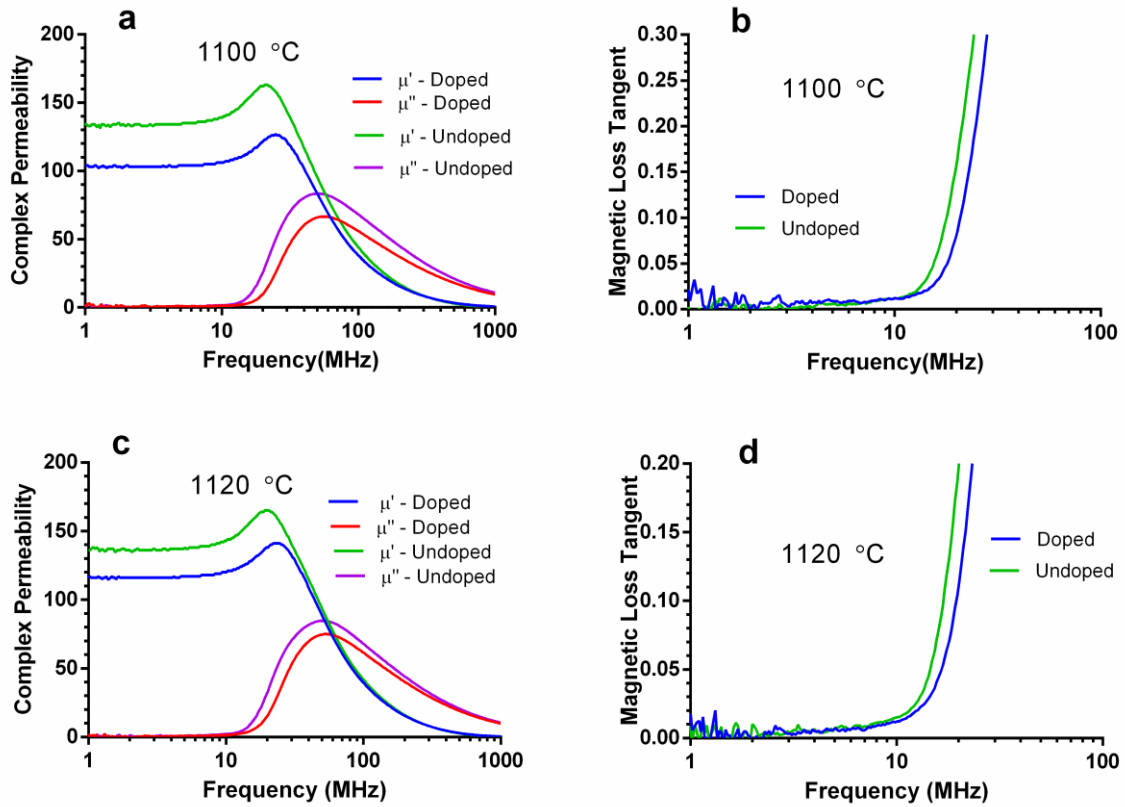


Figure 3-3 Complex permeability spectra of NiCuCoZn ferrite sintered at 1100 °C (a) complex permeability, (b) magnetic loss tangent for doped and undoped sample and 1120 °C (c) complex permeability, (d) magnetic loss tangent for doped and undoped sample [60]. Permissions in Appendix A.

Similarly, at 1120 °C as grain growth of particles are more an increase in real and imaginary part of permeability hence increase in magnetic loss were observed for both doped and undoped samples sintered at 1120 °C as observed in Figure 3-3 (c) and Figure 3-3 (d) due to abnormal grain growth. The comparison between the complex permeability spectra and magnetic loss at both temperatures for the doped and undoped samples are shown in Figure 3-4 (a) and (b).

According to Globus model, the product of resonance frequency and complex permeability of ferrites can be approximately estimated by the following equation 12 [66].

$$(\mu_i - 1)^2 f_r \approx \text{Constant} \quad (12)$$

where μ_i , and f_r are complex permeability and resonance frequency, respectively. The real and imaginary parts of the complex permeability, magnetic loss tangent, Q-factor and resonance frequency at 13.56 MHz for doped and undoped sample are listed in Table 3-1 [60].

Table 3-1 Real and imaginary parts of complex permeability, magnetic loss tangent, Q-factor and resonance frequency of ferrite samples at 13.56 MHz

Sample	Real Permeability	Imaginary permeability	Magnetic loss	Q-factor	Resonance frequency (MHz)
NiCuCoZn-0.2 wt% Bi ₂ O ₃ , 1100 °C	110	1.98	0.018	55.5	24.8
NiCuCoZn-0 wt% Bi ₂ O ₃ , 1100 °C	147	3.94	0.026	37.3	21.6
NiCuCoZn-0.2 wt% Bi ₂ O ₃ , 1120 °C	125	3.1	0.024	40.3	24.8
NiCuCoZn-0 wt% Bi ₂ O ₃ , 1120 °C	152	5.47	0.035	28	20.6

It can be concluded from the results shown in Table 1, the resonance frequency is higher for low permeability samples. It is anticipated that the low permeability specimens exhibit demagnetizing fields due to magnetic wall movements that raise the restoring force, thus resulting in an increased resonance frequency [66]. A similar trend is observed in all specimens.

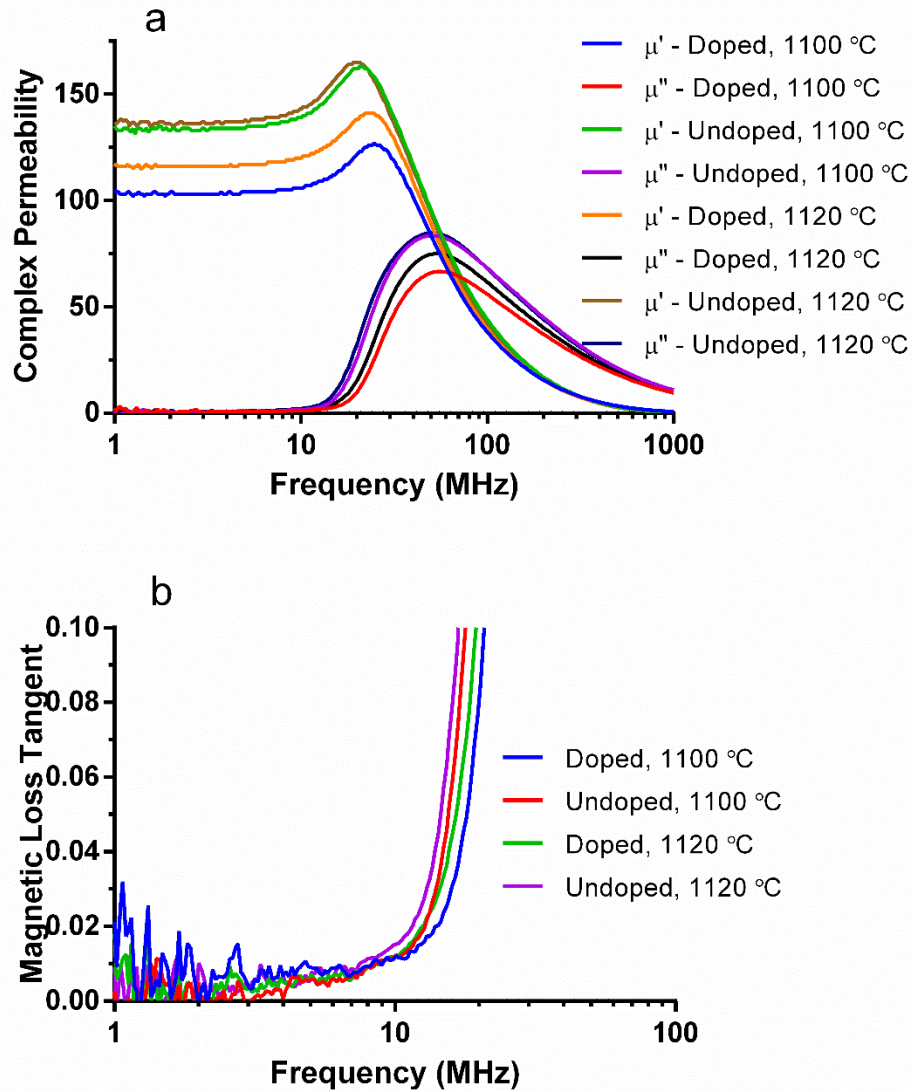


Figure 3-4 Comparison of (a) complex permeability spectra and (b) magnetic loss of NiCuZn ferrite sintered at 1100 °C and 1120 °C for doped and undoped samples [60]. Permissions in Appendix A.

3.3.3 Summary

The effects of the higher sintering temperature and addition of bismuth oxide on Ni-Cu-Zn ferrite powders were studied. Bismuth Oxide is used as a sintering aid in previous studies to lower the sintering temperature. The current study herein is focused on the effects of higher sintering temperature on the frequency dependent complex permeability and magnetic loss with and without

the usage of a sintering aid. At the elevated temperatures of 1100 °C and 1120 °C with the use of sintering aid, a high value of permeability (110 and 125) and low magnetic loss (0.018 and 0.024) were achieved, respectively. Meanwhile, undoped sample exhibited a permeability of 142 and 152 along with a magnetic loss tangent of 0.026 and 0.035, respectively. A 31% decrease in magnetic loss has been achieved with a 0.2 wt% Bi₂O₃ dopant in ferrite powders, while a 22.5% drop in real part of permeability (also known as relative permeability) has been obtained. High value of permeability and low magnetic loss is highly desired to realize high efficiency in NFC applications. Ni-Cu-Zn ferrites offer high permeability and low magnetic loss even after sintering at high temperatures. By controlling the grain growth while burning out the binder properly, high permeability and low magnetic loss can be more readily achieved [60].

3.4 Effect of Hydraulic Pressures at Different Sintering Temperature on Ni-Cu-Zn Ferrite Powders

In this section, we explored the effect of both sintering temperature and a relatively low-level of hydraulic force on the relative permeability and magnetic loss tangent of Ni-Cu-Zn ferrites [28]. It is expected that ferrite thin sheets produced under a similar range of pressure and sintering temperature will exhibit identical magnetic properties as those of toroidal test samples. This study presents our initial results for optimization of sintering temperature and amount of hydraulic force applied during the preparation of ferrite test specimens to achieve highly uniform grain growth, which in turn enhance the effective permeability while lowering magnetic losses. Ni-Cu-Zn ferrite toroidal test specimens were pressed under different levels of hydraulic force and sintered at varied sintering temperatures. The complex permeability spectra of these samples have been measured to study the effect of both hydraulic pressure and sintering temperature. An increase in real part of permeability from 110 to 125 due to an increase of sintering temperature from 1080 °C to 1120 °C

was observed for hand pressed toroidal samples [28]. Also, a significant increase in real part of the permeability from 125 to 152 was observed through the application of hydraulic pressure of 4 MPa with the same sintering temperature of 1100 °C. This study helps elucidate the roles of hydraulic pressure and sintering temperature for improving magnetic properties of Ni-Cu-Zn ferrites and our long-term goal is to develop ferrites for wireless power transfer at higher frequencies.

3.4.1 Microstructure Characterization

3.4.1.1 X-Ray Diffraction (XRD) Analysis

Figure 3-5 presents the X-ray diffraction patterns for the synthesized $\text{Ni}_{0.33}\text{Cu}_{0.2}\text{Co}_{0.014}\text{Zn}_{0.456}\text{Fe}_{1.96}\text{O}_{3.94}$ ferrite powders sintered at 1080 °C, 1100 °C and 1120 °C. All diffraction peaks match well with the standard pattern of Ni-Cu-Zn spinel cubic ferrite. The XRD patterns verify the formation of single-phase cubic structure without any impurity phase.

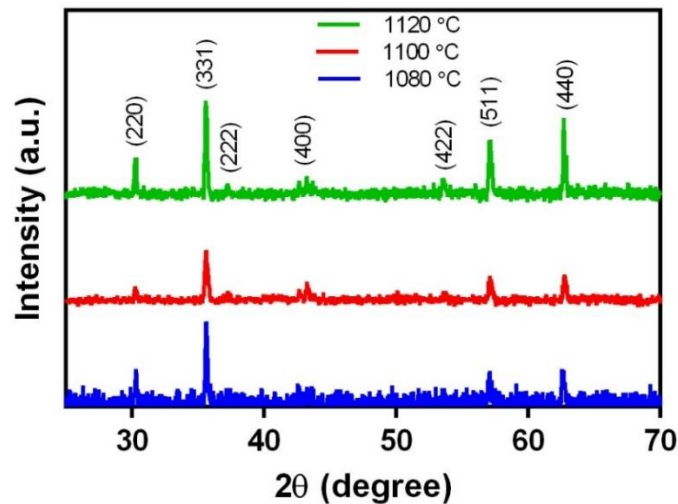


Figure 3-5 XRD patterns of samples sintered at 1080 °C, 1100 °C and 1120 °C [28]. Permissions in Appendix A.

3.4.1.2 Scanning Electron Microscopy (SEM) Analysis

Figure 3-6 shows the SEM micrographs of the surface of toroidal test samples sintered at different temperatures (1080 °C, 1100 °C, 1120 °C), which were pressed manually with no

additional hydraulic pressure applied. Fig. 3 shows SEM images of cracked samples at different hydraulic pressures (i.e., 4 MPa, 8 MPa, 12 MPa) that were all sintered at 1100 °C for 2 hours. The measured bulk sintered density and average grain size of Ni-Cu-Zn ferrite samples sintered at different temperatures are shown in Table 3-2 [28].

The density and grain size gradually increased along with an increment of the sintering temperature. The density of the sintered toroidal samples increased from 5.02 g/cm³ to 5.2 g/cm³ as a result of the increase of the sintering temperature from 1080 °C to 1120 °C. This can be attributed to temperature-driven densification. As shown in Figure 3-6 (a)-(c), a significant grain growth was also observed when the sintering temperature was increased [28]. The average grain sizes of 8-10 μm, 9-13 μm, and 20-30 μm were observed as a consequence of varied sintering temperature at 1080 °C, 1100 °C and 1120 °C, respectively. It was observed that as the sintering temperature rose above 1100 °C, an abnormal grain growth occurred, which can be ascribed to bimodal grain growth that took place at sintering temperatures above a critical temperature [61].

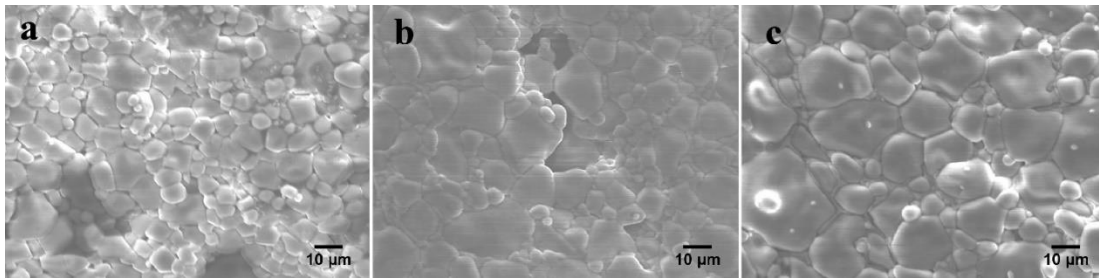


Figure 3-6 Top-view SEM images of the surface of toroidal samples sintered at (a) 1080 °C, (b) 1100 °C and (c) 1120 °C. All samples were pressed manually. Densification and grain size increases with the sintering temperature [28]. Permissions in Appendix A.

Figure 3-7 (a)-(c) shows SEM images of cracked toroidal samples pressed under a hydraulic pressure of 4 MPa, 8 MPa and 12 MPa, respectively. All the samples were sintered at 1100 °C for 2 hours. It can be observed from Figure 3-7 (a)-(c) that air voids or pores between grains decreases and samples become densified as the strength of hydraulic pressure increased

from 4 MPa to 12 MPa. And a similar effect can be seen when comparing them with the manually pressed samples as shown in Figure 3-6 (b). This increase in densification and reduction of air voids can be attributed to an increase in the effective contact area between the ferrite grains. It was observed that with an increase in hydraulic pressure, the average grain size increased from of 9-13 μm for a manually pressed sample to 14-18 μm for samples pressed under 4 MPa, 15-20 μm for samples pressed under 8 MPa, and 17-22 μm for samples pressed under 12 MPa, respectively. The externally applied force induced abnormal grain growth because of reduced grain boundary movement under the combined effect of high sintering temperature and hydraulic pressure [28].

It is evident from the results that the use of higher sintering temperature and application of hydraulic pressure/force on the samples contributed to an increased density and an enlarged average grain size of the Ni-Cu-Zn ferrite sample. In essence, the surface free energy is considered the main driving force for the sintering process while smaller and more uniform grain size facilitates the densification of the sample, which can be the possible underlying mechanisms. High sintering temperature decreases the surface activation energy, which leads to abnormal grain growth with poorer grain size uniformity [67, 68]. Meanwhile, an optimal level of hydraulic pressure can counter the abnormal grain growth by increasing the area of contact between the grains while also decreasing the effective area of the grain boundaries. Hence, simultaneous optimization of both hydraulic pressure and sintering temperature can result in properly densified samples with a desired uniform grain size [28].

Table 3-2 Bulk densities and grain size parameters of the toroidal NiCuCoZn ferrite samples that were pressed manually during the compression molding process but sintered at different temperatures

Temperature ($^{\circ}\text{C}$)	Density (g/cc) m^3	Average grain size (μm)
1080	5.02	8-10
1100	5.16	9-13
1120	5.2	20-30

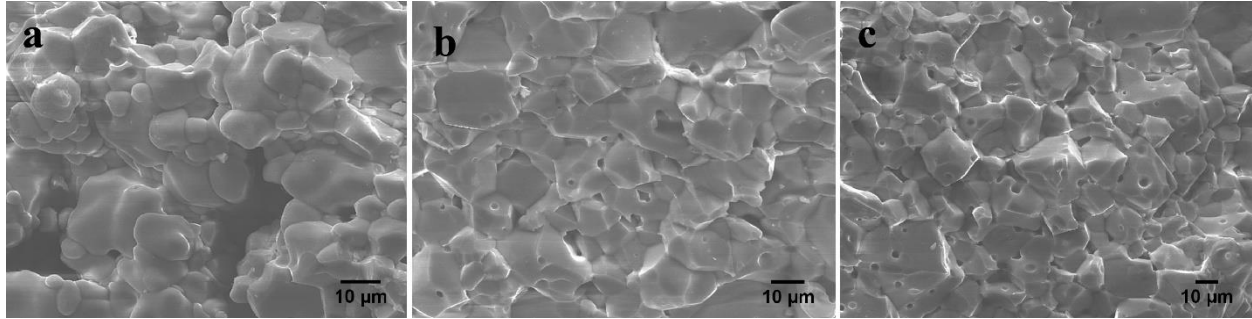


Figure 3-7 Cross sectional images of toroidal samples prepared under varied magnitude of hydraulic press and sintered at 1100 °C for 2 hours, including (a) sample prepared under a hydraulic pressure of 4 MPa; (b) sample prepared under a hydraulic pressure of 8 MPa; and (c) sample prepared under a hydraulic pressure of 12 MPa. Hydraulic pressure increases the densification and promotes more grain growth [28]. Permissions in Appendix A.

3.4.2 Dynamic Magnetic Properties

Figure 3-8 (a)-(e) shows the frequency spectra of the measured complex permeability of various Ni-Cu-Co-Zn ferrite toroidal samples at frequencies ranging from 1 MHz to 1 GHz. It was observed that the real and imaginary parts of permeability both increase with an increment of the hydraulic pressure. A comparison of the measured complex permeability can be made between manually pressed samples (103), the sample pressed under 12 MPa (126), which were both sintered at 1080 °C. The compression molded test samples pressed under 8 MPa and 12 MPa, have shown only small changes in the real part of permeability, whereas the imaginary part of permeability has increased more severely from 1.83 to 2.53, thus leading to an increase of magnetic loss tangent from 0.01 to 0.02 as shown in Figure 4-8 (a)-(b). Overall, the imaginary part of permeability has increased from 1.32 to 2.53 due to an increase in the loss tangent from 0.01 to 0.02. Similar trends of real and imaginary part of permeability were observed for samples sintered at 1100 °C and 1120 °C as can be seen in Figure 3-8 (c)-(e) [28].

The increase in the real part of permeability was much less for samples compression molded at a pressure higher than 8 MPa. This can be attributed to abnormal grain growth observed

for samples prepared under high hydraulic pressure during the compression molding process. Table 3-3. shows the real part of permeability, the imaginary part of permeability, magnetic loss tangent, Q-factor, and a commonly used figure of merit ($\tan\delta/\mu'$) for toroidal samples characterized at 13.56 MHz.

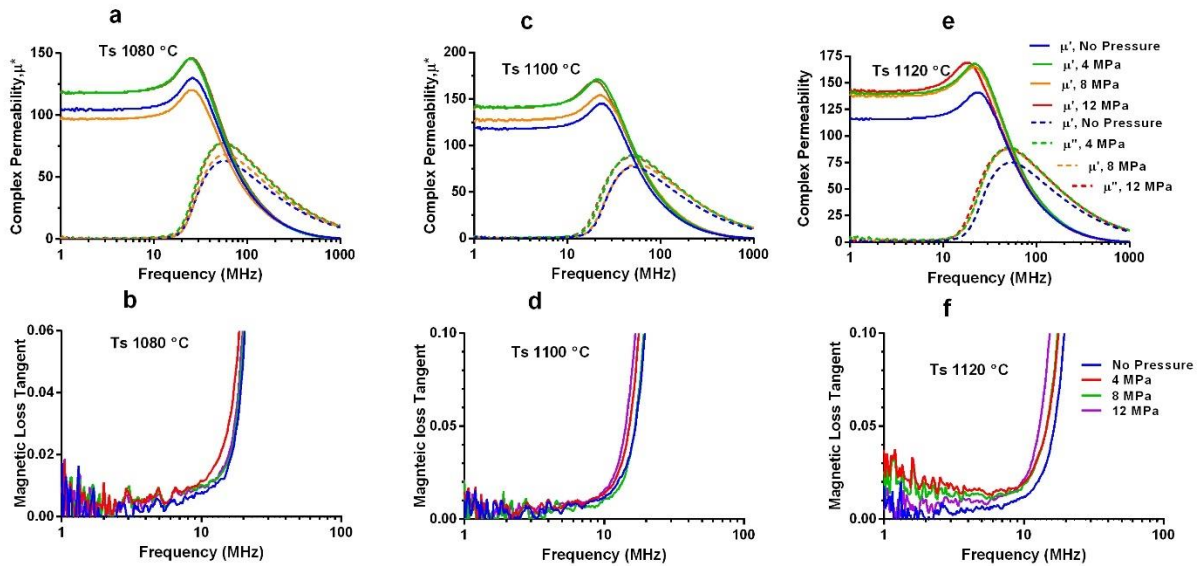


Figure 3-8 Measured complex permeability spectra of NiCuCoZn toroidal samples sintered at 1080°C, 1100°C and 1120°C under different hydraulic pressures: a) complex permeability for samples sintered at 1080°C; (b) magnetic loss tangent for samples sintered at 1080 °C; (c) complex permeability for samples sintered at 1100 °C; (d) magnetic loss tangent for samples sintered at 1100 °C; (e) complex permeability for samples sintered at 1120 °C; and (f) magnetic loss tangent at 1120 °C. All toroidal samples are prepared under the application of three different hydraulic pressures of 4 MPa, 8 MPa and 12 MPa, respectively. The manually pressed samples were labelled as “No Pressure” [28]. Permissions in Appendix A.

It has been reported that the complex permeability is strongly dependent on grain size and density of the NiCuZn ferrite powders [69, 70]. It is observed that only a slight increase in the real part of permeability was realized when the externally applied pressure is increased from 8 MPa to 12 MPa, which can be related to the average grain size as shown in Table 3-2 [28]. Figure 3-9 (a)-(b) presents the measured real and imaginary part of the permeability as well as the magnetic loss tangent for toroidal samples pressed under 4 MPa.

Table 3-3 The comparisons of the complex permeability, magnetic loss and Q-factor at 13.56 MHz for test specimens prepared by using varied sintering temperatures and hydraulic pressures

Sintering Temperature (°C)	Hydraulic Pressure (MPa)	Real Permeability (μ')	Imaginary Permeability (μ'')	Magnetic loss ($\tan\delta = \mu''/\mu'$)	Q-factor	FOM ($\tan\delta/\mu'$) 10^{-5}
1080	Manual Pressure	103	1.32	0.01	100	9.7
	4	110	1.38	0.012	84	10.9
	8	125	1.83	0.01	100	8
	12	126	2.53	0.02	50	15.8
1100	Manual Pressure	127	3.08	0.02	50	15.7
	4	138	2.84	0.03	34	21.7
	8	155	5.02	0.032	30.87	20.6
	12	157	6.43	0.04	25	25.4
1120	Manual Pressure	125	3.1	0.025	40	20
	4	151	6.13	0.04	25	26.5
	8	152	6.13	0.04	25	26.3
	12	161	6.43	0.06	17	37.2
[71]	-	150	5	0.033	30	22
[72]	-	100	3	0.033	30	33
[61]	-	132	3.96	0.03	33.3	22.7
[73]	-	144.5	3.6	0.025	40.14	17.2

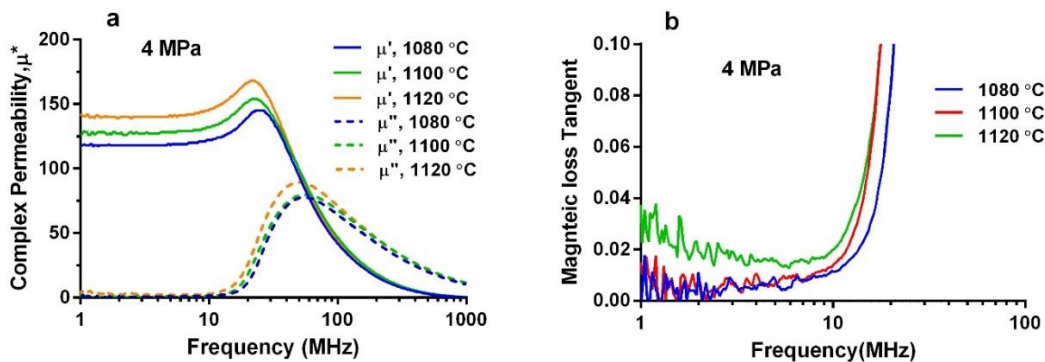


Figure 3-9 Dependence of complex permeability spectra on the varied sintering temperature at a fixed hydraulic pressure of 4 MPa: (a) real and imaginary parts of permeability; (b) magnetic loss tangent at different sintering temperatures including 1080 °C, 1100 °C and 1120 °C [28]. Permissions in Appendix A.

It can be clearly observed that with an increased sintering temperature, the real part of permeability increased from 103 to 125 for manually pressed samples. Similarly, an increase of the relative permeability from 110 to 151, from 125 to 152 and from 126 to 161 has been achieved for samples prepared under a pressure of 4 MPa, 8 MPa and 12 MPa, respectively. The imaginary part of permeability and magnetic loss tangent also followed a similar trend.

Figure 3-10 (a)-(b) shows the frequency-dependent Q-factor for samples prepared under different sintering temperatures and hydraulic pressures [28]. Q-factor is often used as a measure of performance, and it is the inverse of the magnetic loss tangent. It can be observed from the Figure 3-10 that the Q-factor decreases linearly with an increased sintering temperature for all samples prepared under varied hydraulic pressures. Q-factor that is defined as the ratio of the real and the imaginary part of permeability also changed under varied hydraulic pressures. As can be seen in Table 3-3, the measured Q-factor gradually decreased from 100 to 50, for all samples sintered at 1080 °C, as a result of the increasing hydraulic pressure up to 12 MPa. Moreover, the specimen prepared under 8 MPa of hydraulic pressure exhibited a high Q-factor of 100 while also holding a high permeability of 125, which indicate this as an optimal process condition.

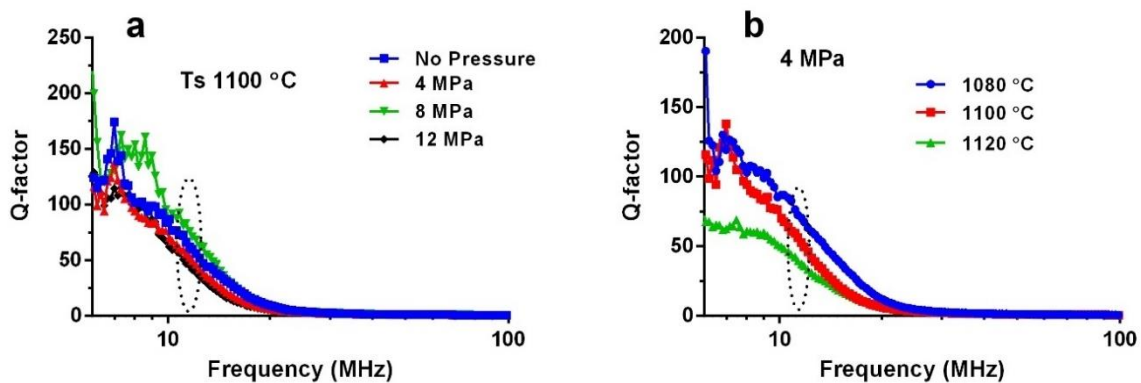


Figure 3-10 Dependence of extracted Q-factor on the frequency, showing (a) measured Q-factors for specimens sintered at 1100 °C under different hydraulic pressures; (b) measured Q-factors for samples prepared under a fixed hydraulic pressure of 4 MPa along with different sintering temperatures [28]. Permissions in Appendix A.

It is worth mentioning that the real and imaginary parts of permeability did not increase linearly with the applied sintering temperature and hydraulic pressure. Hence, our initial test results through comparisons among the samples prepared under these varied conditions implies that high permeability, low magnetic loss tangent, and high Q-factor can be jointly achieved when the grain sizes are limited in between 10 μm and 20 μm . Higher sintering temperatures give rise to high permeability and high density of the specimens because of the large grain size and reduced porosity. For samples with small grains, spin domain wall motion is less significant. However, when the grain that are greater than 3 μm typically have multiple domains and therefore the domain wall motion contributes to the permeability. The number of domain walls increases as the grain size increases due to the higher sintering temperature and hydraulic pressure [74]. Also, a very high sintering temperatures and high hydraulic pressure is anticipated lead to inhomogeneous grain growth and intragranular pores formation, thus resulting in more domain wall motions that lower the effective relative permeability and increase magnetic losses [75].

3.4.3 Summary

In this work, the effects of the sintering temperature and hydraulic pressure applied during compression molding of test specimens have been thoroughly studied, while the average grain sizes, bulk density, and complex permeability spectra are characterized and compared among the NiCuZn ferrite samples prepared under varied conditions [28]. It is observed that the optimization of the sintering temperature and hydraulic pressure can not only control the average grain size and density but also improve dynamic magnetic properties of the ferrite samples. The results indicate that a fairly high relative permeability of 125 and 155 along with a low magnetic loss tangent of 0.01 and 0.03 can be achieved through the employment of an optimal sintering temperature ranging from 1080 $^{\circ}\text{C}$ to 1100 $^{\circ}\text{C}$ and a hydraulic pressure of 8 MPa. In general, a relative permeability

greater than 120 and magnetic loss tangent lower than 0.05 are needed to achieve the desired power/signal transfer high efficiency in NFC devices.

3.5 Effect of Hydraulic Pressures and Durations on Ni-Cu-Zn Ferrite Powders

The present work focuses on varying the amount of applied low hydraulic pressure while making toroidal Ni-Cu-Zn ferrite test specimens for varied time durations to see its effect on the complex permeability spectra of Ni-Cu-Zn toroidal samples [27]. It is expected that similar effects can be observed for ferrite thin sheets prepared through processes such as cold or hot isostatic pressing. In this work, scanning electron microscopy (SEM) and complex permeability spectra have been explored to study the effects of hydraulic pressure and time duration. The ferrite fine powders were then granulated along with 5wt% PVA (Polyvinyl Alcohol) binder to prepare toroidal test samples under different levels of hydraulic pressure and time durations. The obtained ferrite powders were pressed under different hydraulic pressures (4 MPa, 8 MPa, 12 MPa) over different durations (30 sec, 2min, 3min and 5 min). Specific details of pressed toroidal samples are summarized in Table 3-4. Before complex permeability measurements, all the toroidal samples were sintered in the air at 1100 °C for 2 hours.

It was found that the complex permeability spectra change considerably with respect to the application of different hydraulic pressures and time duration. Porosity and grain size play an important role in affecting the permeability and magnetic loss of the ferrite samples. A significant increase of the real part of the complex permeability from 96 to 139 is observed due to the application of hydraulic pressure of 12 MPa for 3 min as compared to a manually pressed sample. The magnetic loss tangent also increases from 0.01 to 0.02 as the imaginary part of the complex permeability increases, which is still acceptable for most of the wireless power transfer (WPT) applications. It is postulated that the effect of hydraulic pressure on ferrite powder-based

composites increases the real part of permeability while influencing magnetic loss less severely [27].

Table 3-4 Different toroidal samples pressed under different hydraulic force levels and different durations. X is the sample, which was prepared by a manual pellet press

Hydraulic Pressure (MPa)	Reference (No applied pressure)	30sec	2min	3min	5min
4	X	A1	A2	A3	A4
8	X	B1	B2	B3	B4
12	X	C1	C2	C3	C4

3.5.1 Microstructure Characterization

3.5.1.1 X-Ray Diffraction (XRD) Analysis

Figure 3-11 shows the XRD pattern of $\text{Ni}_{0.35}\text{Cu}_{0.19}\text{Zn}_{0.46}\text{Fe}_2\text{O}_4$ powders sintered at 1100 °C for 2 hours. A single-phase spinel structure was observed, while no extra unaccounted peak was observed in the X-ray pattern, thus confirming the absence of secondary phase in the structure. The strongest peak observed correlates to (311) crystal orientation [27].

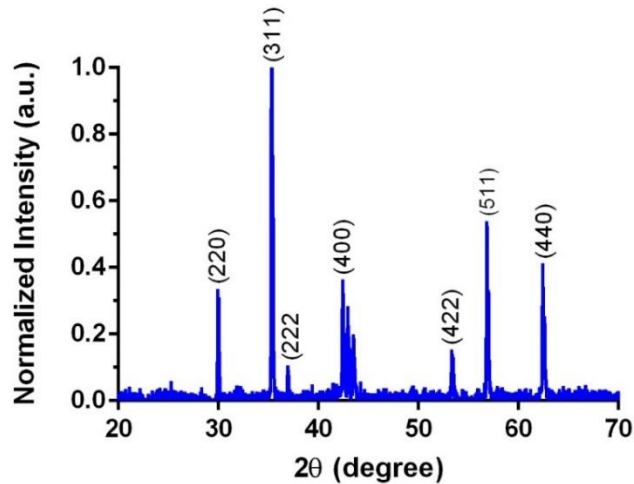


Figure 3-11 X-ray diffraction pattern of $\text{Ni}_{0.35}\text{Cu}_{0.19}\text{Zn}_{0.46}\text{Fe}_2\text{O}_4$ powder [27]. Permissions in Appendix A.

3.5.1.2 Scanning Electron Microscopy (SEM) Analysis

To observe the effect of low hydraulic pressure on the porosity and grain growth of the toroidal samples, SEM images were taken. Figure 3-12 (a)-(d) present the SEM images of $\text{Ni}_{0.35}\text{Cu}_{0.19}\text{Zn}_{0.46}\text{Fe}_2\text{O}_4$ toroidal specimens formed while applying a 12 MPa pressure for varied durations. All the specimens were sintered at 1100 °C for 2 hours. It can be observed from Figure 3-12 (a)-(d) that porosity decreases as the duration of applied hydraulic pressure is increased as compared to the reference sample pressed and formed manually. Figure 3-13 (a)-(c) shows the comparison of SEM images of toroidal samples pressed manually and under two different hydraulic pressures (4 MPa and 12 MPa) for same time duration. The densification and grain growth of particles can be clearly observed due to increasing hydraulic pressure [27].

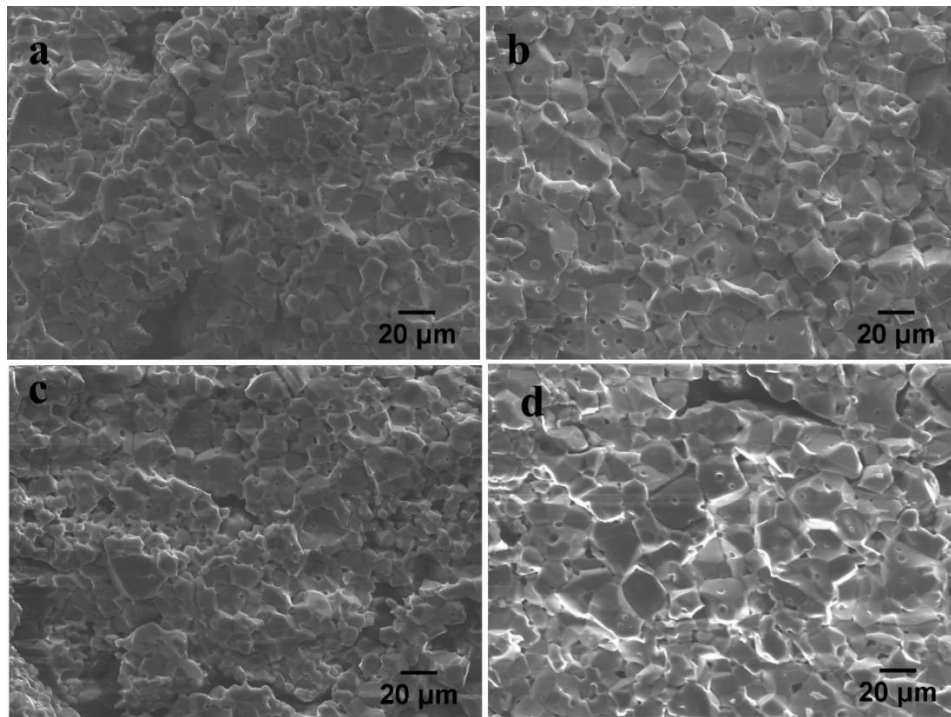


Figure 3-12 Cross-sectional SEM images of toroidal samples prepared under varied amplitude and duration of hydraulic press (a) sample prepared by manual press without hydraulic force applied; and three other samples pressed under 12 MPa hydraulic pressure for different durations: (b) pressed for 30 sec; (c) pressure applied for 2 min; (d) pressed for 5 min. With increased time duration up to 5 min, particles become more densely packed, thus reducing porosity in the sample. All samples were sintered at 1100 °C for 2 hours [27]. Permissions in Appendix A.

Toroidal samples prepared without hydraulic pressure has more porosity as compared to samples prepared with the hydraulic press. The decrease in porosity and increase in density for hydraulically pressed sample A1 can be associated with the increase in contact area between the particles. Consequently, density of the different samples sintered at the same temperature of 1100 °C varies with the change in duration of the hydraulic press as shown in Figure 3-14 (a)-(b). Specifically, the dependence of the density for samples X to A4 on the duration of the applied hydraulic pressure of 12 MPa is shown in Figure 3-14 (a)-(b). The density of sintered toroidal specimens increases upon the application of hydraulic force as compared to the manually pressed sample (A1-5.357 g/cm³ vs. X- 5.217 g/cm³) [27]. However, when the duration of applied pressure increases beyond the initial 1-minute period, a decrease in density is observed (from A2- 5.357 g/cm³ to A4- 5.17 g/cm³). The decrease can be attributed to the sudden and abnormal grain growth observed at longer durations which leads to bimodal grain size distributions. The force/pressure level to induce such type of grain growth highly depends on the grain size distribution. Because of

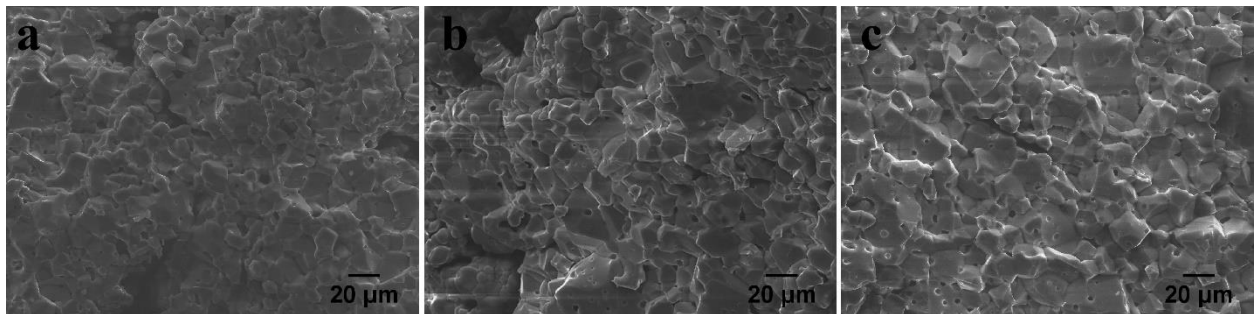


Figure 3-13 Cross-sectional SEM images of toroidal samples prepared under varied amplitude and 30 seconds of applied hydraulic press (a) sample prepared by manual press without hydraulic force applied; (b) sample pressed under 8 MPa hydraulic pressure; (c) sample pressed under 12 MPa. With increased pressure from manual to 12 MPa, particles become more densely packed, thus increasing the real part of the complex permeability [27], permissions in Appendix A.

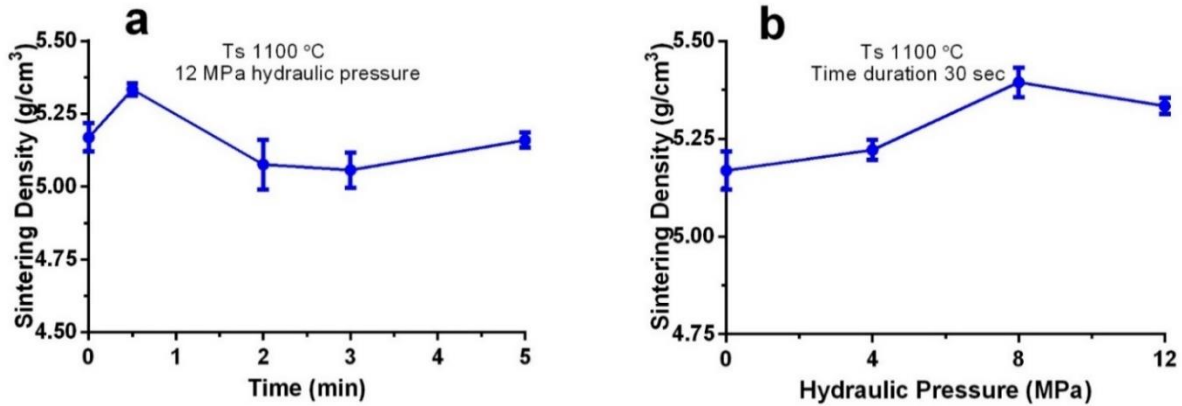


Figure 3-14 The density data of different toroidal samples: (a) pressed under 12 MPa hydraulic pressure for different time durations; (b) pressed for 30 secs at different hydraulic pressures [27]. Permissions in Appendix A.

non-uniform grain size distribution observed at higher sintering temperature, there is abnormal grain growth observed at higher pressures and longer durations which results in decrease of pore mobility. Pore separation from boundaries occurs due to non-uniform grain size distribution, which leads to intra-granular pore entrapment thus lowering the density [69, 76].

It was observed that average particle size increases with raised pressure levels and longer durations. For instance, average particle size for manually pressed sample lies between 8-15 μm , whereas average particle sizes for specimens hydraulically pressed for 30 sec, 2min and 5 min span between 11-30 μm , 11-18 μm and 18-25 μm , respectively. This can be attributed to variation in density due to the amplitude and duration of the hydraulic press process, which results in different grain growth of the particles. From the density and grain size measurements, it can be concluded that the further increase in duration of hydraulic press beyond 2 minutes is anticipated to have negligible impact [27].

3.5.2 Dynamic Magnetic Properties

Figure 3-15 (a) - (f) show RF complex permeability spectra of NiCuZn ferrite specimens sintered at 1100 °C under different amplitudes and durations of applied hydraulic pressures [27].

The complex permeability spectra of toroidal samples pressed under three different hydraulic pressures (i.e., 4 MPa, 8 MPa and 12 MPa) for different durations have been measured over a wide frequency range between 1 MHz to 1 GHz. It was observed that toroidal samples exhibit a noticeable difference in both real and imaginary parts of complex permeability spectra under different amplitudes and durations of the hydraulic press. In Figures 3-15 to 3-17, zero duration response corresponds to the manually pressed samples. It can be seen from Figure 3-15 (a), there was a significant increase in the relative permeability (real part of permeability) for sample prepared under a hydraulic pressure of 4 MPa as compared to the manually pressed specimen.

Specifically, for a short duration of 30 seconds, hydraulically pressed specimen A1 has exhibited a relative permeability of 135, which is significantly higher than that of the manually pressed sample A1 ($\mu_r = 96$). On the contrary, no significant increase was observed after longer durations of applied hydraulic press [27]. In fact, there was a decrease in relative permeability observed from 135 to 117 from sample A2 to sample A4, due to further increased hydraulic press duration. Likewise, imaginary part of permeability first increases from 1.17 to 2.66 as a result of short duration of hydraulic press as seen in sample X and A1. Similarly, the imaginary part of the permeability gradually decreases from 2.66 to 1.18 as longer duration of hydraulic press has been applied as shown in samples A2 to A4.

Figure 3-15 (b) presents the magnetic loss tangent versus frequency. It was reported previously that an increase in density increases the volume fraction of magnetic particles, which in turn led to low magnetic loss and high permeability [77]. Our study shows the similar trends. So, it can be deduced from density measurements in Figure 4 that higher density and lower porosity due to applied hydraulic pressure is expected to contribute to lower magnetic loss and higher permeability. Similar trends were observed for samples prepared by hydraulic press under 8 MPa

and 12 MPa pressure. There is a maximum value of the relative permeability for a certain duration (up to 30 seconds-2 minutes), and subsequently the real part of the complex permeability decreases as seen in Figure 3-15 (c)-(f). Variations of both real and imaginary parts of permeability and magnetic loss with different pressures at constant time duration 30 seconds can be seen in Figure 3-16 (a)-(b).

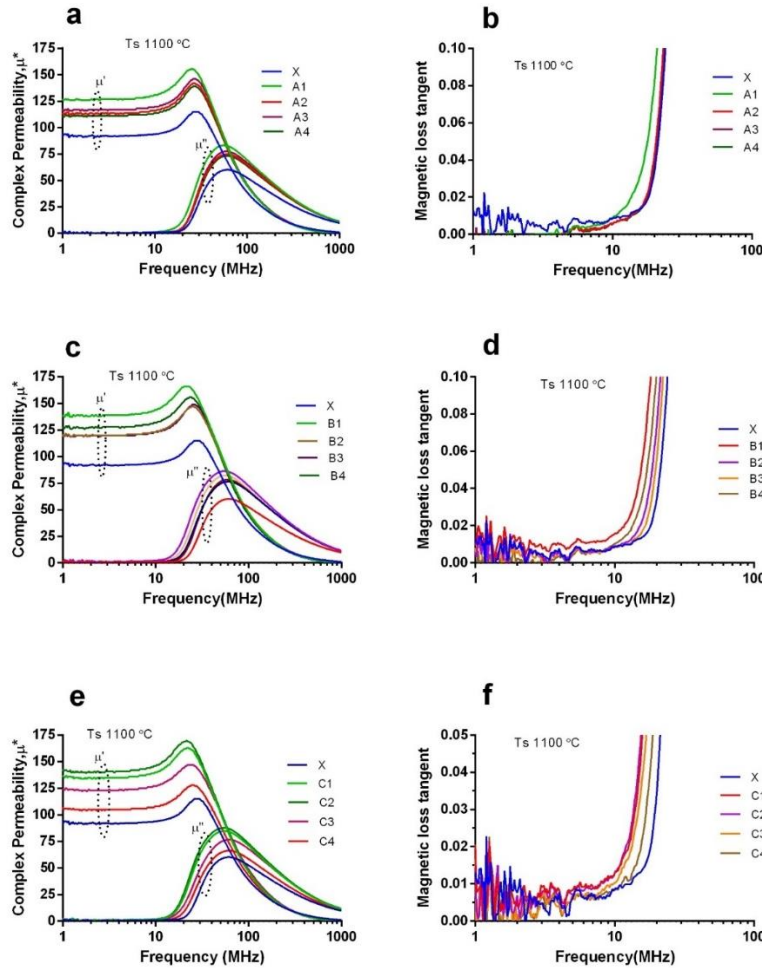


Figure 3-15 Measured RF complex permeability spectra of NiCuZn ferrite toroidal samples: (a) complex permeability of samples pressed under applied hydraulic pressure of 4 MPa for different time durations (b) magnetic loss tangent for the 4 MPa pressed samples (c) complex permeability of samples pressed under applied hydraulic pressure of 8 MPa for different time durations; (d) magnetic loss tangent for 8 MPa pressed samples; (e) complex permeability of samples pressed under applied hydraulic pressure of 12 MPa for different time durations; (f) magnetic loss tangent for under 12 MPa pressed samples. X refers to the manually pressed reference sample formed without no applied hydraulic pressure[27]. Permissions in Appendix A.

It can be concluded from Figure 3-16 that with an increase in hydraulic pressure permeability increases to a certain point then decreases because of abnormal grain size distribution observed at high pressure. Figure 3-17 (a)-(b) show real and imaginary parts of measured permeability at 13.56 MHz for samples prepared under different durations and amplitudes of hydraulic forces. At low hydraulic pressure of 4 MPa, the relative permeability μ' (real value of complex permeability) at 13.56 MHz increases as the duration of hydraulic press increases, which can be partially attributed to reduced porosity [27].

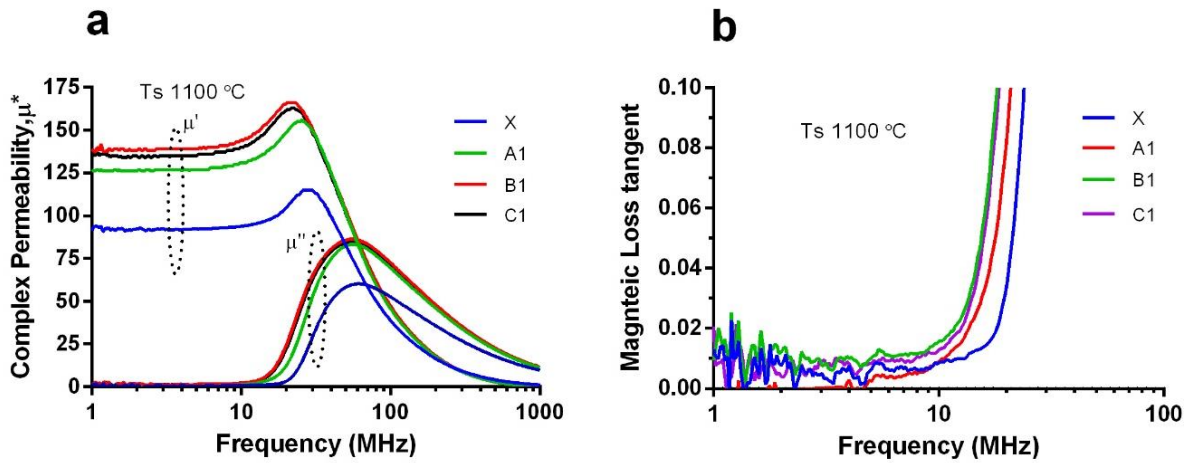


Figure 3-16 Measured RF complex permeability spectra of NiCuZn ferrite toroidal samples: (a) complex permeability of samples pressed for 30 seconds under different applied hydraulic pressures (b) magnetic loss tangent for the 30 second pressed samples. The real part of permeability first increased from manual to 8 MPa pressed sample then decreases slightly due to abnormal grain growth and large grain size observed for sample pressed under 12 MPa [27]. Permissions in Appendix A.

For higher hydraulic press duration, μ' and μ'' start to decrease. It is noteworthy that the relative permeability (μ') increases from 135(A1) to 151 (B1) and 147 (C1) due to the hydraulic press at relative high-pressure of 8 MPa and 12 MPa, respectively, for the same duration of 30 seconds. This can be explained by the fact that ferrite samples prepared by hydraulic press at these higher pressures have less porosity as compared to the counterparts prepared under 4 MPa, resulting in high value of relative permeability [27]. Variations of magnetic loss tangent and Q-

factor at 13.56 MHz for samples prepared under different hydraulic pressures and durations are presented in Figure 3-17 (c)-(d). It is observed that the higher Q-factors and low magnetic losses have been demonstrated by toroidal samples hydraulically pressed under 4 MPa. It is entailed that samples prepared under an optimal condition of hydraulic press in terms of amplitude and duration gives high Q-factor and low magnetic loss along with high permeability.

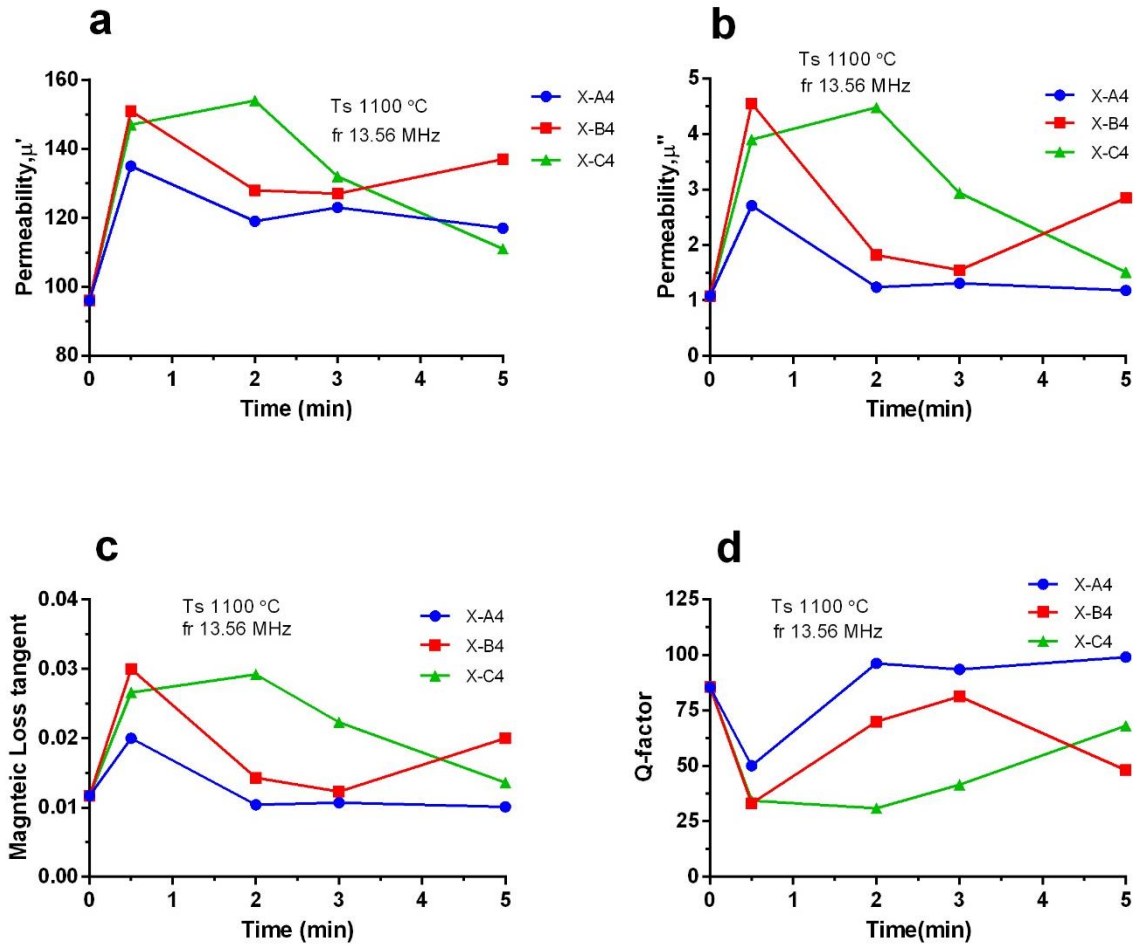


Figure 3-17 (a) Real part of complex permeability versus varied hydraulic press duration under different hydraulic pressures applied; (b) imaginary part of complex permeability versus varied hydraulic press duration under different hydraulic pressures applied; (c) magnetic loss tangent versus hydraulic press duration under different hydraulic pressures applied; (d) Q-factor versus hydraulic press duration under different hydraulic pressures. All results were taken at 13.56 MHz based on measured complex permeability spectra [27]. Permissions in Appendix A.

However, all toroidal samples have shown increased magnetic loss and decreased Q -factor after application of higher hydraulic pressures. This could be associated with higher rate of grain growth observed in samples pressed under higher hydraulic pressure, consequently giving rise to high magnetic loss and low Q -factor. It is evident that grain size and density have a strong effect on permeability, magnetic loss and Q -factor of ferrites [78]. Magnetic loss tangent can be extracted from measured complex permeability spectra in Figure 3-17 (a)-(c), and samples that offer high permeability often exhibit high magnetic loss tangent as well.

It has been reported in earlier works that the magnetic properties of polycrystalline ferrite materials strongly correlates to spin domain rotation and domain wall motion [66, 78]. Meanwhile, the domain wall motion depends on grain size and density of the polycrystalline ferrites. For instance, Sun *et al.* in 2008 reported larger grain size and higher sintering density could lead to an increase in relative permeability. These reported observations are consistent with the key findings of this work [63].

3.5.3 Summary

The effect of varied amplitudes and durations of hydraulic press on the resultant complex permeability spectra of $\text{Ni}_{0.35}\text{Cu}_{0.19}\text{Zn}_{0.46}\text{Fe}_2\text{O}_4$ ferrite toroidal samples have been studied. The solid-state synthesis technique was used to synthesize $\text{Ni}_{0.35}\text{Cu}_{0.19}\text{Zn}_{0.46}\text{Fe}_2\text{O}_4$ ferrite powders. The real part of the complex permeability (μ') is increased by decreasing porosity and increasing rate of grain growth, which in turn depend on hydraulic pressure parameters (time and magnitude of the hydraulic force) as evidenced by our experiments [27]. The magnetic loss tangent and Q -factor also depend on amount of hydraulic pressure applied. The results indicate that an optimal amount of applied hydraulic pressure and duration can be adopted to prepare toroidal samples with controlled porosity and density, which further improves relative permeability and Q -factor.

Samples pressed under different hydraulic pressures (e.g., A1(135), B1(151) and C1(147)) universally show increments in real part of permeability as compared to manually pressed reference sample (X), which has a relative permeability of 96. The percentage increases of relative permeability are 40.6%, 57% and 53% for ferrite sample A1, B1 and C1, respectively. However, magnetic loss also increases together with the permeability increment, which results in Q-factor reduction from 85.5 to 51, 33 and 34 for samples A1, B1 and C1, respectively. Variations of complex permeability for samples prepared under varied hydraulic pressure clearly indicate the change in porosity, grain size and density with applied hydraulic pressure during sample preparation. Dense and less porous Ni-Cu-Zn ferrites with uniform grain size are anticipated to exhibit high permeability and low loss. It will be worthwhile to explore effect of hydraulic pressure on other static and dynamic magnetic properties of Ni-Cu-Zn ferrites to explore the underlying mechanism. These experiments can be instrumental to further optimization of the manufacturing of the thin ferrite sheets under cold or hot isostatic pressures for wireless power transfer applications. This work provides new evidence and a new route for achieving better dynamic magnetic properties of NFC materials. Our future studies will focus on developing more robust soft magnetic ferrite materials for WPT and other high frequency applications through better understanding the mechanisms involved and hence optimizing the synthesis process.

Chapter 4: Microwave and Structural Properties of Ni-Co-Zn Ferrite Powders

4.1 Note to Reader

Portions of this chapter and figures have been previously published in *J. Am Ceram Soc.* vol. 105, pp. 2678–2689, 2022 [31]. Permissions are included in Appendix A.

4.2 Introduction

This chapter presents, effect of different dopants such as CuO and Co₂O₃ on microwave and structural properties of Ni-Co-Zn ferrites to achieve high permeability and low magnetic losses for RF and microwave device applications [31]. Composition and microstructure control is crucial to obtain the desired magnetic and loss properties. CuO dopant (x = 0 wt% to 20 wt%) and Co₂O₃ (x=0.10 to x=0.25) were employed during the synthesis of Ni-Co-Zn ferrite powders to modify the microstructures, thus improving the magnetic properties of the ferrites. High values of measured relative permeability (μ' of 4 -10) and relatively low magnetic loss tangent ($\tan\delta_m$ of 0.01- 0.1) has been achieved at frequency range between 100 MHz and 1 GHz for different doping. Solid state synthesis method was used for synthesis of all powders. Various researches have been conducted for improving magnetic properties and raising of resonance frequency on spinel ferrites and hexaferrites using different dopants such as Cu substituted Ni-Zn ferrite [29, 41, 42], Ca and Cao-SiO₂ doped Ni-Co-Zn [43], Y and La doped Ni-Co-Zn ferrite [44], Co-Ti substituted M-type barium hexaferrite [45], Ir, ZA, Ca and glass doped Co₂Z hexaferrite [46, 47] [48], and so on at radio frequency region. Ni-Co-Zn composition was chosen as cobalt oxide in spinel lattice of Ni-Zn helps in reducing core loss and contributes to the enhancement of the magneto crystalline anisotropy, thereby achieving better dynamic magnetic properties [49]. It is hypothesized that

migration of cobalt ions in spinel lattice stabilizes the magnetic domain walls because of induced anisotropy. Copper oxide acts as sintering aid to lower the sintering temperature, thus promoting the grain growth and densify the microstructure.

4.3 Effect of CuO on Ni-Co-Zn Ferrite Powders

In this paper, we introduced CuO as dopant into Ni-Co-Zn polycrystalline ferrites by adding CuO after the crystalline structure was formed by solid-state ceramic synthesis process. Subsequently, the effect of CuO concentration upon complex permeability and permittivity spectra as well as losses over 1 MHz to 1 GHz frequency range has been carefully studied. There is no prior report on copper oxide (CuO) doped Ni-Co-Zn ferrite. Previous studies showed that the addition of copper oxide in Ni-Zn ferrites could tune the magnetic properties, hence permeability and magnetic losses can be tailored [49]. The effect of CuO concentration on phase composition and microstructure have also been systematically studied and correlated with dynamic magnetic and dielectric properties [31].

4.3.1 Microstructure Characterization

4.3.1.1 X-Ray Diffraction (XRD) Analysis

The XRD patterns of the CuO (x=0 wt% to 20 wt%) doped $\text{Ni}_{0.4}\text{Co}_{0.25}\text{Zn}_{0.35}\text{Fe}_2\text{O}_4$ ferrite powders are shown in Figure 4-1. The sharp and high-intensity peaks in the XRD indicates the formation of single-phase spinel structure and all the peaks are indexed with the (JCPDS Card 00-08-0234). Extra peaks of CuO appeared in the XRD patterns of Ni-Co-Zn ferrite for x >3% of relatively small intensities. All compositions exhibited maximum intensity at (311) and other strong diffraction peaks corresponds to (111), (220), (311), (222), (422), (511) and (440) *hkl* planes. Lattice parameters are shown in Table 5-1 for all the compositions of varied CuO dopants. The lattice constant (*a*) in cubic crystal lattice was calculated using the following equation 13

$$a = d\sqrt{h^2 + k^2 + l^2} \quad (13)$$

where d is the interplanar spacing and hkl are the Miller indices. The value of lattice constant matches with as reported values in the literature for Ni-Co-Zn ferrites, which varies with the level of added CuO dopants [31]. The lattice constant first increases with CuO doping and then slightly decreases at higher doping percentage $x > 3$ wt% as shown in Figure 4-2 (A). This can be attributed to difference in ionic radii of copper (0.73 Å), nickel (0.69 Å) and cobalt (0.745 Å) ions. The initial increase (8.315 Å to 8.440 Å) in lattice constant is expected because ionic radii of copper is larger than that of nickel. As the amount of copper ions increases in the composition, there was a slight decrease in lattice constant after $x > 3$ wt%, which may be attributed to segregation of excess copper ions at the grain boundaries. Also, there is a possibility of migration of copper ions to A site rather than B site due to excess amount of copper ions. The average crystallize size was calculated using Scherrer formula given by equation 14.

$$D = \frac{k\lambda}{\beta \cos\theta} \quad (14)$$

where k is a constant, λ is X-ray wavelength, β is full width half maximum and θ is diffraction angle. As shown in Figure 5-2 (A), the calculated crystal size decreases with amount of CuO dopants from 69.76 nm ($x=0$ wt%) to 30.06 nm ($x=20$ wt%). Furthermore, the diffraction angle of peaks of CuO doped Ni-Co-Zn ferrite shifted with the CuO doping as compared to undoped samples as shown in Figure 4-1. This is related to the substitution of copper ions in the cubic lattice as diameter of Cu, Ni and Co ions are different, the peaks shift according to the ionic radii of each element [79]. The theoretical X-ray density was calculated using the following equation 15.

$$d_{X-ray} = \frac{nM_V}{N_A V} \quad (15)$$

where, n is number of moles per unit volume, M_V is molecular weight of sample, N_A is Avagadro

number and V is volume of sample. The porosity percentage was calculated for all $\text{Ni}_{0.4}\text{Co}_{0.25}\text{Zn}_{0.35}\text{Fe}_2\text{O}_4$ samples sintered at 1100 °C for 2 hours according to the equation 16 [31].

$$P\% = 100\left(1 - \frac{d_{X\text{-ray}}}{d_{\text{Bulk}}}\right)\% \quad (16)$$

where, $d_{X\text{-ray}}$ is the theoretical X-ray density and d_{Bulk} is bulk density.

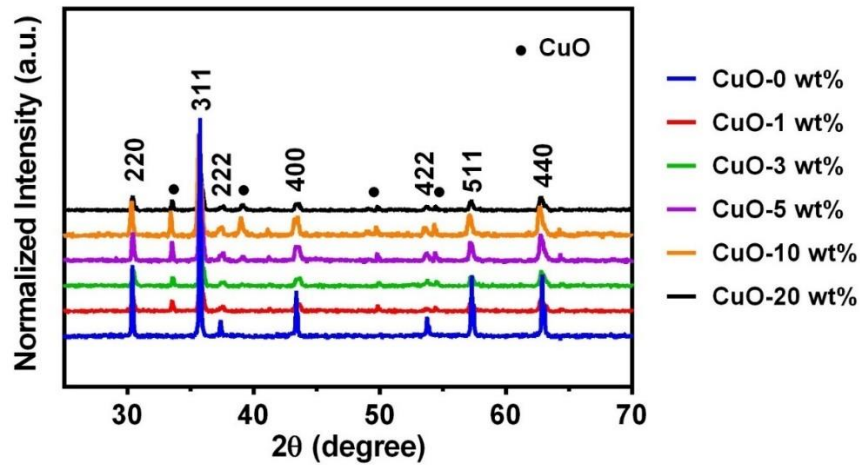


Figure 4-1 XRD patterns of CuO ($x=0, 1, 3, 5, 10$ and 20 wt%) doped $\text{Ni}_{0.4}\text{Co}_{0.25}\text{Zn}_{0.35}\text{Fe}_2\text{O}_4$ ferrite ceramics sintered at 1100 °C for 2 hours [31]. Permissions in Appendix A.

Figure 4-2 (B) shows an increase in both theoretically predicted (5.41 g/cm^3 ($x=0$ wt%) to 5.47 g/cm^3 ($x=3$ wt%)) and experimentally measured densities (4.29 g/cm^3 ($x=0$ wt%) to 5.33 g/cm^3 ($x=3$ wt%)) respectively because of the increase in CuO concentration in the composition.

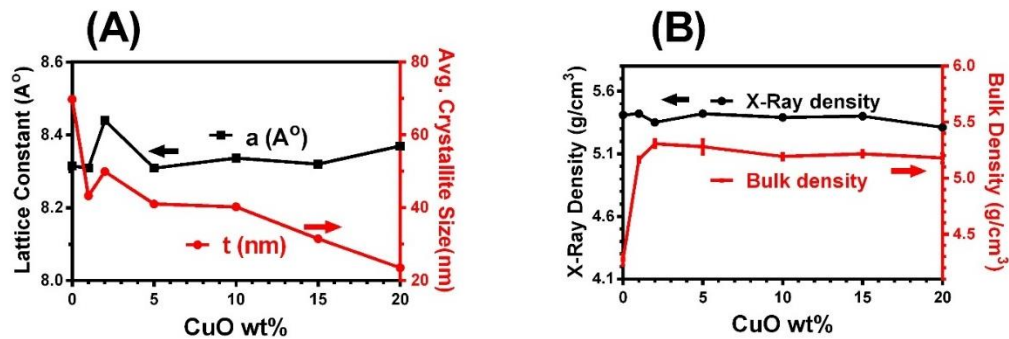


Figure 4-2 Variation of (A) lattice constant and average crystallite size in response to varied CuO concentrations; (B) X-ray density and bulk density with respect to CuO concentration for $\text{Ni}_{0.4}\text{Co}_{0.25}\text{Zn}_{0.35}\text{Fe}_2\text{O}_4$ ferrite [31]. Permissions in Appendix A.

Table 4-1 X-ray density, d-spacing, lattice constant, average crystallite size, and porosity of $\text{Ni}_{0.4}\text{Co}_{0.25}\text{Zn}_{0.35}\text{Fe}_2\text{O}_4$ samples sintered at 1100 °C for 2 hours for x= 0 wt% to 20 wt%

Sample	X-Ray Density (g/cm ³)	d-spacing (Å ^o)	Lattice Constant (Å ^o)	Average Crystallite Size (nm)	Porosity (%)
0%	5.41	2.940	8.315	Average Crystallite Size (nm)	Porosity (%)
1%	5.42	2.938	8.309	69 ± 5	21.01 ± 0.920
3%	5.47	2.929	8.440	44 ± 7	4.67 ± 0.403
5%	5.42	2.938	8.309	48 ± 7	1.99 ± 0.532
10%	5.39	2.947	8.336	41 ± 5	2.58 ± 1.152
15%	5.40	2.941	8.320	40 ± 5	3.64 ± 0.554
20%	5.41	2.940	8.317	31 ± 5	3.15 ± 0.553

4.3.1.2 Scanning Electron Microscopy (SEM) Analysis

Figure 4-3 shows the SEM micrograph of CuO doped (x=0 wt% to 20 wt%) Ni-Co-Zn samples sintered at 1100 °C. It was observed that average grain size gradually increased with CuO concentration in the composition. Narrow grain size distribution was observed for samples doped with less than 3 wt% CuO as compared to other samples doped with higher CuO concentrations as shown in Table 4-2 [31]. In fact, non-uniform grain size distribution was observed at higher CuO concentrations (>5%). Average grain size was drastically increased from 200-600 nm to 15 - 40 μm for undoped Ni-Co-Zn ferrite (x=0 wt%) and heavily doped sample (x=20 wt%), respectively. Porosity decreased along with an increase in grain size specially at higher CuO concentrations.

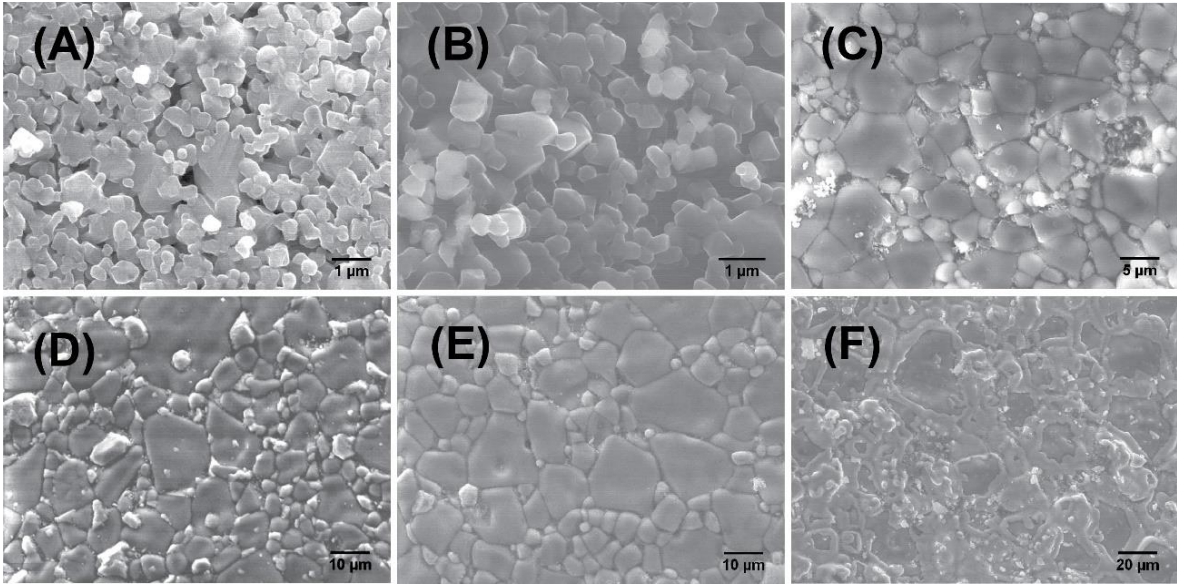


Figure 4-3 SEM micrographs of CuO ($x=0, 1, 3, 5, 10$ and 20 wt%) doped $\text{Ni}_{0.4}\text{Co}_{0.25}\text{Zn}_{0.35}\text{Fe}_2\text{O}_4$ ferrite ceramics sintered at 1100°C for 2 hours, including ferrite doped with CuO at varied levels: (A) $x=0$ wt% (undoped); (B) $x=1$ wt%; (C) $x=3$ wt%; (D) $x=5$ wt%; (E) $x=10$ wt%; (F) $x=20$ wt [31] %. Permissions in Appendix A.

It mainly results from the decrease in intragranular porosity, which decreases from 20.71 % for an undoped sample ($x=0$ wt%) to 1.4 % for a heavily doped counterpart ($x=20$ wt%). Copper substitution increases the bulk density from 4.27 g/cm^3 ($x=0$ wt%) to 5.33 g/cm^3 ($x=3$ wt%), which are then decreased to 5.24 g/cm^3 ($x=20$ wt%) as shown in Table 4-2. This can be attributed to an increase in grain size and the reduction in porosity with increasing CuO concentration, as reactivity of the grains with each other has led to mergers and formation of larger grains. The presence of copper oxide in the composition during sintering facilitates grain growth and reduction in porosity, which in turn play important role for enhancing dynamic magnetic properties [31].

Table 4-2 Bulk density and grain size of $\text{Ni}_{0.4}\text{Co}_{0.25}\text{Zn}_{0.35}\text{Fe}_2\text{O}_4$ samples sintered at 1100 °C, 2 hours for different CuO concentrations (x= 0 wt% to 20 wt%)

Sample	Bulk Density(g/cm³)	Grain Size (μm)
0%	4.29	0.2-0.6
1%	5.15	0.4-0.8
3%	5.33	2-9
5%	5.25	5-20
10%	5.14	15-30
15%	5.22	18-25
20%	5.24	15-40

4.3.2 Dynamic Magnetic Properties

The variation of complex permeability spectra for CuO doped (x=0 wt% to 20 wt%) Ni-Co-Zn ferrite samples sintered at 1100 °C for 2 hours are shown in Figure 4-4 (A-C). It is noted that both real (μ') and imaginary part (μ'') of the permeability increases with CuO concentration until x=3 wt%, because of the increase in grain size and density with increasing CuO concentration [31]. Afterwards, both real and imaginary part of the complex permeability decreases steadily with further increase of CuO dopants. Between x=0 wt% and x=3 wt%, the real part of permeability increases from 3.87 to 10.9, whereas the imaginary part of permeability increases from 1.38 to 1.59, which were tested at 400 MHz frequency. With further increase in CuO content, the real part of permeability decreases from 10.9 (x=3 wt%) to 3.77 (x=20 wt%) along with a decrease in the imaginary part from 1.59 (x=3 wt%) to 0.06 (x=20 wt%). The relative magnetic permeability of ferrites has shown a positive correlation with grain size.

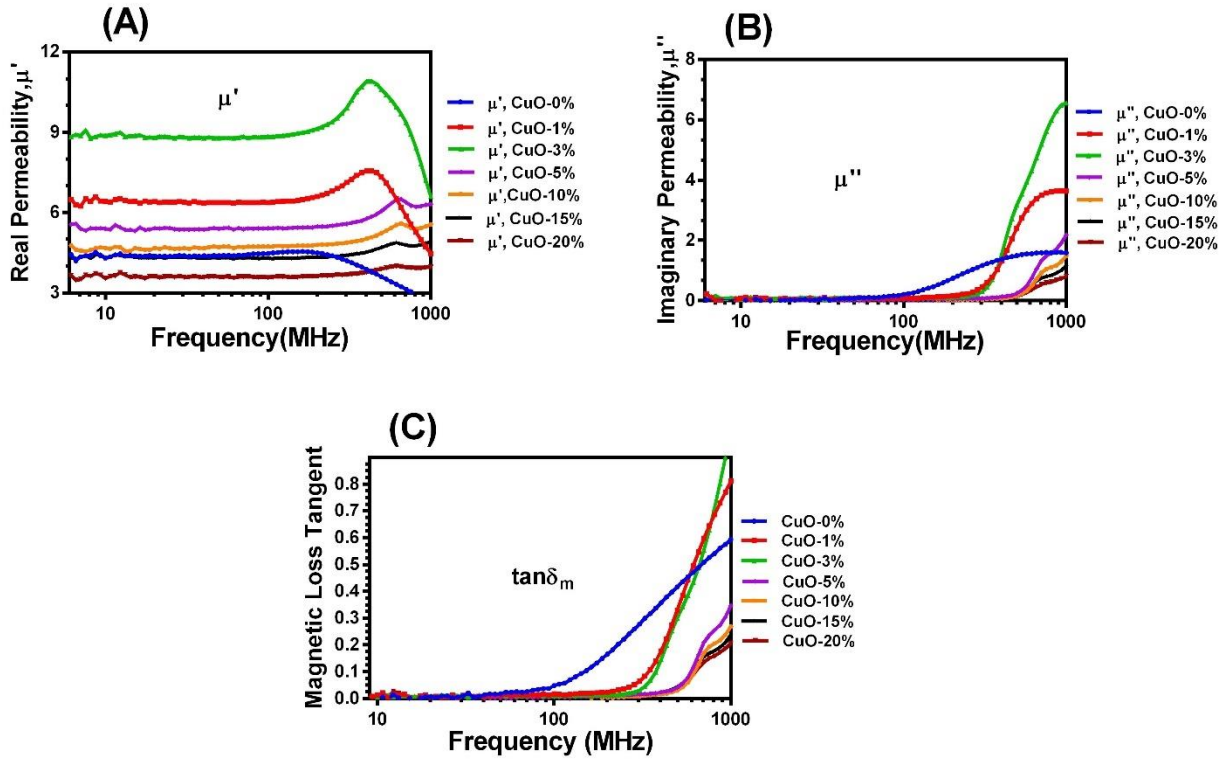


Figure 4-4 Relative complex permeability spectra of $\text{Ni}_{0.4}\text{Co}_{0.25}\text{Zn}_{0.35}\text{Fe}_2\text{O}_4$ samples sintered at $1100\text{ }^\circ\text{C}$ for 2 hours: (A) real part of complex permeability; (B) imaginary part of complex permeability; (C) magnetic loss tangent [31]. Permissions in Appendix A.

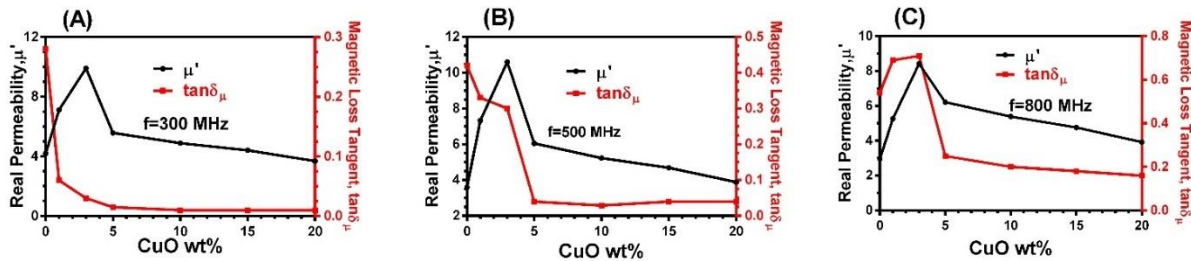


Figure 4-5 Real part of permeability and magnetic loss tangent of $\text{Ni}_{0.4}\text{Co}_{0.25}\text{Zn}_{0.35}\text{Fe}_2\text{O}_4$ samples sintered at $1100\text{ }^\circ\text{C}$ for 2 hours with respect to CuO concentrations at different frequencies of: (A) 300 MHz; (B) 500 MHz; and (C) 800 MHz [31]. Permissions in Appendix A.

The magnetic loss tangent of the samples is also depicted in Figure 4-4 (C), which showed pronounced decrease in values from undoped sample ($x=0\text{ wt}\%$) to doped samples ($x=20\text{ wt}\%$). It is noted that magnetic loss tangent at 400 MHz decreases from 0.36 ($x=0\text{ wt}\%$) to 0.02 ($x=20\text{ wt}\%$). Magnetic loss follows a different trend than imaginary part of the permeability. This

indicates that copper helps in lowering of magnetic loss, as it acts as a sintering aid during the sintering process of ferrite samples, which densifies sample while reducing pore volume. The values of real part of permeability, magnetic loss tangent and relative loss factor are tabulated in Table 4-4 at different frequencies [31].

The real part of permeability and magnetic loss tangent at different Cu concentrations for 300 MHz, 500 MHz and 800 MHz are depicted in Figure 4-5 (A-C). It is observed that real part of permeability follows the same trend at higher frequencies above 500 MHz, it decreases after an initial increase for all frequencies. On the contrary, magnetic loss tangent decreases gradually and drop to very low values at frequencies up to 500 MHz for samples doped with a high concentration of CuO. As frequency increases above 500 MHz, high magnetic loss tangent was observed at low concentration of CuO dopants as compared to the higher concentrations (Figure 4-5 C). The real part of permeability μ' remains almost constant in a certain range of frequency (between 100 to 500 MHz depending on the composition) and then begins to decrease sharply at higher frequencies. The imaginary part of permeability μ'' gradually increases with frequency and attains the highest value at resonance frequency, whereas the real part of permeability rapidly decreases. This feature resembles a typical relaxation characteristic of natural resonance frequency; the frequency at which μ'' form a broad peak is known as resonance frequency f_o . Resonance frequency is a key limiting factor for magnetic materials to be utilized efficiently at frequencies below this value. f_o was observed towards the lower frequency for samples prepared with a low concentration of CuO dopant, x, 3 wt%. And beyond x=3 wt %, f_o further shifted to higher frequency range above 1 GHz. This behavior agrees well with Globus model, which relates the relative permeability to the resonance frequency [80] as shown below by equation 17

$$\sqrt{(\mu_r - 1)}f_o = constant \quad (17)$$

Complex permeability spectra of polycrystalline ferrite are dependent on two different magnetizing phenomena: the spin rotational magnetization and domain wall motion. The complex permeability of polycrystalline ferrites is highly dependent on the microstructure of the ferrite powder [81]. In previous studies, it was reported that spin rotational component is dependent only on post sintering density of the ferrite, while domain wall motion is dependent on post sintering density and the grain size of the ferrite. It was also reported that domain wall contribution lies only at lower frequency range while complex permeability at higher frequency range above 100 MHz is governed by spin rotation component [65]. Large grains have a greater number of domain walls, which in turn contribute to increase in magnetization, thus leading to increased permeability. In this study, for unsubstituted sample ($x=0$ wt%), low value of permeability is realized as domain wall movement is absent because of single domain particles. On the contrary, the multi-domain particles of grain size $\geq 3 \mu\text{m}$ are observed for CuO substituted samples that result in higher domain wall contribution, thus increasing the permeability [29].

It was noted that grain size increases with CuO concentration up to a certain weight percent (up to $x= 3\text{wt}\%$), beyond which segregation of CuO at grain boundaries and increase in intragranular porosity discontinuous grain growth (seen in SEM images-Figure 4-3) can be observed that have a direct impact on permeability [78]. Another contributing factor is the density, which also aids the enhancement of permeability due to the reduction of demagnetizing field that is attributed to decrease in pore volume. As shown in Figure 4-5 (C), it was observed that permeability decreases with frequency, especially for high frequencies > 500 MHz. Basically, the presence of nonmagnetic impurities located between grains and intragranular pores can hinder the movement of spin and domain walls, which in turn lowers the permeability and increases the magnetic loss [31].

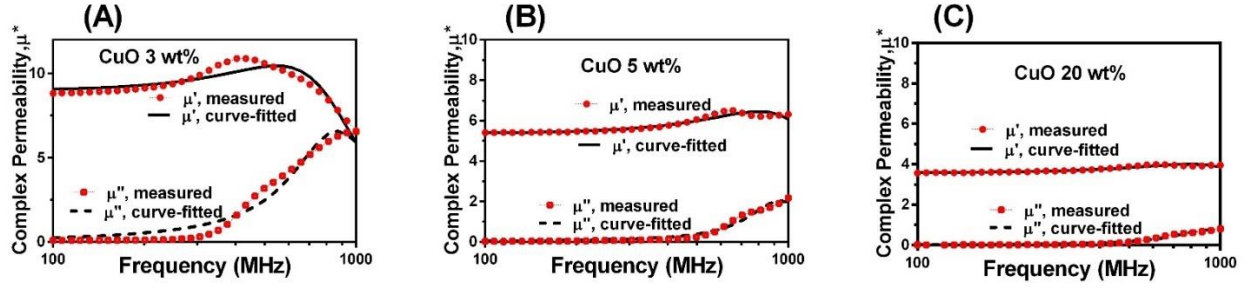


Figure 4-6 Fitted complex permeability spectra of the $\text{Ni}_{0.4}\text{Co}_{0.25}\text{Zn}_{0.35}\text{Fe}_2\text{O}_4$ samples with varied CuO dopant concentrations, where solid lines are fitting curves: (A) $x= 3$ wt%; (B) $x= 5$ wt%; (C) $x= 20$ wt% [31]. Permissions in Appendix A.

With an increase in CuO concentration, both the real and imaginary part of permeability initially increases and then decreases with frequencies. In order to determine the model-predicted resonance frequency, the relative complex permeability spectra in Figure 4-4 is fitted with Kittel Equation (equations 18 and 19) using three fitting parameters: where χ_o is the static magnetic susceptibility; f_o is the resonant frequency; and α is the damping factor [82, 83].

$$\mu_r(f) = 1 + \frac{\chi_o(1+i\alpha\frac{f}{f_o})}{(1+i\alpha\frac{f}{f_o})^2+(\frac{f}{f_o})^2} \quad (18)$$

$$\mu_r(f) = 1 + \frac{\chi_o f_o^2 (f_o^2 - (1-\alpha)f^2)}{(f_o^2 - (1+\alpha^2)f^2)^2 + 4\alpha^2 f_o^2 f^2} - i \frac{\chi_o \alpha f_o f (f_o^2 + (1+\alpha)f^2)}{(f_o^2 - (1+\alpha^2)f^2)^2 + 4\alpha^2 f_o^2 f^2} \quad (19)$$

The measured and fitted permeability spectra of CuO substituted ($x= 3, 5$ and 20 wt%) ferrite samples are shown in Figure 4-6 (A-C). Table 4-3 listed the parameters obtained for samples with different CuO concentration. The calculated permeability (solid line) in Figure 4-6 is in good agreement with the measured complex permeability (circled line). Similar to the measurements, unsubstituted/undoped samples ($x=0$ wt%) have small pores, small average grains along with lowest sintering density as listed in Table 4-2, which leads to large demagnetizing field. As a result, static magnetic susceptibility (χ_o) is the lowest (e.g., 3.28 for $x=0$ wt% vs 7.99 for $x=3$ wt% samples).

Table 4-3 Fitted parameters extracted from the $\text{Ni}_{0.4}\text{Co}_{0.25}\text{Zn}_{0.35}\text{Fe}_2\text{O}_4$ samples for $x= 0$ wt% to 20 wt%

Sample	Static magnetic susceptibility (χ_o)	Resonant frequency (f_o) GHz	Damping coefficient (α)
0%	3.28	1.30	1.670
1%	5.52	2.09	1.495
3%	7.99	1.98	1.274
5%	4.37	2.56	1.135
10%	3.71	2.71	1.163
15%	3.29	1.53	0.542
20%	4.48	2.39	1.043

Since the pore volume decreases and the average grain size increases with increasing CuO concentrations, demagnetizing field decreases and χ_o increases, accordingly. The further increase of CuO concentration beyond a certain threshold (i.e., $x=3$ wt%) cause inhomogeneous microstructure that is represented by a large grain size distribution, thus creating closed pores as well as long and wide grain boundaries [31]. As a result, the demagnetizing field increases while magnetic susceptibility(χ_o) decreases [84]. Similarly, damping factor (α) also decreases first then increases in response to an increasing concentration of Cu. The generation of closed pores also increase the impediment to domain wall motion, which in turn increases the damping factor. The increase in resonant frequency f_o with CuO concentration can be ascribed to reduced demagnetizing fields caused by the grain size and pore distribution.

4.3.3 Dielectric Properties

To characterize the dielectric characteristics of prepared ferrite samples, complex permittivity spectra was measured for CuO doped ($x=0$ wt% to 20 wt%) Ni-Co-Zn ferrite samples sintered at 1100 °C for 2 hours as shown in Figure 4-7 (A-B).

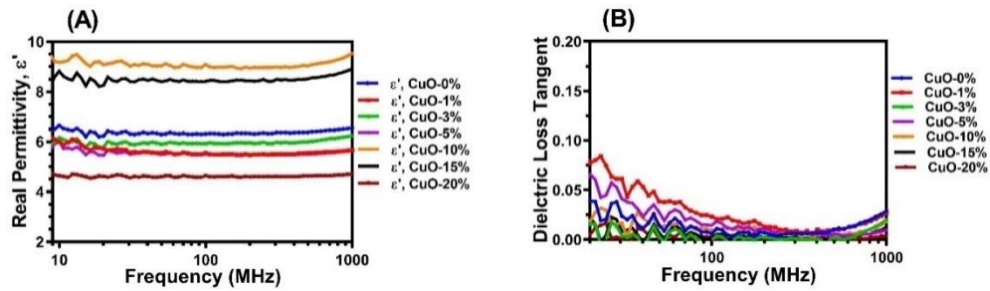


Figure 4-7 Permittivity spectra of $\text{Ni}_{0.4}\text{Co}_{0.25}\text{Zn}_{0.35}\text{Fe}_2\text{O}_4$ samples sintered at 1100 °C for 2 hours: (A) dielectric permittivity; (B) dielectric loss tangent [31]. Permissions in Appendix A.

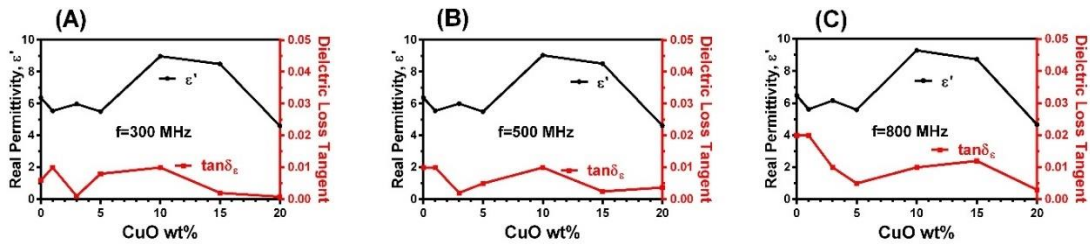


Figure 4-8 Real part of permittivity and dielectric loss tangent of $\text{Ni}_{0.4}\text{Co}_{0.25}\text{Zn}_{0.35}\text{Fe}_2\text{O}_4$ samples sintered at 1100 °C for 2 hours with respect to CuO concentration at different frequencies: (A) 300 MHz; (B) 500 MHz; (C) 1 GHz [31]. Permissions in Appendix A.

It is noted that permittivity remains constant across the full range of measured frequencies, which is dissimilar to bulk ferrites in the RF and microwave frequency region. The real part of permittivity (ϵ') shows some noticeable variation with different CuO concentration, while imaginary part of permittivity (ϵ'') for different samples show small variation in the frequency range from 1 MHz to 1 GHz [31]. Permittivity increases with an increase in CuO concentration until $x=10$ wt%, beyond which it decreases with further increased CuO concentrations.

Table 4-4 Magnetic and dielectric properties of $\text{Ni}_{0.4}\text{Co}_{0.25}\text{Zn}_{0.35}\text{Fe}_2\text{O}_4$ samples sintered at 1100 °C for 2 hours for x= 0 wt% to 20 wt% measured at different frequencies

Sample	Parameters	300 MHz	500 MHz	800 MHz
0 wt%	μ'	4.2	3.6	2.95
	$\tan\delta_\mu$	0.28	0.42	0.54
	$\tan\delta_\mu/\mu'$	0.066	0.116	0.183
	ϵ'	6.37	6.38	6.49
	$\tan\delta_\epsilon$	0.006	0.01	0.02
	$\tan\delta_\epsilon/\epsilon'$	0.0009	0.0015	0.0030
1 wt%	μ'	7.12	7.33	5.26
	$\tan\delta_\mu$	0.06	0.33	0.69
	$\tan\delta_\mu/\mu'$	0.008	0.045	0.131
	ϵ'	5.50	5.55	5.61
	$\tan\delta_\epsilon$	0.01	0.01	0.02
	$\tan\delta_\epsilon/\epsilon'$	0.0018	0.0018	0.0035
3 wt%	μ'	9.91	10.6	8.42
	$\tan\delta_\mu$	0.03	0.30	0.70
	$\tan\delta_\mu/\mu'$	0.003	0.028	0.080
	ϵ'	5.98	6.0	6.16
	$\tan\delta_\epsilon$	0.001	0.002	0.01
	$\tan\delta_\epsilon/\epsilon'$	0.0001	0.0003	0.0016
5 wt%	μ'	5.57	6.05	6.21
	$\tan\delta_\mu$	0.015	0.04	0.25
	$\tan\delta_\mu/\mu'$	0.002	0.006	0.040
	ϵ'	5.51	5.50	5.59
	$\tan\delta_\epsilon$	0.008	0.005	0.005
	$\tan\delta_\epsilon/\epsilon'$	0.0014	0.0009	0.0008
10 wt%	μ'	4.88	5.23	5.39
	$\tan\delta_\mu$	0.01	0.03	0.20
	$\tan\delta_\mu/\mu'$	0.002	0.006	0.037
	ϵ'	8.98	9.04	9.29
	$\tan\delta_\epsilon$	0.01	0.01	0.01
	$\tan\delta_\epsilon/\epsilon'$	0.0011	0.0011	0.0010
15 wt%	μ'	4.41	4.69	4.76
	$\tan\delta_\mu$	0.01	0.04	0.18
	$\tan\delta_\mu/\mu'$	0.002	0.008	0.037
	ϵ'	8.49	8.51	8.73
	$\tan\delta_\epsilon$	0.0028	0.0025	0.012
	$\tan\delta_\epsilon/\epsilon'$	0.0003	0.0003	0.0013
20 wt%	μ'	3.68	3.89	3.92
	$\tan\delta_\mu$	0.01	0.04	0.16
	$\tan\delta_\mu/\mu'$	0.003	0.01	0.040
	ϵ'	4.61	4.62	4.66
	$\tan\delta_\epsilon$	0.0002	0.0004	0.003
	$\tan\delta_\epsilon/\epsilon'$	0.00004	0.00008	0.0006

Substitution of Cu ions in the spinel lattice enhances the dielectric polarization of the material, thus increasing the permittivity (6.4 to 9). Furthermore, an increase in grain size causes an increase in grain-to-grain boundary thickness ratio, which in turn increases permittivity for samples doped with higher CuO concentrations [31]. At very higher CuO concentration ($x > 10$ wt%), permittivity starts to drop noticeably from 9 to 4.5 mainly because of nonuniform grain sizes or large grain size distribution that results in low permittivity. The dielectric loss also exhibits a similar dependence on CuO concentration by decreasing with Cu concentration after an initial increase to reach a peak value. Figure 4-8 (A-C) shows the real part of permittivity and dielectric loss tangent at frequency of 300 MHz, 800 MHz, and 1 GHz. The dielectric and magnetic properties of all samples are summarized in Table 4-4.

4.3.4 Summary

Overall, CuO doped Ni-Co-Zn spinel ferrites with a wide range of CuO dopant concentrations from 0 wt% to 20 wt% have been successfully prepared using solid state synthesis method. The quantity of CuO dopants is optimized to modify the microstructure and enhance the magneto-electric properties of the sintered ferrite powders, while lowering the magnetic and dielectric losses. CuO dopant up to 3wt% has led to uniform grain growth and increased density that result in substantial improvement in magnetic properties. At 400 MHz, 3wt% doped sample has exhibited ~180 % increase in permeability along with ~60% reduction in magnetic loss tangent. Further increase of the CuO dopant concentration lowered the magnetic permeability and shifted the resonance frequency into GHz range, which has shown potential to expand the utilization of the ferrite powders for RF and microwave applications at GHz frequencies [31]. Moreover, dielectric properties (permittivity) are also stable over the frequency range. In fact, an improvement in permittivity for concentrations up to 10 wt% doping has been observed. For

example, 10wt% CuO doped specimen has exhibited ~ 40% higher permittivity as compared to that of undoped samples.

4.4 Effect of Cobalt Oxide (Co₂O₃) Substitution on Ni-Co-Zn Ferrite Powders

Complex magnetic and dielectric spectra of Co₂O₃-substituted (x=0.10 to 25) in Ni_{0.65-x}Co_xZn_{0.35}Fe₂O_{4.1} ferrites at very high frequencies and ultra-high frequencies have been studied in this section. The Ni-Co-Zn ferrites were prepared by the conventional ceramic synthesis process by using Co substitution in Ni. The synthesized powders were doped with 0.2 wt% Bi₂O₃ and 10 wt% of CuO for 2 hour ball milling at 560 rpm. The cobalt substitution in Ni-Zn ferrite has led to the formation of soft ferrites with high permeability and permittivity and low magnetic and dielectric losses, which are desirable for applications like biomedical implantable antennas and unmanned aerial vehicle applications at very high frequencies and ultra high frequencies. Addition of Co₂O₃ decreases the magnetic loss followed by increase in resonance frequency.

4.4.1 Microstructure Analysis

The phase composition of calcined ferrite powders was analyzed by XRD and the morphology of the sintered toroidal samples was examined by scanning electron microscopy.

4.4.1.1 X-Ray Diffraction (XRD) Analysis

Figure 4-9 shows the XRD pattern of Ni_{0.65-x}Co_xZn_{0.35}Fe₂O_{4.1} (x=0.10 to 0.25) powders sintered at 1100 °C for 2 hours. A single-phase spinel structure was observed for all doped samples, while no extra unaccounted peak was observed in the X-ray pattern, thus confirming the absence of secondary phase in the structure. The strongest peak observed correlates to (311) crystal orientation.

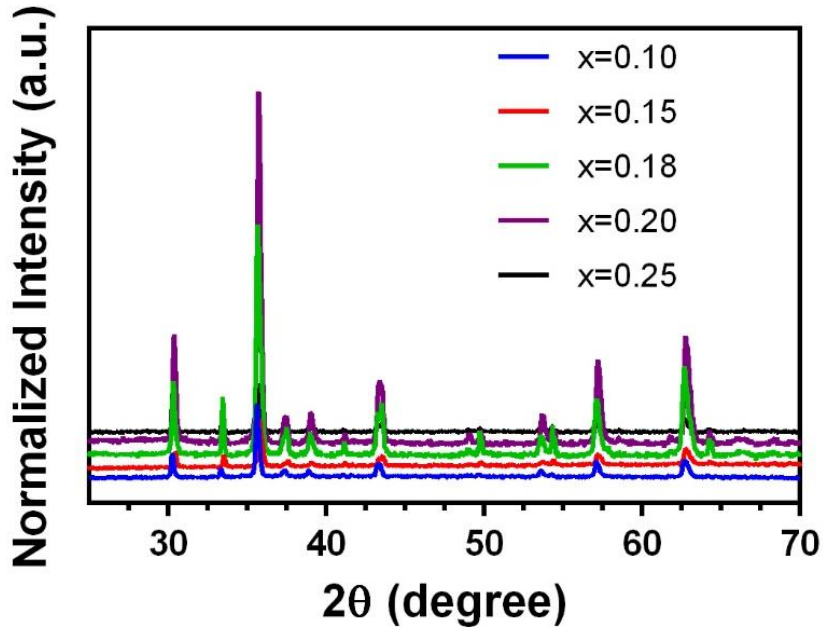


Figure 4-9 X-ray diffraction patterns of $\text{Ni}_{0.65-x}\text{Co}_x\text{Zn}_{0.35}\text{Fe}_2\text{O}_{4.1}$ ($x=0.10$ to 0.25) powders sintered at $1100\text{ }^\circ\text{C}$ for 2 hours.

4.4.1.2 Scanning Electron Microscopy (SEM) Analysis

To observe the effect of Co_2O_3 on the grain growth of the toroidal samples, SEM images were taken. Figure 4-10 (a)-(e) shows the microstructure pattern of $\text{Ni}_{0.65-x}\text{Co}_x\text{Zn}_{0.35}\text{Fe}_2\text{O}_{4.1}$ ($x=0.10$ to 0.25) toroidal specimens sintered at $1100\text{ }^\circ\text{C}$ for 2 hours. It can be observed that the grain size decreases slightly with increase in Co_2O_3 concentration from $x=0.10$ to $x=0.25$. The average grain size and grain sizes distribution were analyzed using ImageJ software with a sample area consists of 50 grains. Variation of average grain size with cobalt substitution is tabulated in Table 4-5. Particle's agglomeration can be observed with Co_2O_3 doping.

Table 4-5 Grain size of $\text{Ni}_{0.65-x}\text{Co}_x\text{Zn}_{0.35}\text{Fe}_2\text{O}_{4.1}$ samples sintered at 1100 °C, 2 hours for different Co_2O_3 concentrations ($x= 0.10$ to 0.25)

Sample	Particle Size (μm)
$x=0.10$	10-35
$x=0.15$	10-30
$x=0.18$	12-28
$x=0.20$	10-20
$x=0.25$	2-9

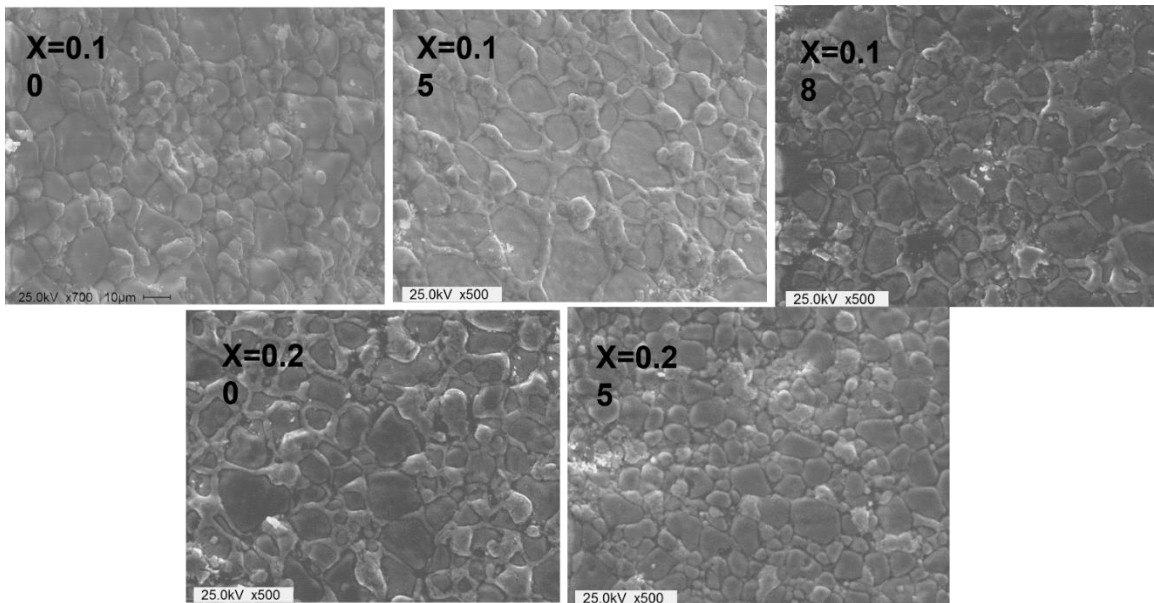


Figure 4-10 SEM micrographs of $\text{Ni}_{0.65-x}\text{Co}_x\text{Zn}_{0.35}\text{Fe}_2\text{O}_{4.1}$ ($x=0.10$ to 0.25) powders sintered at 1100 °C for 2 hours.

4.4.2 Dynamic Magnetic Properties

To study the effect of Co_2O_3 substitution on dynamic magnetic properties, complex permeability spectra was measured for all Co_2O_3 substituted toroidal samples using RF/Impedance analyzer between 1 MHz to 1 GHz frequency range.

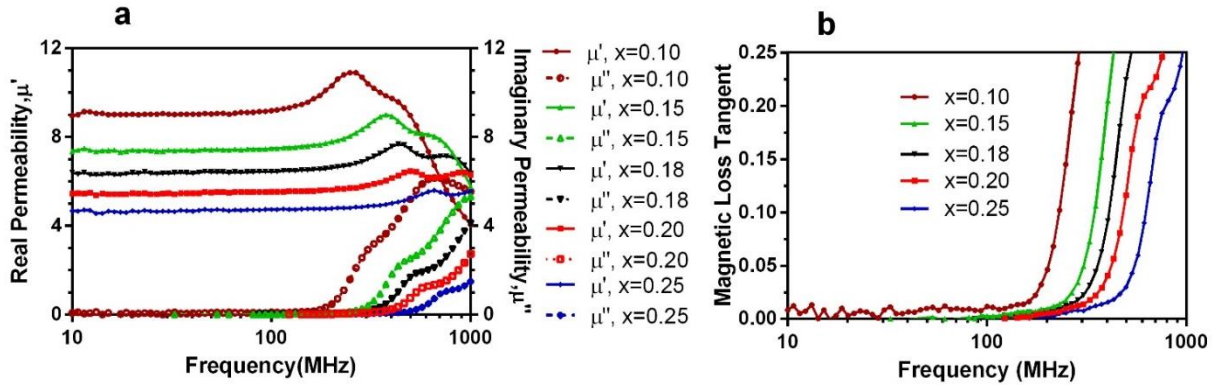


Figure 4-11 Magnetic properties of Co_2O_3 -substituted ($x = 0.10, 0.15, 0.18, 0.20$ and 0.25) $\text{Ni}_{0.65-x}\text{Co}_x\text{Zn}_{0.35}\text{Fe}_2\text{O}_4$ ferrite toroid samples versus frequency sintered at 1100°C (a) real and imaginary part of permeability; (b) magnetic loss tangent.

Figure 4-11 shows the complex permeability spectra and magnetic loss tangent for all the Co_2O_3 doping toroidal specimens. It is observed that real and imaginary part of permeability decreases with increase in Co_2O_3 concentration. It can be attributed to increase in domain wall energy and magneto crystalline anisotropy constant. With increase in Co^{2+} ions at the octahedral site of the spinel structure increase the magneto crystalline anisotropy, in turn decreases the permeability.

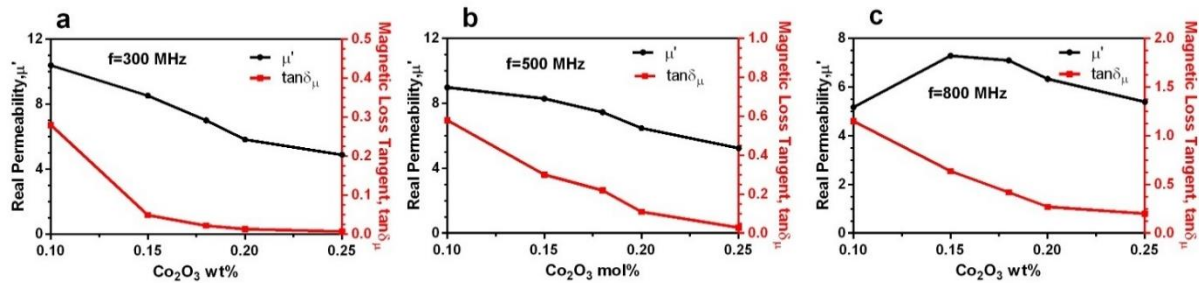


Figure 4-12 Real part of permeability and magnetic loss tangent of Co_2O_3 -substituted ($x = 0.10, 0.15, 0.18, 0.20$ and 0.25) $\text{Ni}_{0.65-x}\text{Co}_x\text{Zn}_{0.35}\text{Fe}_2\text{O}_4$ ferrite toroid samples with respect to Co_2O_3 concentrations at different frequencies of: (A) 300 MHz; (B) 500 MHz; and (C) 800 MHz.

From $x=0.10$ to $x=0.25$, the real part of permeability decreases from 10.4 to 4.88, whereas the imaginary part of permeability decreases from 2.92 to 0.04, at 300 MHz frequency. The

magnetic loss tangent of the samples depicted in Figure 4-11 (b), which also showed pronounced decrease in values from Co_2O_3 doping ($x=0.10$ wt%) to ($x= 0.25$ wt%). It is noted that magnetic loss tangent at 300 MHz decreases from 0.28 ($x=0.10$) to 0.007 ($x= 0.25$).

It is known that permeability depends on the microstructure and composition of the material. As it is observed in the microstructure (SEM Figure 4-10) of the Co_2O_3 doped samples ($x=0.10$ w) to ($x= 0.25$), grain size decreases for $x=0.10$ to $x=0.25$, permeability follows the same trend. It is also known that cobalt substitution increases the magnetic anisotropy and magnetostriction in the composition and permeability follows the inverse relation with them. Figure 4-12 (a)-(b) shows the real part of permeability and magnetic loss tangent at different Co_2O_3 concentrations for 300 MHz, 500 MHz and 800 MHz. It is observed that real part of permeability decreases from 10.4 to 5.17 at lower doping of Co_2O_3 ($x=0.10$) at frequency above 500 MHz. The other doping percentages also follows the same trend. The magnetic loss tangent follows the same trend at higher frequencies above 500 MHz for all cobalt dopings. The values of real part of permeability and permittivity, magnetic and dielectric loss tangent and relative loss factor are tabulated in Table 4-6 at different frequencies.

4.4.3 Dielectric Properties

Figure 4-13 shows the variation of real part of permittivity and dielectric loss with frequency for all Co_2O_3 doped disc shaped specimens. It is observed that with increase in Co_2O_3 doping the real part of permittivity first decreases from $x=0.10$ ($\epsilon'=8.07$) to $x=0.15$ ($\epsilon'=5.55$), and then increases from $x=0.15$ ($\epsilon'=5.55$) to $x=0.25$ ($\epsilon'=9.04$) measured at 500 MHz. On the contrary, dielectric loss decreases for all samples from $x=0.10$ to $x=0.25$. This behavior can be attributed to that fact that at low concentration, of Co^{2+} ions replacing Ni^{2+} and Fe^{3+} ions at octahedral sites, which reduces the ratio of $\text{Fe}^{2+}/\text{Fe}^{3+}$, consequently, the polarization decreases. While at higher

concentration, Co^{2+} ions are occupying the A site which increases the ration of $\text{Fe}^{2+}/\text{Fe}^{3+}$ ions, hence, dielectric properties increase.

Table 4-6 Magnetic and dielectric properties of $\text{Ni}_{0.65}\text{Co}_x\text{Zn}_{0.35}\text{Fe}_2\text{O}_4$ samples sintered at 1100 °C for 2 hours for $x= 0.10$ to 0.25 measured at different frequencies

Sample	Parameters	300 MHz	500 MHz	800 MHz
0.10 wt%	μ'	10.4	8.98	5.17
	$\tan\delta_\mu$	0.28	0.57	1.1
	$\tan\delta_\mu/\mu'$	0.006	0.063	0.191
	ϵ'	8.06	8.07	8.15
	$\tan\delta_\epsilon$	0.02	0.03	0.04
	$\tan\delta_\epsilon/\epsilon'$	0.002	0.0037	0.0049
0.15 wt%	μ'	8.53	8.29	7.28
	$\tan\delta_\mu$	0.05	0.30	0.63
	$\tan\delta_\mu/\mu'$	0.005	0.036	0.086
	ϵ'	5.51	5.55	5.66
	$\tan\delta_\epsilon$	0.01	0.02	0.02
	$\tan\delta_\epsilon/\epsilon'$	0.0018	0.0036	0.0035
0.18 wt%	μ'	7.0	7.45	7.09
	$\tan\delta_\mu$	0.02	0.22	0.41
	$\tan\delta_\mu/\mu'$	0.0028	0.029	0.057
	ϵ'	8.26	8.37	8.62
	$\tan\delta_\epsilon$	0.01	0.01	0.02
	$\tan\delta_\epsilon/\epsilon'$	0.0012	0.0011	0.0023
0.20 wt%	μ'	5.82	6.46	6.33
	$\tan\delta_\mu$	0.012	0.11	0.27
	$\tan\delta_\mu/\mu'$	0.002	0.017	0.042
	ϵ'	7.61	7.69	7.90
	$\tan\delta_\epsilon$	0.008	0.01	0.01
	$\tan\delta_\epsilon/\epsilon'$	0.001	0.0013	0.0013
0.25 wt%	μ'	4.88	5.23	5.39
	$\tan\delta_\mu$	0.007	0.04	0.2
	$\tan\delta_\mu/\mu'$	0.001	0.007	0.037
	ϵ'	8.98	9.04	9.29
	$\tan\delta_\epsilon$	0.005	0.005	0.007
	$\tan\delta_\epsilon/\epsilon'$	0.0005	0.0005	0.0007

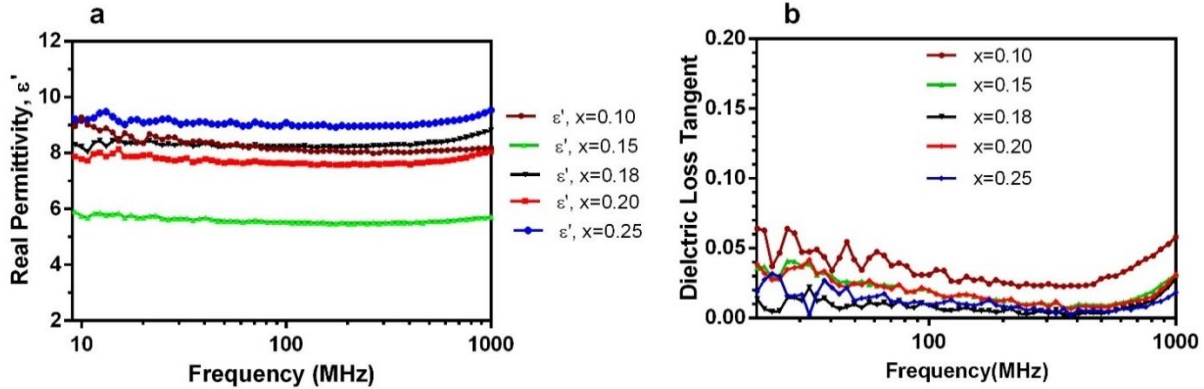


Figure 4-13 Dielectric properties of Co_2O_3 -substituted ($x= 0.10, 0.15, 0.18, 0.20$ and 0.25) $\text{Ni}_{0.65-x}\text{Co}_x\text{Zn}_{0.35}\text{Fe}_2\text{O}_{4.1}$ ferrite toroid samples versus frequency sintered at $1100\text{ }^\circ\text{C}$ (a) real part of permittivity; (b) dielectric loss tangent.

Dispersion type behavior is observed in all the samples. The real part of permittivity and dielectric loss observed is high at lower frequencies as compared to higher frequencies, however, are constant 100 MHz to 600 MHz, for all the doped samples. This phenomenon can be explained using Maxwell's model. The grains are dominant at higher frequency while grain boundaries are dominant at the lower frequencies. The dielectric properties are controlled by polarization mechanism between the metal ions in the structure. At lower frequencies, electrons hop towards grain boundaries and accumulate there, which in turn increases the dielectric properties while at higher frequencies, electrons turn the direction and number of charges decreases at grain boundaries which lowers the dielectric constant. In the present case, more dispersion is observed because of large number of grain boundaries at higher concentration of cobalt doping. Figure 4-14 (a-c) shows the real part of permittivity and dielectric loss tangent at frequency of 300 MHz, 500 MHz, and 800 MHz. Figure 4-15 (a-b) shows the permeability and permittivity spectra for $x=0.18$ sample. The real part of permeability values is approximately close to the values of permittivity for $x=0.18$ sample.

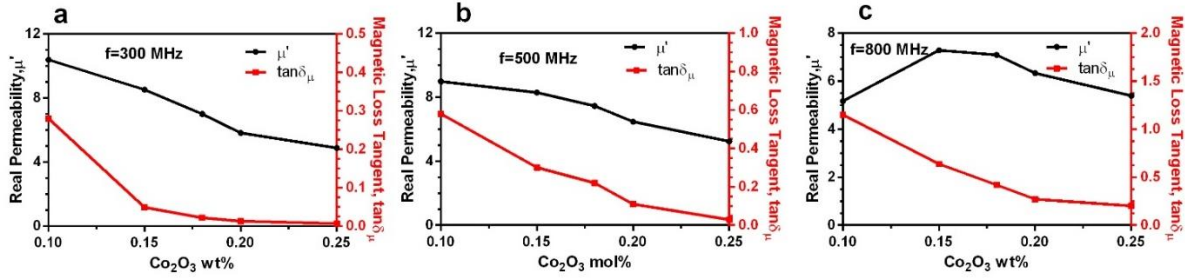


Figure 4-14 Real part of permittivity and dielectric loss tangent of Co_2O_3 -substituted ($x= 0.10, 0.15, 0.18, 0.20$ and 0.25) $\text{Ni}_{0.65-x}\text{Co}_x\text{Zn}_{0.35}\text{Fe}_2\text{O}_{4.1}$ ferrite toroid samples with respect to Co_2O_3 concentrations at different frequencies of: (A) 300 MHz; (B) 500 MHz; and (C) 800 MHz.

Variation of all four parameters real part of permittivity, permeability, dielectric losses and magnetic losses at 500 MHz for all doped samples are presented in Figure 4-16 (a-b). It is observed that the value of real permeability ($x=0.10, \mu' = 8.9$ and $x=0.18, \mu' = 7.4$) is close to the value of real permittivity ($x=0.10, \epsilon' = 8.1$ and $x=0.18, \epsilon' = 6.5$) at $x=0.10$ and 0.25 doping concentrations measured at 500 MHz. Magnetic and dielectric loss tangent decreases linearly for all concentrations ($x=0.10$ to $x=0.25$) of Co_2O_3 as shown in Figure 4-16 (b).

Figure 4-17 shows the calculated normalized impedance and miniaturization factor for all Co_2O_3 doping measured at 500 MHz. Miniaturization factor of 8.5 ($x=0.10$) and 7.9 ($x=0.18$) with refractive index of 1.1 ($x=0.10$) and 0.9 ($x=0.18$) were achieved respectively. The obtained miniaturization factor and refractive index will aid in reduction of the size of devices designed for high frequencies between 100 MHz to 500 MHz frequency range. Table 4-7 presents the different parameters for all Co_2O_3 doped samples measured at 500 MHz.

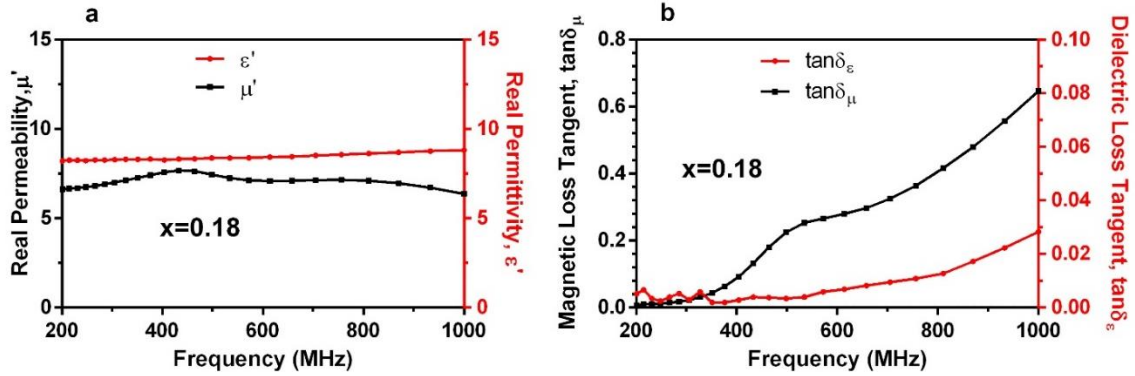


Figure 4-15 (a) Measured real part of permeability and permittivity spectra; (b) magnetic and dielectric loss tangent for x=0.18 doped sample versus frequency.

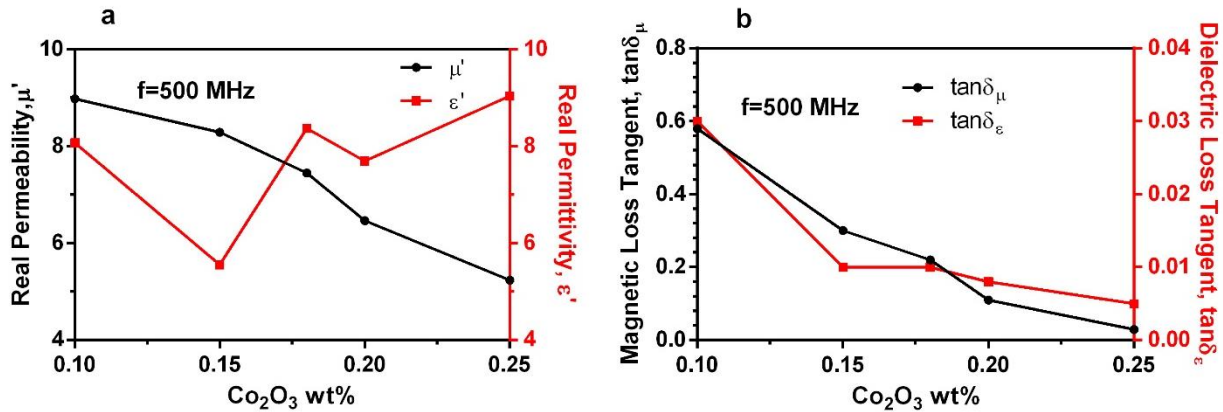


Figure 4-16 (a) Measured real part of permeability and permittivity spectra; (b) magnetic and dielectric loss tangent at 500 MHz for all Co₂O₃-substituted (x= 0.10, 0.15, 0.18, 0.20 and 0.25) Ni_{0.65-x}Co_xZn_{0.35}Fe₂O_{4.1} samples.

Table 4-7 Measured magnetic and dielectric parameters for all Co₂O₃ doped samples (x=0.10 to 0.25) at 500 MHz

Compos ition (wt%)	Real Permeabilit y (μ')	Magnetic loss ($\tan\delta_{\mu}$)	Real Permittivi ty (ϵ')	Dielectric loss ($\tan\delta_{\epsilon}$)	Refractive Index (η)	Norma lized Imped ance (Z_i/Z_0)
X=0.10	8.98	0.57	8.07	0.03	8.5	1.11
X=0.15	8.29	0.30	5.55	0.01	6.78	1.49
X=0.18	7.45	0.22	8.37	0.01	7.89	0.89
X=0.20	6.46	0.10	7.69	0.01	7.04	0.84
X=0.25	5.23	0.03	9.04	0.005	6.85	0.58

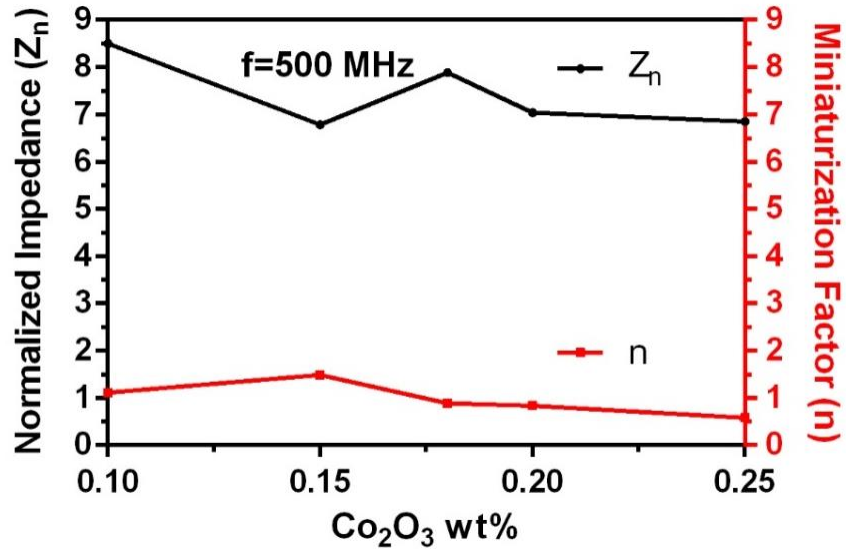


Figure 4-17 Calculated normalized impedance and miniaturization factor of Co_2O_3 -substituted ($x=0.10, 0.15, 0.18, 0.20$ and 0.25) $\text{Ni}_{0.65-x}\text{Co}_x\text{Zn}_{0.35}\text{Fe}_2\text{O}_{4.1}$ samples at 500 MHz.

4.4.4 Summary

Cobalt oxide doped $\text{Ni}_{0.65-x}\text{Co}_x\text{Zn}_{0.35}\text{Fe}_2\text{O}_{4.1}$ ferrites shows the significant enhancement in resonance frequency and decrease in the magnetic loss tangent for very high frequency and ultra high frequency applications. Comparable real part of permeability and permittivity with low magnetic and dielectric loss has been achieved at 300 MHz and 500 MHz frequencies for samples with $x=0.10$ and $x=0.18$ cobalt oxide doping. Real part of permeability decreases from 9.74 to 5.01 with an increase in Co_2O_3 mole percentage from $x=0.10$ to $x=0.25$, hence shifting the resonance frequency well over the 1 GHz. Magnetic loss tangent decreases from 0.40 to 0.01 with an increase in Co_2O_3 mole percentage from $x=0.10$ to $x=0.25$. Constant permittivity with low dielectric loss have been achieved for all doped samples at frequencies between 100 MHz and 800 MHz. Miniaturization factor of 8.5 and 7.9 have been observed for samples with $x=0.10$ and $x=0.18$ of cobalt oxide doping. Normalized impedance lies between 0.9 to 1.4 for all Co_2O_3 concentrations. These properties of the ferrite powder have shown promising properties for utilization in antennas

for biomedical devices (wearable sensors and body networked devices) and other, high frequency (HF), very high frequency (VHF) and ultra high frequency (UHF) applications by following the process methodology described herein.

Chapter 5: Ni-Co-Zn Composites Characterization and Their Application in Ultra High Frequency Antennas

5.1 Introduction

In this chapter microwave properties of Ni-Co-Zn/Epoxy composites are investigated for utilization as magnetic substrates of a planar antenna designed for biomedical devices operating at VHF and UHF ranges. The electromagnetic properties of the ferrite composites were characterized using a RF impedance analyzer and the results were compared with theoretical values calculated using different mixture models. In this work, two different patch antennas were designed using 3D electromagnetic simulations (ANSYS/HFSS software) and their performance were investigated under various parametric conditions. The first patch antenna design consists of a dielectric core of a commercial laminate (Rogers RO3010 laminated board) with copper claddings of 35 μm on both sides and the second patch antenna design consists of Ni-Co-Zn/Epoxy based magnetic substrate.

5.2 Measured Microwave Properties of Ni-Co-Zn Ferrites and Ni-Co-Zn/Epoxy Composite

Substrate

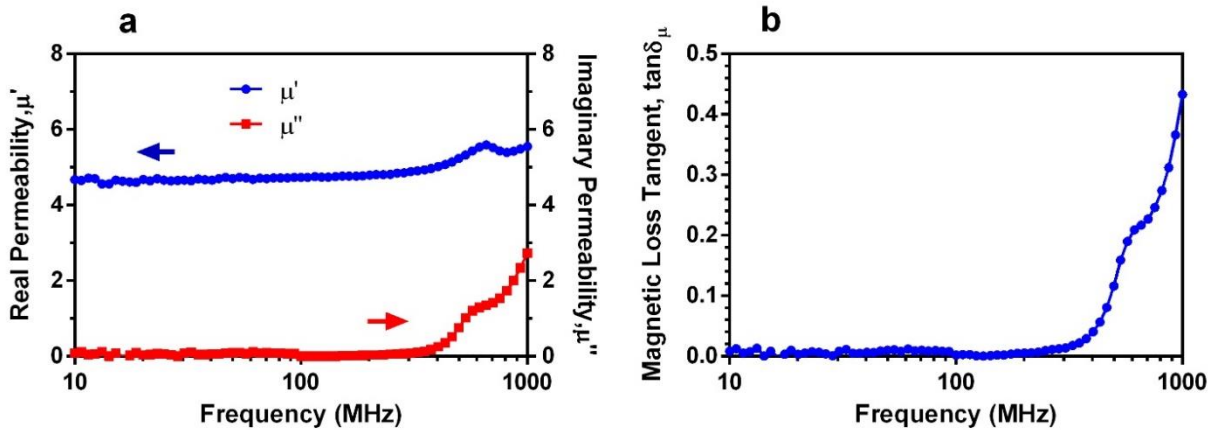


Figure 5-1 Magnetic properties versus frequency of $\text{Ni}_{0.4}\text{Co}_{0.25}\text{Zn}_{0.35}\text{Fe}_2\text{O}_{4.1}$ ferrite toroid samples sintered at 1100 °C for 2 hours including: (a) real and imaginary parts of permeability; (b) magnetic loss tangent.

In this section, microwave properties of Ni-Co-Zn ferrite and its composite are explored and characterized using a RF impedance/material analyzer (E4991A, Keysight, CA, USA) along with a magnetic material test fixture (Keysight 16454A, CA, USA) and dielectric test fixture (Keysight 16453A, CA, USA), respectively, over the frequency range between 1 MHz and 1 GHz. $\text{Ni}_{0.4}\text{Co}_{0.25}\text{Zn}_{0.35}\text{Fe}_2\text{O}_4$ ferrite with 5 wt% CuO and 0.2 wt% Bi_2O_3 dopants was used for the fabrication of magnetic composite sheets. All ferrite powders were sintered at 1100 °C for 2 hours and grinded in a ball milling machine for 1 hour before being used for magnetic composite sheet fabrication. Different volume percentage (33 vol%, 37 vol %, 47 vol %, 55 vol % and 66 vol %) of ferrite fillers were used for the magnetic composite substrate fabrication. Figure 5-1 shows the complex permeability and magnetic loss tangent of $\text{Ni}_{0.4}\text{Co}_{0.25}\text{Zn}_{0.35}\text{Fe}_2\text{O}_4$ ferrite that was sintered at 1100 °C for 2 hours. Figure 5-2 shows complex permittivity and dielectric loss tangent of the in-house prepared $\text{Ni}_{0.4}\text{Co}_{0.25}\text{Zn}_{0.35}\text{Fe}_2\text{O}_4$ ferrite.

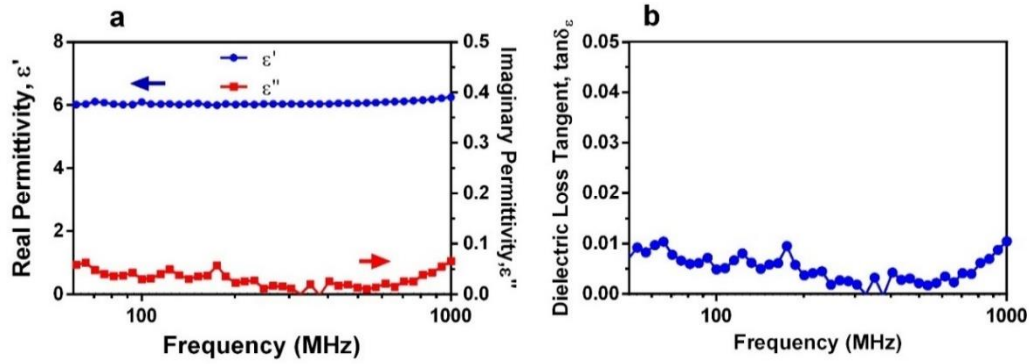


Figure 5-2 Dielectric properties versus frequency of $\text{Ni}_{0.4}\text{Co}_{0.25}\text{Zn}_{0.35}\text{Fe}_2\text{O}_{4.1}$ ferrite toroid samples sintered at 1100 °C for 2 hours including: (a) real and imaginary parts of permittivity; (b) dielectric loss tangent.

Figure 5-3 (a-d) shows the permeability and permittivity spectra of $\text{Ni}_{0.4}\text{Co}_{0.25}\text{Zn}_{0.35}\text{Fe}_2\text{O}_{4.1}$ /Epoxy composite samples loaded with different volume percentages of ferrite fillers (Pure ferrites, 33 vol%, 37 vol %, 47 vol %, 55 vol % and 66 vol %), which have been measured at 1 MHz-1 GHz using a RF impedance analyzer. The real part of permeability of magnetic epoxy composites is lower than that of pure ferrite as shown in Figure 5-3 (a). As expected, the real part of permeability increases with the increase in percentage of ferrite fillers in the composite. Magnetic loss tangent also follows the same trend and increases with the filler percentage. Real part of permittivity is almost constant over the entire frequency range up to 1 GHz. There is no resonance observed in the magnetic epoxy composite up to 1 GHz. It was known that magnetic polymer composites typically exhibit higher resonance as compared to pure ferrites as shown in Figure 5-3. Dielectric and magnetic loss tangents of magnetic epoxy composite observed is comparable to that of pure ferrite, specially over frequencies below 400 MHz. The magnetic dielectric properties of the ferrite-epoxy composite shows that these ferrites will be a good candidate for substrates utilized in applications such as biomedical implants, NFC and RFID antennas for these frequency

ranges. Table 5-1 shows the microwave properties measured at 400 MHz of a variety of Ni-Co-Zn/Epoxy magnetic composite samples loaded with ferrite fillers of different volume fractions.

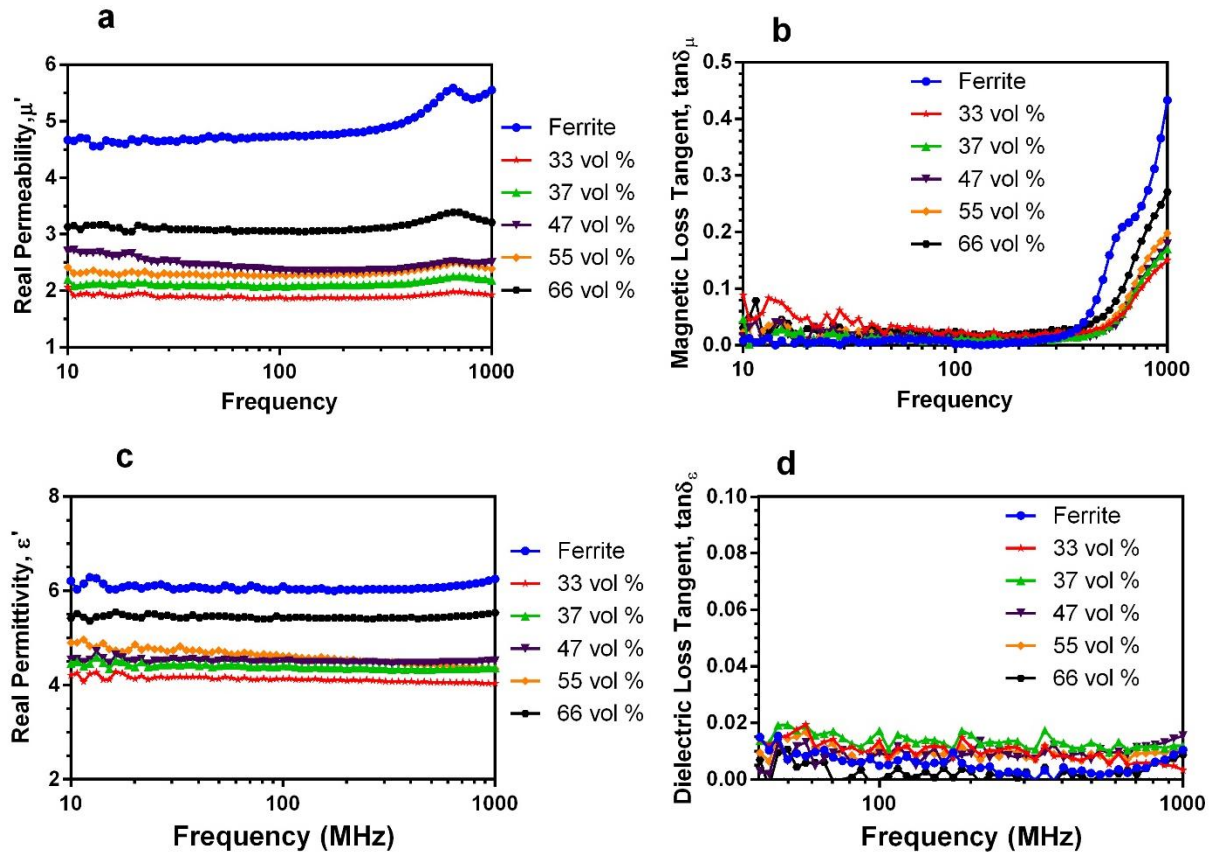


Figure 5-3 Magnetic and dielectric properties of $\text{Ni}_{0.4}\text{Co}_{0.25}\text{Zn}_{0.35}\text{Fe}_2\text{O}_{4.1}$ /Epoxy composite toroid samples including: (a) permeability; (b) magnetic loss tangent; (c) permittivity; and (d) dielectric loss tangent.

Table 5-1 Microwave properties of Ni-Co-Zn/Epoxy magnetic composite measured at 400 MHz

Volume Fraction	Permeability	Magnetic Loss	Permittivity	Dielectric Loss
0	5.0	0.01	6.1	0.003
0.33	1.90	0.02	4.16	0.005
0.37	2.14	0.03	4.34	0.005
0.47	2.50	0.02	4.47	0.005
0.55	2.40	0.02	4.51	0.005
0.66	3.2	0.03	5.40	0.006

5.3 Theoretical Models for Effective Permeability and Permittivity of Ni-Co-Zn/Epoxy Soft Magnetic Composites

In this section, different models were used to calculate and compare the effective permeability and permittivity of Ni-Co-Zn/Epoxy magnetic composites composed of different volume fractions of ferrite fillers. These models are based on the heterogeneous mixtures, in this case ferrite-medium mixtures. The main purpose of using these models is to examine the effective permeability and permittivity of ferrite particles in the epoxy medium using the measured real permeability and permittivity values at 1 MHz -1 GHz frequency range. There are a few models for ferrite-medium mixtures. In all equations mentioned below, μ_{eff} and ε_{eff} represents effective permeability and permittivity of the ferrite-medium mixture, respectively. μ_m and ε_m represents permeability and permittivity of medium, respectively. μ_i and ε_i represents intrinsic permeability and permittivity of ferrite powder, respectively, and f represents the volume fraction of the ferrite powders in the mixture.

5.3.1 Bruggeman Mixture Equation

Bruggeman mixture equation is a structure dependent mixture equation which was derived by taking care of microscopic structure of the ferrite-medium mixture. This equation is based on effective medium theory, in which both constituents are supposed to be embedded in the effective medium.

$$f \frac{\mu_i - \mu_{eff}}{\mu_i + 2\mu_{eff}} + (1 - f) \frac{\mu_m - \mu_{eff}}{\mu_m + 2\mu_{eff}} = 0 \quad (20)$$

This equation is expected to predict effective permeability and permittivity the mixture of up to 50% of ferrite particle fillers in volume fraction as reported in the literature.

5.3.2 Maxwell-Garnett Mixture Equation

Maxwell-Garnett mixture equation was also derived based on microscopic structure of the mixture. This is the oldest mixture equation used for ferrite-medium mixtures and also called as Rayleigh mixture equation 21.

$$\frac{\mu_{eff}-\mu_m}{\mu_{eff}+2\mu_m} = f \frac{\mu_i-\mu_m}{\mu_i+2\mu_m} \quad (21)$$

This equation is applicable to only spherical particles in the mixture.

5.3.3 QCA-CP Mixture Equation

QCA-CP mixture equation is also dependent on structure of the ferrite particles. This equation is also called GKM approximation 22.

$$\mu_{eff} = \mu_m + \frac{3f\mu_{eff}(\mu_i-\mu_m)}{3\mu_{eff}+(1-f)(\mu_i-\mu_m)} \quad (22)$$

5.3.4 Lichtenecker Mixture Equation

Lichtenecker mixture equation was derived based on random distribution of particles of different shapes and orientations and is applicable to both lossy and lossless materials. It is a two-part mixture equation and is symmetrical with respect to permittivities and permeabilities of the two components.

$$\frac{\mu_{eff}}{\mu_m} = \left(\frac{\mu_i}{\mu_m}\right)^f \quad (23)$$

5.3.5 Logarithm Mixture Equation

Logarithm mixture equation was also derived by Lichtenecker. This equation is a linear mixture equation based on random shapes and orientations of particles in the medium.

$$\ln \mu_{eff} = f \ln \mu_i + (1-f) \ln \mu_m \quad (24)$$

All of the above-mentioned mixture equations are used to calculate the effective permeability along with effective permittivity.

5.4 Comparison Between Measured and Calculated Effective Microwave Properties of Ni-Co-Zn/Epoxy Composite Substrate

Figure 5-4 shows the comparison between measured and calculated values of the relative permeability and permittivity. It can be observed that measured values of the relative permeability and permittivity are in good agreement with Bruggeman and QCA-CP mixture equations. This shows that both Bruggeman model and QCA-CP mixture equations accurately predict the electromagnetic properties of this ferrite/epoxy composite mixture. On the contrary, experiment values are slightly lower as compared to values calculated by Maxwell-Garnett, Lichtenecker and Logarithm mixture equations. It is observed that both real permeability and permittivity values are strongly volume fraction dependent in case of Maxwell-Garnett mixture equation, but it is seen that this equation did not give accurate electromagnetic properties over a wide volume fraction range. Also, variation in permeability and permittivity in case of Lichtenecker and Logarithm mixture equations can be attributed to the fact that both these equations were derived based on random shapes and orientation. It is also observed from the results that measured values of both permeability and permittivity are slightly higher for ferrite particle loadings above 50 vol.% as compared to calculated values. This can be attributed to the fact that there are more large particle clusters formed at higher ferrite particle loadings which leads to higher value of permeability and permittivity. This size increase due to cluster formation is not accounted for in various models.

Figure 5-5 shows the comparison between measured and calculated values of real permeability versus frequency for different volume fractions: 0.33, 0.47 and 0.66. Figure 5-6 shows the comparison between measured and calculated values of relative permittivity versus frequency for different volume fractions: 0.33, 0.47 and 0.66. Table 5-2 shows the permeability

and permittivity values for all the volume fractions calculated using above-described mixture equations.

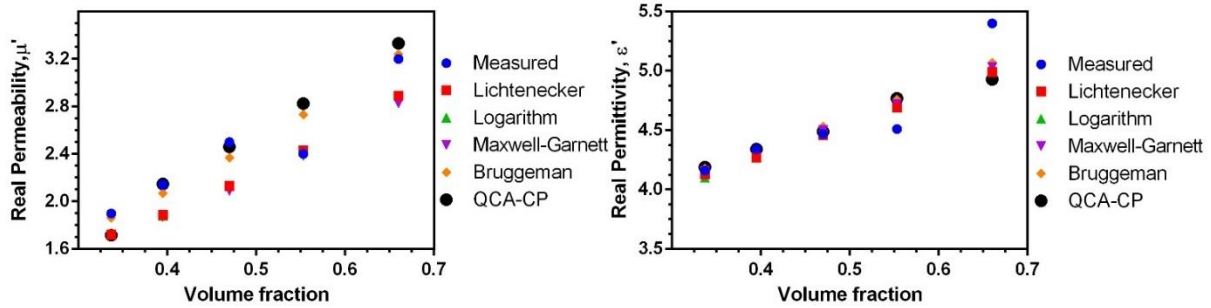


Figure 5-4 Real permeability and permittivity of $\text{Ni}_{0.4}\text{Co}_{0.25}\text{Zn}_{0.35}\text{Fe}_2\text{O}_{4.1}$ /Epoxy magnetic composites using different mixture models versus volume fraction at 400 MHz: (a) real permeability; (b) real permittivity

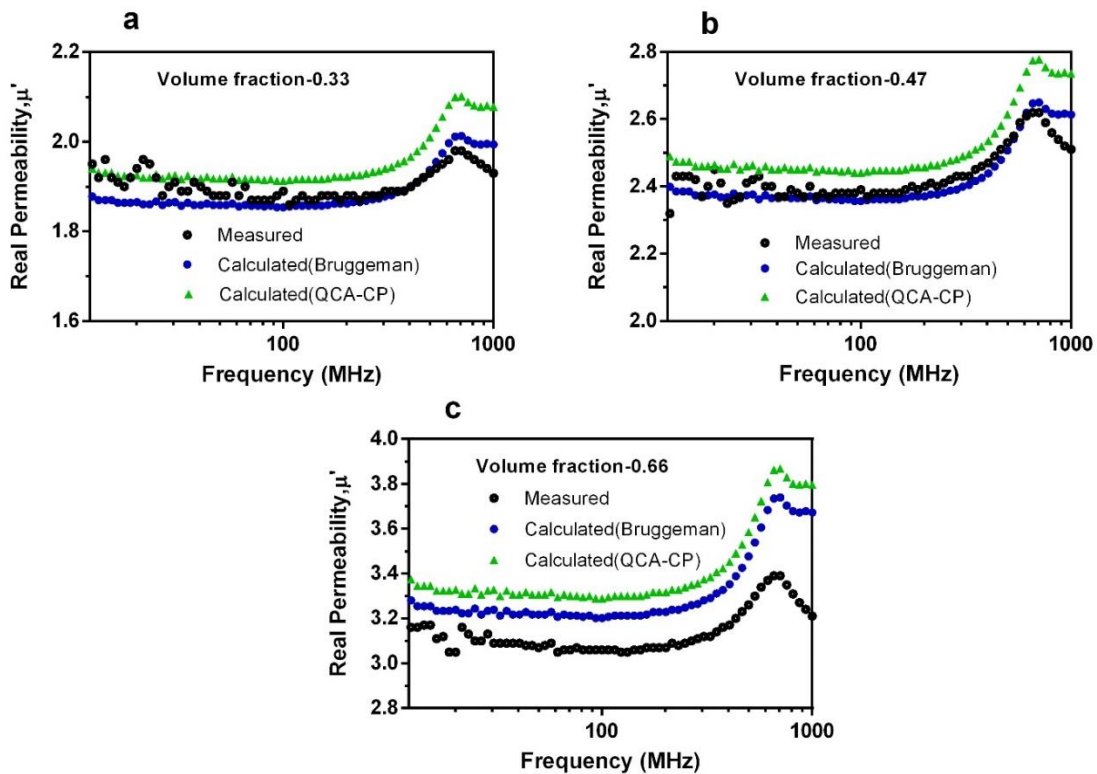


Figure 5-5 Comparison between measured and calculated values of real permeability versus frequency for different volume fractions: (a) 0.33; (b) 0.47; (c) 0.66.

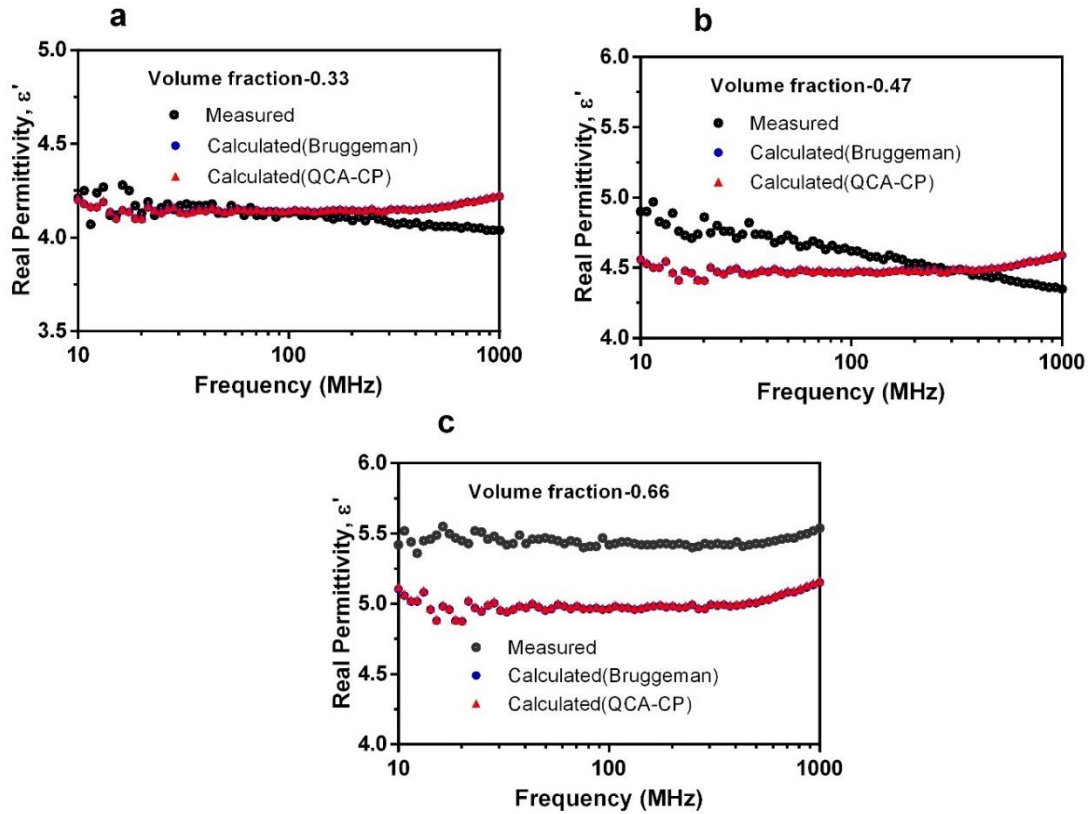


Figure 5-6 Comparison between measured and calculated values of real permittivity versus frequency for different volume fractions: (a) 0.33; (b) 0.47; (c) 0.66.

Table 5-2 Measured vs. model predicted properties of Ni-Co-Zn/Epoxy magnetic composites

Composite Sample	Permeability (μ')	Permittivity (ϵ')
Volume Fraction- 0.33 @ 400 MHz		
Measured values	1.9	4.16
Bruggeman mixture equation	1.86	4.18
Maxwell-Garnett mixture equation	1.72	4.16
QCA-CP mixture equation	1.75	4.19
Lichtenecker mixture equation	1.72	4.10
Logarithm mixture equation	1.72	4.13
Volume Fraction- 0.37 @ 400 MHz		
Measured values	2.14	4.34
Bruggeman mixture equation	2.07	4.33

Table 5-2 (Continued)

Maxwell-Garnett mixture equation	1.87	4.3
QCA-CP mixture equation	2.14	4.34
Lichtenecker mixture equation	1.88	4.27
Logarithm mixture equation	1.88	4.27
Volume Fraction- 0.47 @ 400 MHz		
Measured values	2.5	4.47
Bruggeman mixture equation	2.37	4.53
Maxwell-Garnett mixture equation	2.09	4.5
QCA-CP mixture equation	2.46	4.49
Lichtenecker mixture equation	2.13	4.46
Logarithm mixture equation	2.13	4.46
Volume Fraction- 0.55 @ 400 MHz		
Measured values	2.42	4.51
Bruggeman mixture equation	2.73	4.75
Maxwell-Garnett mixture equation	2.38	4.72
QCA-CP mixture equation	2.82	4.77
Lichtenecker mixture equation	2.43	4.69
Logarithm mixture equation	2.43	4.69
Volume Fraction- 0.66 @ 400 MHz		
Measured values	3.2	5.4
Bruggeman mixture equation	3.24	5.07
Maxwell-Garnett mixture equation	2.82	5.03
QCA-CP mixture equation	3.33	4.94
Lichtenecker mixture equation	2.89	4.99
Logarithm mixture equation	2.89	4.99

5.5 Design, Fabrication and Characterization of Microstrip Patch Antennas for Ultra High Frequency Band (MICS Band)

In this section, performance and miniaturization capabilities of microstrip patch antenna using dielectric and magnetic-dielectric substrates have been studied for the 401-406 MHz frequency range. For the fabrication of two microstrip patch antennas for this comparison study, a dielectric substrate (dielectric core of a Rogers RO3010 commercial laminate with a permittivity of 10.2 and loss tangent of 0.003) and a synthesized magnetic composite substrate with measured permittivity of 4.4, permeability of 2.4, magnetic loss tangent of 0.03 and dielectric loss tangents of 0.006 are employed. Additionally, the effects of substrate thickness and material properties on the performance of antenna built on top of dielectric and ferrite composite substrates were studied.

5.5.1 Parametric Analysis for the Design of the Patch Antennas

During the antenna design process, dimensions of the antenna patch were calculated according to the equations reported by Balanis, Schneider's, Paucel and Masse.

The resonance frequency of the rectangular microstrip patch antenna is calculated by following equation 25

$$f_r = \frac{c}{2L\sqrt{\epsilon_{eff}\mu_{eff}}} \quad (25)$$

where c is speed of light, L is length of patch, ϵ_{eff} is effective permittivity, and μ_{eff} is effective permeability.

Over the UHF frequency range, permittivity is considered nondispersive. Hence, it can be calculated using Schneider's equation 26

$$\epsilon_{eff} = 0.5\left[\epsilon_r + 1 + \frac{(\epsilon_r - 1)}{\left(1 + 10\frac{h}{w}\right)^2}\right] \quad (26)$$

where h is substrate thickness, ϵ_r is relative permittivity at MHz frequencies, w is width of patch antenna.

μ_{eff} can be calculated using the formula given by Pucel and Masse

$$\mu_{eff} \approx \mu_r \left(\frac{C}{C-D}\right)^2 \dots\dots \text{for } \frac{w}{h} \geq 2 \quad (27)$$

$$\mu_{eff} \approx \frac{2\mu_r}{1+\mu_r} \left(\frac{A-B}{A}\right)^2 \dots\dots \text{for } \frac{w}{h} \leq 2 \quad (28)$$

$$C = \frac{w}{2h} + \frac{(\ln 2\pi \epsilon \left[\frac{w}{2h} + 0.94\right])}{\pi} \quad (29)$$

$$D = (1 - \mu_r) \frac{(\ln[0.5\pi \epsilon \left(\frac{w}{2h} + 0.94\right)] - \mu_r \ln\left[\frac{\pi^2 \epsilon}{16}\right])}{2\pi} \quad (30)$$

$$A = \ln\left(\frac{8h}{w}\right) + 0.5 \left(\frac{w}{4h}\right)^2 \quad (31)$$

$$B = 0.5 \left(\frac{1-\mu_r}{1+\mu_r}\right) \left\{ \ln\left(\frac{\pi}{2}\right) + \mu_r \ln\left(\frac{4}{\pi}\right) \right\} \quad (32)$$

where, μ_r is the real part of the absolute permeability of the substrate.

The patch width of the antenna for a good radiation efficiency is given by equation 33

$$w = \frac{c}{2f_r \sqrt{\frac{(\epsilon_{eff}+1)(\mu_{eff}+1)}{2}}} \quad (33)$$

The effective patch length is given by following equation 34

$$L_{eff} = \frac{1}{2f_r \sqrt{\mu_{eff} \epsilon_{eff} \sqrt{\mu_0 \epsilon_0}}} \quad (34)$$

where,

$$L = L_{eff} - 2\Delta L \quad (35)$$

The normalized antenna length extension can be calculated using equation 36

$$\frac{\Delta L}{h} = 0.412 \frac{(\epsilon_{eff}+0.3)\left(\frac{w}{h}+0.264\right)}{(\epsilon_{eff}-0.258)\left(\frac{w}{h}+0.8\right)} \quad (36)$$

5.5.1.1 Figure of Merit and Measurement Techniques

To analyze the performance of dielectric and magnetic composite patch antennas, return loss (S_{11}), resonance frequency (f_r), -10 dB bandwidth (BW), Gain (dBi) and radiation pattern parameters have been used. The performance of the patch antenna was simulated using ANSYS Electromagnetic Suite (HFSS 19). For return loss measurements, a 50 MHz-6 GHz vector network analyzer (VNA) was used measure frequency characteristics between 350 MHz and 550 MHz. 2D radiation pattern measurements were done by using USF WAMI Center's anechoic chamber.

5.5.2 Simulations and Design of Microstrip Patch Antenna Using Dielectric and Magnetic Composite Substrates

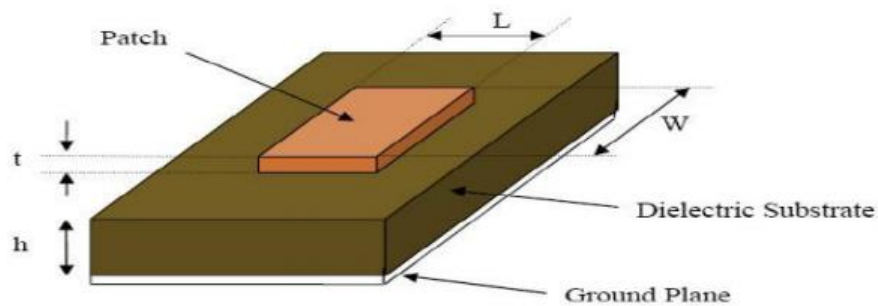


Figure 5-7 Schematic illustration of the key design parameters of a microstrip patch antenna.

For the patch antenna design and simulation, measured dielectric and magnetic composite substrate properties as a function of frequency were added in the ANSYS/HFSS 3D EM simulation software. All the dimensions of patch antennas for both dielectric and magnetic composite substrates were calculated according to aforementioned antenna equations. The dimensions of patch antenna were optimized in the design according to desired resonance frequency. Figure 5-7 shows the schematic diagram of patch antenna design. Table 5-3 shows the dimensions of patch antennas for dielectric and magnetic substrates. The dielectric and magnetic composite substrate were selected according to the values of permittivity and permeability. Antenna performances are

compared using figure of merit such as bandwidth, return loss, gain and size of the patch. Table 5-4 shows the microwave properties of the different substrate used for comparison.

Table 5-3 Patch antenna design parameters for devices over different substrates

Substrate	Patch Length (mm)	Patch Width (mm)	Substrate Height (mm)
Antenna 1: Rogers (RO3006)	146	190	2
Antenna 2: Rogers (RO3010)	111	135	1.27
Antenna 3: NiCoZn/Epoxy	112	115	2

Table 5-4 Antenna substrate properties

Substrate Properties	Permittivity (ϵ)	Dielectric Loss Tangent ($\tan\delta_\epsilon$)	Permeability (μ)	Magnetic Loss Tangent ($\tan\delta_\mu$)
Antenna 1: Rogers (RO3006)	6.15	0.0025	1	0
Antenna 2: Rogers (RO3010)	10.2	0.003	1	0
Antenna 3: NiCoZn/Epoxy	4.4	0.006	2.4	0.03

The representation schematic and electric field distribution of the patch antenna are shown in Figure 5-8 and 5-9, respectively. During the simulation of dielectric and magnetic patch antennas, 35 μm thick metallic layer of Cu was used for both patch and ground layers. Dielectric and magnetic layers of substrate were used between the patch and ground for dielectric and magnetic composite antenna, respectively. In order to compare the performance of the dielectric and magnetic composite antennas, antenna designs 1 and 3 are compared to show the miniaturization of patch with comparable permittivity values. Antenna design 2 and 3 are

compared to show the enhancement in the patch antenna bandwidth. Figure 5-10 shows the return loss (dB) versus frequency comparison for all three antennas. Clear differences are observed in terms of bandwidth enhancement between antenna design 1, 2 and 3. Four times enhancement in antenna bandwidth has been achieved for magnetic composite antenna (permittivity-4.4) when it is compared to a reference design implemented using pure dielectric substrate (e.g. dielectric core of the RO3006 laminate with a permittivity of 6.15). Similarly, two times enhancement as compared to another reference patch antenna implemented using the dielectric core of a RO3010 laminate with a permittivity of 10.2. Table 5-5 shows the antenna performance for patch antenna design 1, 2 and 3. Figure 5-11 and 5-12 depicts the radiation patterns of all three antennas over E-Plane and H-Plane.

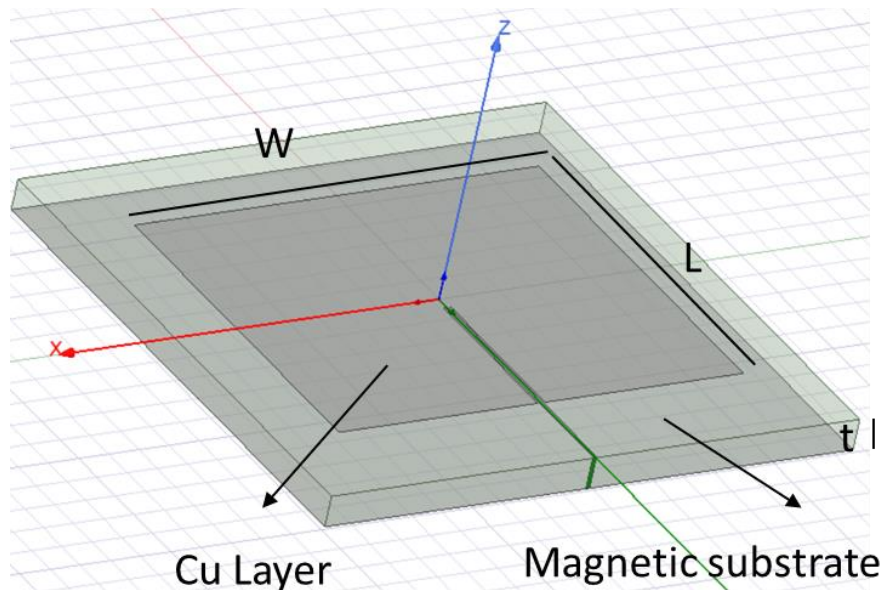


Figure 5-8 Schematic diagram of the microstrip patch antenna.

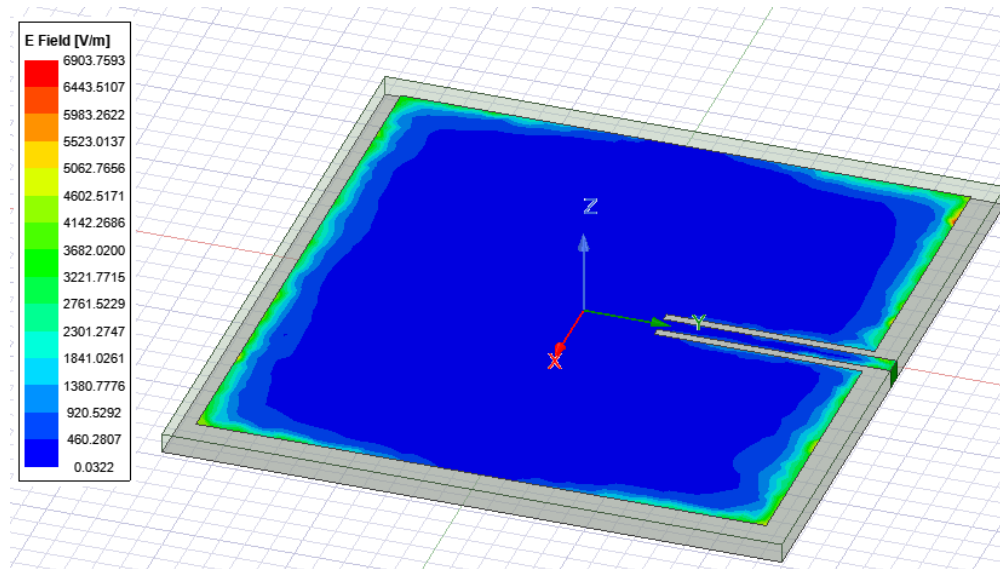


Figure 5-9 Representative electric field distribution of the microstrip patch antenna.

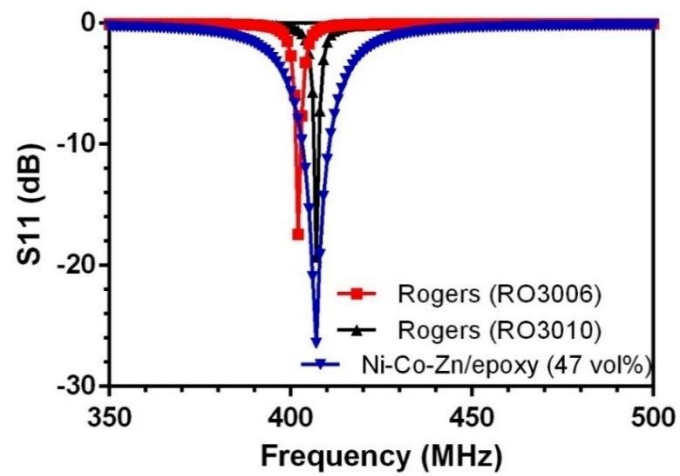


Figure 5-10 Simulated return loss vs. frequency for designed dielectric and magnetic patch antennas.

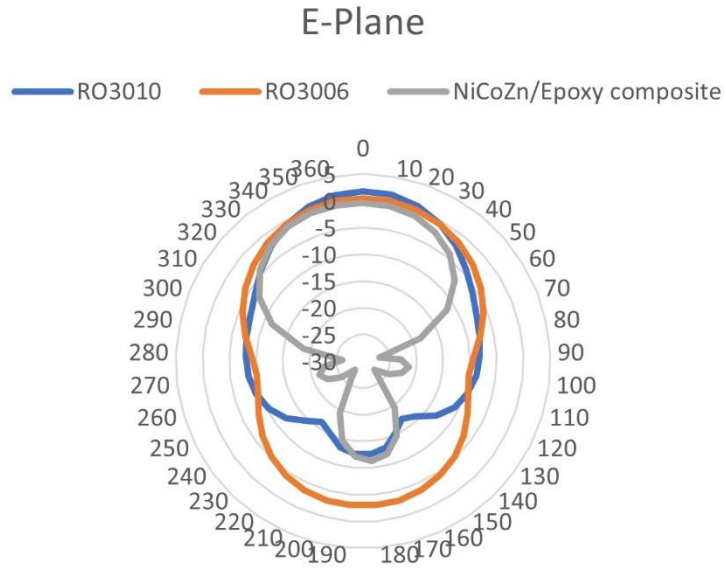


Figure 5-11 Simulated E-Plane radiation patterns for patch antenna design 1, 2 and 3.

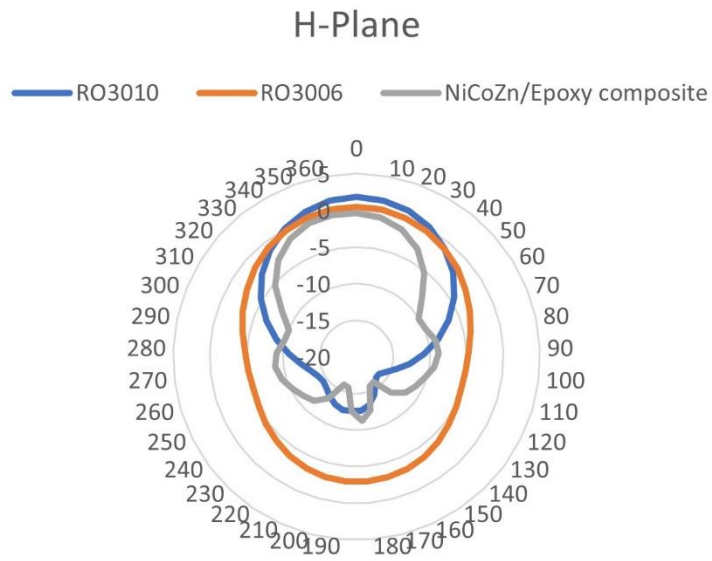


Figure 5-12 Simulated H-Plane radiation patterns for patch antenna design 1, 2 and 3.

Table 5-5 Performance parameters for antennas designed based on dielectric core of a Rogers RO3006 laminate, dielectric core of a Rogers RO3010 laminate, and Ni-Co-Zn/Epoxy substrate

Antenna	Resonance Frequency (MHz)	Return Loss (dB)	-10 dB Bandwidth (BW)	Gain (dBi)	Area (cm²)	Efficiency (%)
Antenna 1: Rogers (RO3006)	403	-17.23	2.3	2.71	277	41
Antenna 2: Rogers (RO3010)	407	-19.41	4	4.60	149	29
Antenna 3: NiCoZn/Epoxy	406	-27.01	8.2	1.85	127	14

5.5.3 Fabrication and Measurement of Microstrip Patch Antenna Using the Dielectric Core of RO3010 Laminate and Magnetic Composite (Ni-Co-Zn/Epoxy-47 Vol%) Substrate

For the fabrication of a patch antenna over a dielectric substrate, the dielectric core of a Rogers RO3010 laminate with a thickness of 1.27 mm was used as its substrate. Copper cladding sheet of a 35 μm thickness was used to form the metallic patterns (Patch, Ground, Microstrip feed) over both dielectric and magnetic composite substrates. Patch antenna was milled over a Rogers RO3010 laminate according to the optimized dimensions designed using HFSS simulations. Figure 5-13 shows the picture of the dielectric patch antenna designed on RO3010 substrate with a permittivity of 10.2 and a dielectric loss tangent of 0.003.



Figure 5-13 Micrograph of a dielectric patch antenna designed and milled using Rogers RO3010 laminate as the substrate.

For the fabrication of prototype magnetic composite patch antenna, the first step was to develop magnetic composite substrate. For this purpose, a $150 \times 150 \text{ mm}^2$ Teflon mold was used for molding of Ni-Co-Zn ferrite/epoxy slurry to form a soft magnetic substrate. Teflon cover was used with screws to get a 2 mm-thick substrate of a uniform thickness. Detailed process for the fabrication of magnetic substrate was discussed in chapter 2 under material and synthesis section. A $35 \text{ }\mu\text{m}$ thick copper sheet was used as metallic layer for both the antenna patch and ground. The copper sheet was attached using adhesive tape. For the patch antenna design, the copper sheet was cut according to dimensions of the patch design and then attached to the substrate. Figure 5-14 and 5-15 shows the picture of prototype magnetic composite patch antenna and picture of 2D antenna radiation pattern measurement setup in the USF WAMI Center's anechoic chamber, respectively.

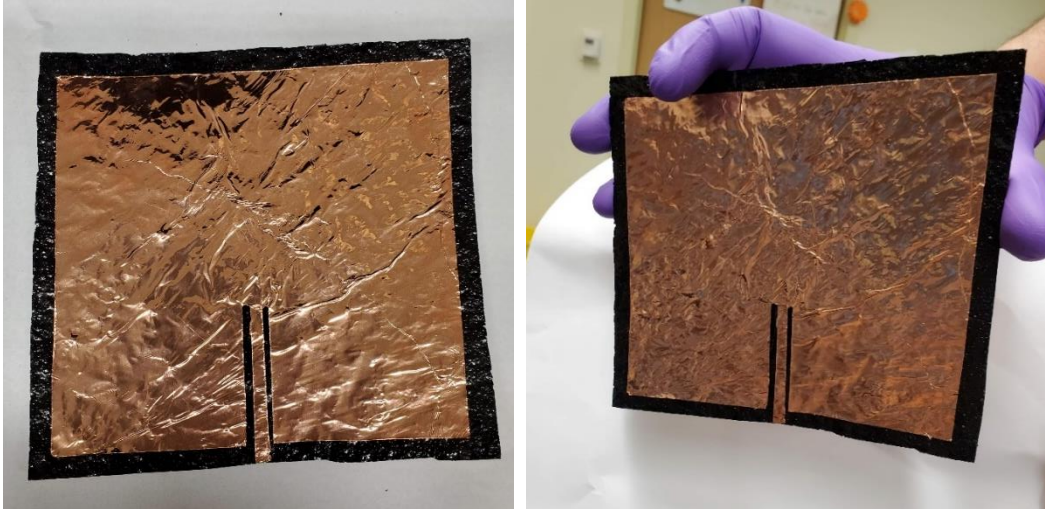


Figure 5-14 Micrograph of the magnetic patch antenna using Ni-Co-Zn/Epoxy as the substrate.

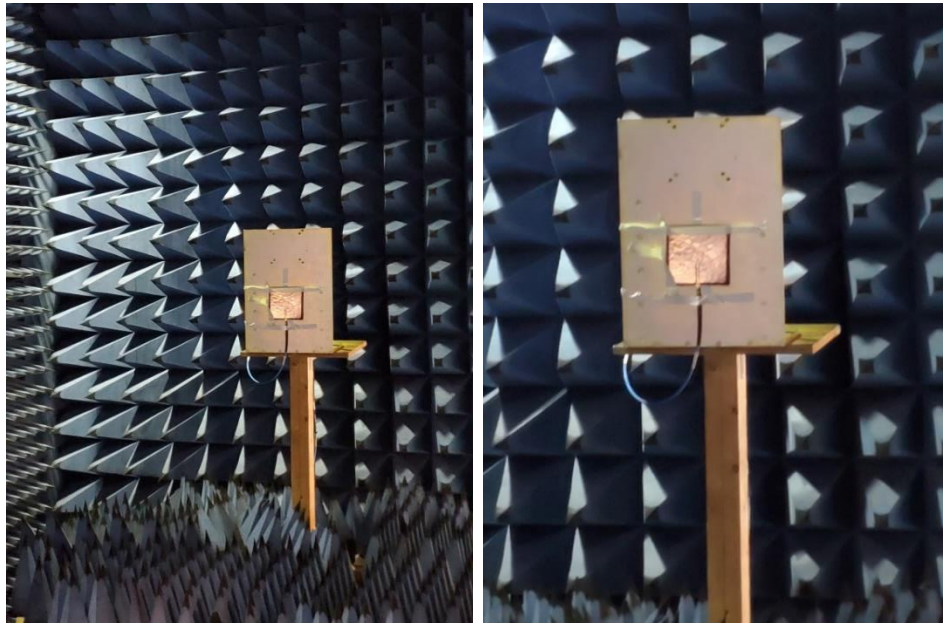


Figure 5-15 Micrograph of measurement set up for radiation pattern measurement of antenna.

5.5.3.1 Dielectric Substrate (Rogers RO3010) Patch Antenna Results

Return loss and radiation pattern of the patch antenna fabricated over a Rogers RO3010 dielectric substrate was measured using a 50 MHz-6 GHz VNA and an anechoic antenna test chamber, respectively. Simulated and measured return loss for dielectric substrate patch antenna is shown in Figure 5-16. It can be observed from Figure 5-16 that measured resonance frequency

(measured-406 MHz vs. simulated-405 MHz) and return loss (measured-13.65 dB, simulated-19.41dB) is slightly off as compared to simulated results. The small frequency shift can be ascribed to effect of the SMA connectors and geometrical discrepancy between HFSS simulated design and the actual device due to fabrication tolerance. The difference in measured and simulated return loss values can be attributed to glue used while attaching copper foil to the substrate, which in turn reduces the return loss. Figure 5-17 (a) shows the comparison between simulated E-plane and H-plane radiation patterns and Figure 5-17 (b) shows the comparison between simulated and measured E-plane radiation patterns. The parameters of the patch antenna performance are tabulated in Table 5-6.

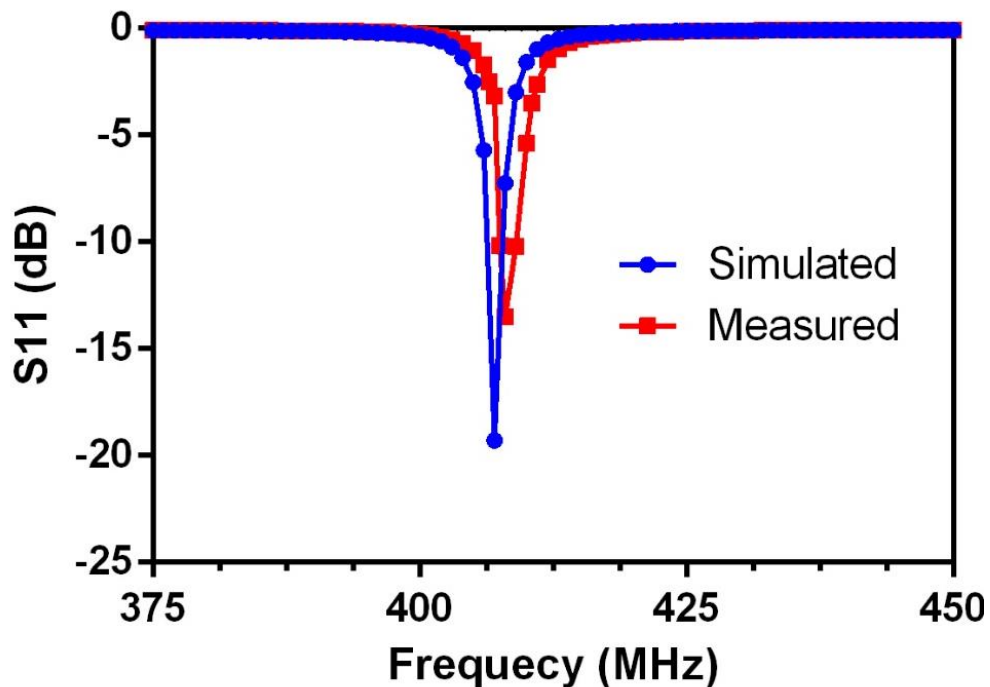


Figure 5-16 Simulated and measured return loss of custom-designed dielectric substrate patch antenna.

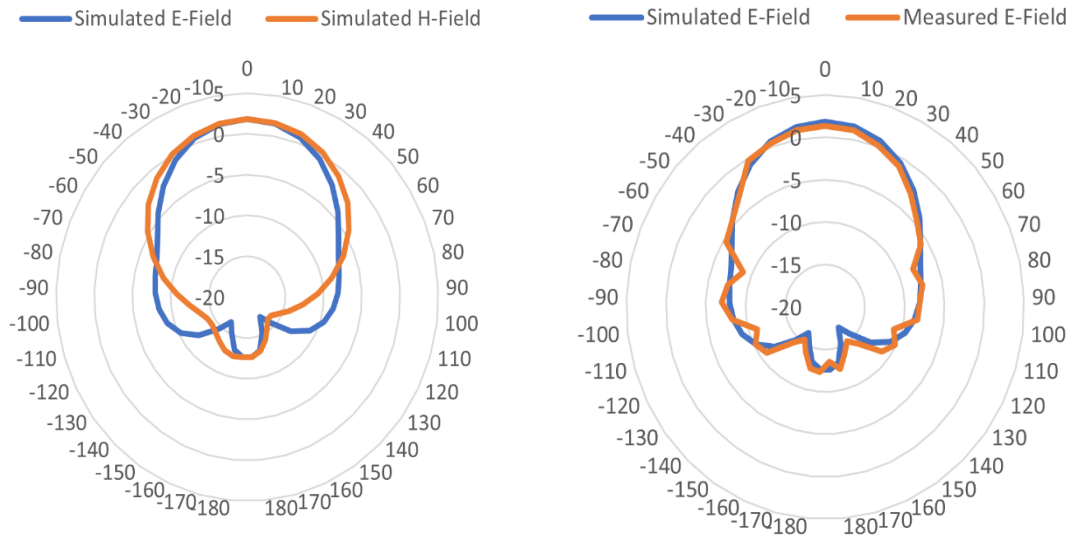


Figure 5-17 (a) Comparison between simulated E-plane and H-plane radiation patterns and (b) comparison between simulated and measured E-plane radiation patterns for dielectric substrate patch antenna.

Table 5-6 Performance parameters of dielectric (RO3010) antenna

Dielectric Antenna	Resonance Frequency (MHz)	Return Loss (dB)	Gain (dBi)	Bandwidth (MHz)
Simulated	405	-19.41	4.6	2
Measured	406	-13.65	4.32	2.1

5.5.3.2 Magnetic Composite Substrate (Ni-Co-Zn/Epoxy) Patch Antenna Results

Simulated and measured return loss for magnetic composite substrate (Permittivity-4.4, Permeability-2.4, 47 vol % loading of ferrite particles) antenna are shown in Figure 5-18. It can be seen from Figure 5-18 that measured resonance frequency (measured-405.5 MHz vs. simulated-406 MHz) and return loss (measured-23.09 dB vs. simulated-27.01dB) are comparable to simulated results. The measured 10-dB bandwidth of the antenna is 15 MHz as compared to simulated results of 8 MHz. This may be because of small air voids trapped inside the magnetic substrate during curing. This process in turn changes the microwave properties of the substrate.

The bandwidth increase is partially associated with more loss in the material. In this case, small air voids in the substrate increase the losses in the substrate, which leads to increases in the bandwidth of the antenna. Figure 5-19 shows the comparison between E-plane and H-plane radiation patterns as well as the comparison between simulated and measured E-plane radiation patterns. The measured gain of fabricated magnetic substrate patch antenna is 1.51 dBi, while simulated gain is 1.8 dBi. Simulated and measured parameters of antenna performance are tabulated in Table 5-7.

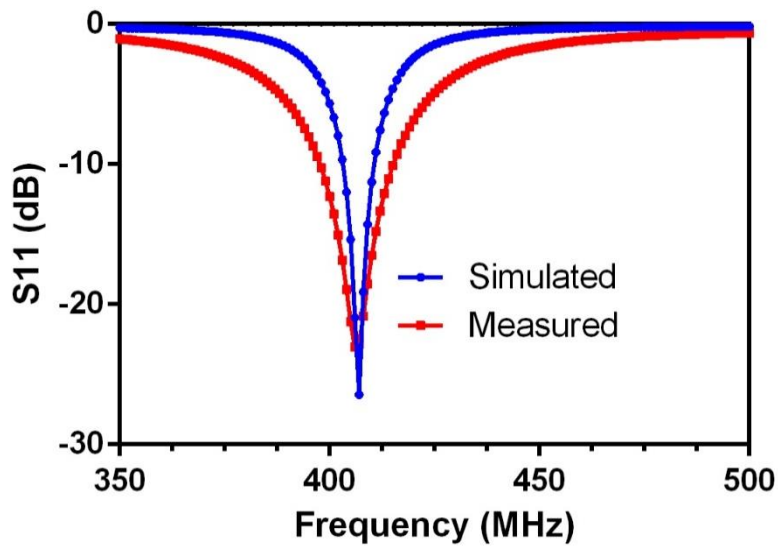


Figure 5-18 Simulated and measured return loss of Ni-Co-Zn/Epoxy patch antenna.

Table 5-7 Performance parameters of magnetic composite (vol 47 %) antenna

Dielectric Antenna	Resonance Frequency (MHz)	Return Loss (dB)	Gain (dBi)	Bandwidth (MHz)
Simulated	406	-27.01	1.8	8
Measured	405.5	-23.09	1.59	15

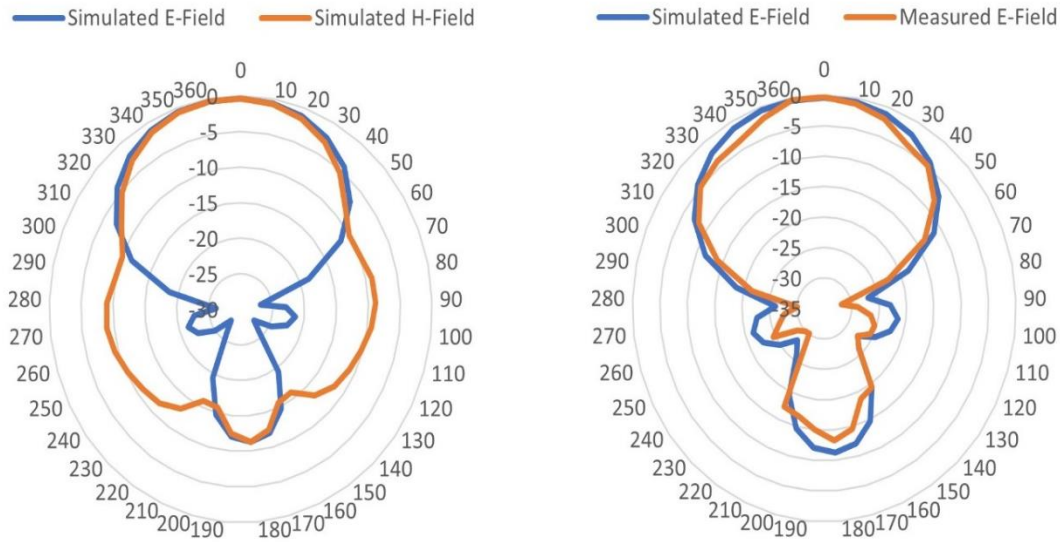


Figure 5-19 (a) Comparison between simulated E-plane and H-plane radiation patterns; and (b) comparison between simulated and measured E-plane radiation patterns.

5.5.3.3 Comparison in Performance between Dielectric Substrate (Rogers RO3010) and Magnetic Composite Substrate (Vol 47 %) Antennas

Measured return losses for dielectric substrate (Rogers RO3010) and magnetic composite substrate (ferrite loading 47 vol %) patch antennas are shown in Figure 5-20. Dielectric substrate patch antenna was designed on a Rogers RO3010 substrate with a permittivity of 10.2, and magnetic composite substrate patch antenna was designed on substrate with permittivity of 4.4 and permeability of 2.4. The miniaturization factor of the substrate is calculated by equation: $\eta = \sqrt{\epsilon \times \mu}$. For dielectric substrate η is 3.2; while for magnetic composite substrate η is 3.24. Also, both antennas are designed for same frequency, so direct comparison can be done in antenna performances. As seen in Figure 5-20, magnetic composite antenna presents 7.5 times higher bandwidth than that of the dielectric substrate antenna fabricated on Rogers RO3010 substrate. Measured return loss is also higher for magnetic composite substrate patch antenna. Antenna designed on magnetic substrate offers smaller antenna patch size as compared to that of the

dielectric substrate patch antenna. Magnetic composite patch antenna is 17.5% smaller in size than that of the dielectric substrate patch antenna. Gain of dielectric substrate patch antenna is 4.32 dBi, which is higher than the gain of the magnetic composite substrate antenna of 1.59 dBi. This can be attributed to the fact that magnetic and dielectric losses are higher in soft magnetic composite substrate (Magnetic loss-0.003, Dielectric loss-0.006) as compared to the losses of the dielectric substrate (Magnetic loss-0.00, Dielectric loss-0.002). Higher antenna gain can be achieved by decreasing the losses of the substrate. All the performance parameters are presented in Table 5-8.

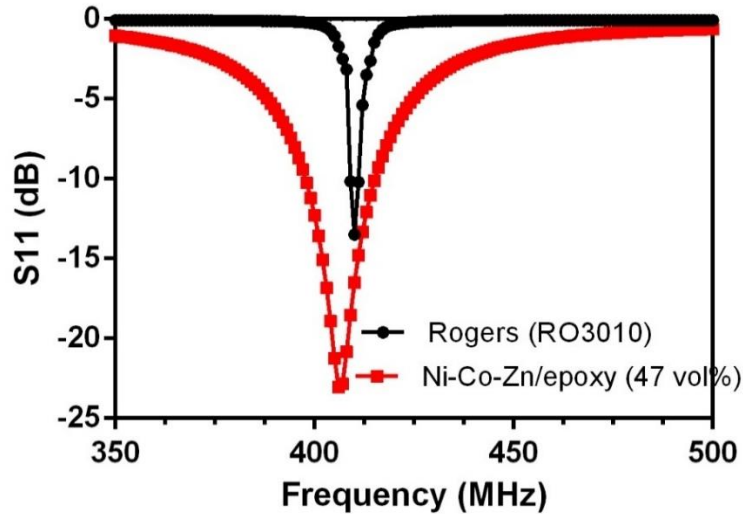


Figure 5-20 Measured return loss for dielectric substrate (RO3010) and magnetic composite substrate (Ni-Co-Zn/Epoxy) patch antennas.

Table 5-8 Measured parameters of dielectric substrate and magnetic composite patch antennas

Antenna (Measured)	Resonance Frequency (MHz)	Return Loss (dB)	Gain (dBi)	Bandwidth (MHz)	Area (cm ²)
Dielectric (RO3010)	406	-13.65	4.32	2.1	149
Magnetic Composite (47 vol %)	405.5	-23.09	1.59	15	127

5.5.4 Effects of Substrate Thickness and Material Properties on the Performance of Dielectric Substrate and Magnetic Composite Substrate Patch Antennas

In this section, after the evaluation of the performance of simulated and measured prototype dielectric substrate (Rogers RO3010) and magnetic composite (Ni-Co-Zn/Epoxy-47 vol % ferrite loading) patch antennas, the effects of substrate thickness and material properties on the performance of designed patch antennas was studied using HFSS simulations. We know that the microwave properties of the substrate and thickness of the substrate have direct effects on the performance of the antennas such as gain, bandwidth, return loss, efficiency and size of the antenna patch. Low permittivity and thick substrates can result in better patch antenna gain and efficiency, at the expense of antenna size. On the contrary, high permittivity substrate helps in reduction of patch antenna size at the expense of bandwidth and return loss. In this section, we studied the effect of the substrate thickness (1.27 mm - 10 mm) on dielectric substrate and magnetic composite antenna performance. The effect of ferrite volume loading for magnetic composite substrate patch antenna is also studied using HFSS simulations.

5.5.4.1 Dielectric Substrate (RO3010) Antenna Performance with Varied Substrate Thickness

Figure 5-21 shows the effect of substrate thickness on the return loss, gain and efficiency of the dielectric substrate antenna. It can be observed that as thickness of the substrate increases, resonance frequency has shifted from 406 MHz to 415 MHz with low return loss. On the contrary, there is a positive effect on the gain and efficiency of the patch antenna due to increment of the substrate thickness. All the performance parameters are tabulated in Table 5-9 for designs with varied thickness. It is noted that after a thickness of 6 mm, gain and efficiency started to decrease. Therefore, we did not increase the thickness above 6.5 mm for the 3D EM simulations. An

optimized return loss curve at resonance frequency of 407 MHz is plotted in Figure 5-22 for a thickness of 6 mm and tuned patch parameters. Table 5-10 shows the new optimized properties of the 6mm-thick dielectric substrate patch antenna.

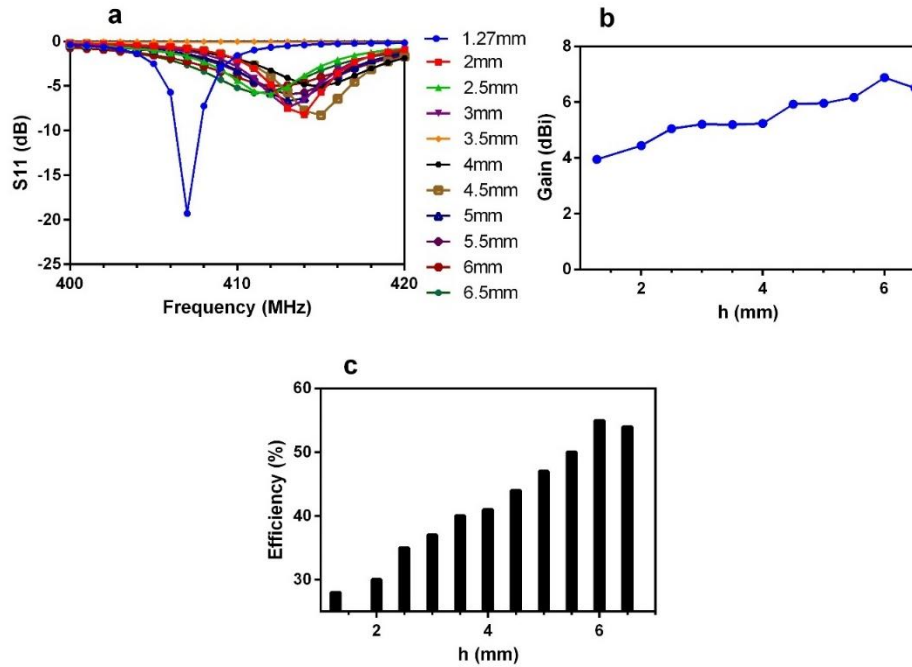


Figure 5-21 Stimulated performance parameters including: (a) return loss; (b) gain and (c) efficiency of the dielectric substrate (RO3010) patch antenna at varied thickness.

Table 5-9 Performance parameters for dielectric substrate patch antennas of varied thickness

Substrate Thickness (mm)	Return Loss (dB)	Gain (dBi)	Resonance Frequency (MHz)	Efficiency (%)
1.27	-19.3	3.95	407	28
2	-8.2	4.44	414	30
2.5	-6	5.05	412	35
3	-7.5	5.21	413	37
3.5	-6.6	5.20	414	40
4	-5	5.24	415	41
4.5	-8.2	5.93	415	44
5	-6.69	5.98	413	47
5.5	-5.94	6.18	413	50
6	-4.99	6.88	413	55
6.5	-5.77	6.51	411	54

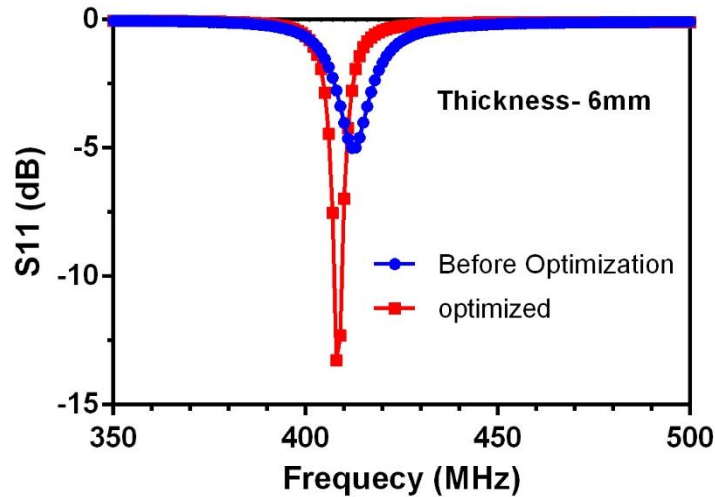


Figure 5-22 Simulated return losses for dielectric substrate (RO3010) before and after optimization of parameters.

Table 5-10 Optimized performance parameters for 6 mm-thick dielectric substrate patch antennas

Substrate Thickness (h= 6mm)	Resonance Frequency (MHz)	Return Loss (dB)	Gain (dBi)	Efficiency (%)
Non-optimized	413	-4.99	6.88	55
Optimized	407	-13.28	6.73	56

5.5.4.2 Magnetic Antenna Performance with Varying Substrate Thickness

Figure 5-23 shows simulation results for the effect of substrate thickness ($h=1.27$ mm - 10 mm) on the return loss, gain and efficiency of the magnetic composite Ni-Co-Zn/epoxy patch antenna. As observed from the figure, the resonance frequency has shifted from 405 MHz to 454 MHz due to the thickness increment from 1.27 mm to 10 mm. Gain and efficiency have shown dramatic increase in values with the thickness increase. It is already known that the substrate thickness has positive effect on the antenna performance. In order to optimize the design for the resonance frequency of 407 MHz, the antenna patch dimensions have been adjusted.

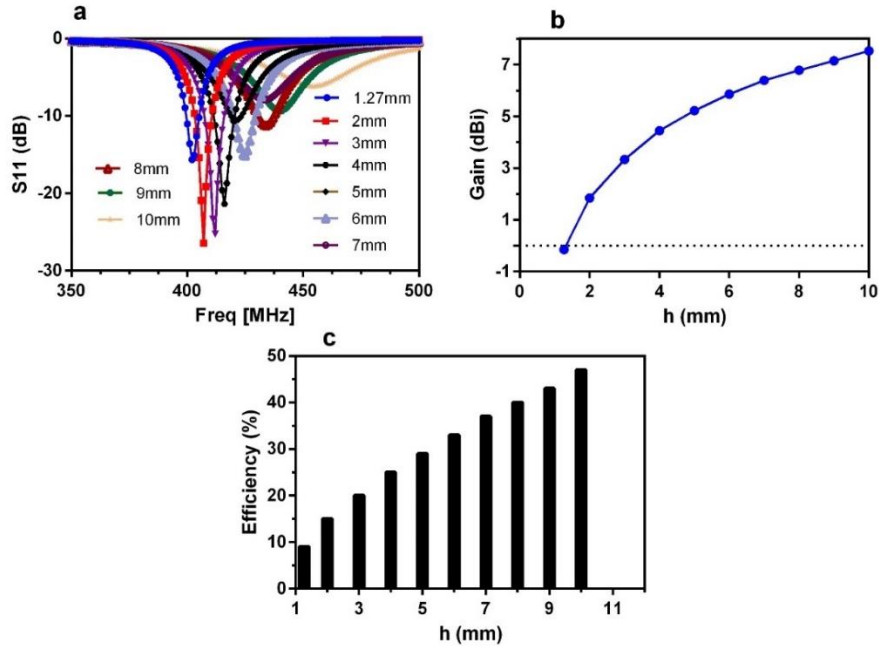


Figure 5-23 Stimulated performance parameters including: (a) return loss; (b) gain and (c) efficiency of the magnetic composite Ni-Co-Zn/Epoxy patch antenna at varied thickness.

During the optimization process, both gain and efficiency are not affected very much. Hence, based on the application requirement, high gain performance antenna can be designed on thick magnetic substrate by not compromising the antenna bandwidth. All performance parameters are depicted in Table 5-11.

Table 5-11 Performance parameters of magnetic composite antenna of varied thickness

Substrate Thickness (mm)	Return Loss (dB)	Gain (dBi)	Resonance Frequency (MHz)	Efficiency (%)
1.27	-15.63	-0.15	402	9
2	-27.01	1.85	406	15
3	-25.25	3.33	412	20
4	-21.39	4.45	416	25
5	-10.55	5.22	421	29
6	-15.13	5.86	425	33
7	-7.92	6.39	433	37
8	-11.2	6.78	434	40
9	-9.35	7.15	440	43
10	-6.18	7.53	454	47

5.5.4.3 Effect of Ferrite Volume Loading on Performance of Magnetic Composite Antennas

Based on the measured values of permeability, permittivity, magnetic and dielectric losses for different ferrite volume loadings, simulations were performed for three different ferrite volume loadings of 33%, 47% and 66%. Figure 5-24 shows the return loss, gain, bandwidth, and antenna size reduction with respect to the Ni-Co-Zn ferrite loading. It can be observed that gain is decreased with ferrite loading, which can be observed by the fact that both magnetic and dielectric losses increase with ferrite particle loadings. Similar effect on antenna bandwidth can be observed, it increases with ferrite loading. Because of high values of permeability and permittivity, antenna size decreases with ferrite loading. All performance parameters with Ni-Co-Zn ferrite volume loading are depicted in Table 5-12. Table 5-13 shows the reported antenna performance for different magnetic composites (prior works in literatures) and Ni-Co-Zn/epoxy composite (the present work).

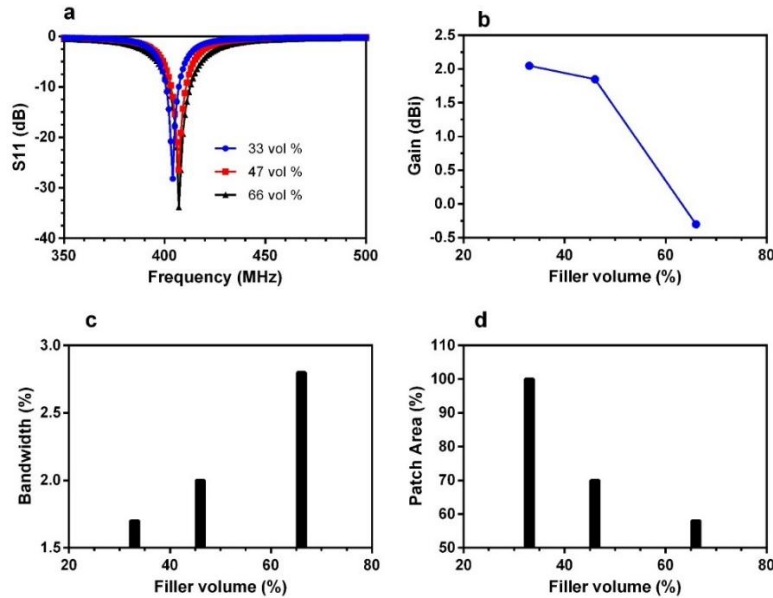


Figure 5-24 Stimulated performance parameters including: (a) return loss; (b) gain; (c) bandwidth and (d) patch area of the magnetic composite Ni-Co-Zn/Epoxy patch antenna at different ferrite volume loading.

Table 5-12 Performance parameters of magnetic composite antenna with different Ni-Co-Zn ferrite particle loading volume fractions

Ferrite Volume Loading (Vol %)	Return Loss (dB)	Gain (dBi)	Bandwidth (MHz)	Patch Area (cm²)	Efficiency (%)
33	-28.17	2.05	7	179	25
47	-27.01	1.85	8	127	15
66	-33	-0.3	11	104	10

Table 5-13 Summary of prior works reported in literatures and the present work for the magnetic composite antenna performance and microwave properties

Ferrite/ Composite	Year	Properties	Dimension (mm)	Frequency Band (MHz)	Return Loss (dB)	BW (MHz)	Gain (dB)	Applications
Co ₂ Z/Polyurethane [8]	2020	$\epsilon=6.2, \mu=1.5$ Tan $\delta_e=0.1$, Tan $\delta_m=0.02$	(W=125mm, L=125mm)	402-405	-20.6	30.3	-6.1	Bio-implants
NiCoZn Ferrite compound [7]	2015	$\epsilon=5.11, \mu=5.43$ Tan $\delta_e=0.1$, Tan $\delta_m=0.09$	(W=71mm, L=71mm)	397	-43	29.5	-	For MICS Band applications
Co ₂ Z Ferrite compound [57]	2015	$\epsilon=4.5, \mu=4.6$ Tan $\delta_e=0.02$, Tan $\delta_m=0.05$ Tan $\delta_e=0.1$, Tan $\delta_m=0.09$	(W=44mm, L=38mm)	360	-37	83	-	RF applications
NiCoZn/BFO [11]	2015	$\epsilon=4.5, \mu=4.6$ Tan $\delta_e=0.02$, Tan $\delta_m=0.05$	(W=70mm, L=69mm)	500	-34	30	-	Antenna
BaCo/Silane [85]	2008	$\epsilon=18, \mu=4.2$ Tan $\delta_e=0.26$, Tan $\delta_m=0.14$	(W=49mm, L=49mm)	386	-20.2	5.9	-8.9	RFID

Table 5-13 (Continued)

Present Work	2021	$\epsilon=4.4$, $\mu=2.4$ $\text{Tan}\delta_e=0.00$, $\text{Tan}\delta_m=0.0$ 3	(W=113m m, L=111 mm)	402-407	-27.01	8.1	-0.38	Bio-Implants, NFC-RFID, MICS band and UAV applications
Ferrite/epoxy [86]		$\epsilon=4.18$, $\mu=1.56$ $\text{Tan}\delta_e=0.02$ 2, $\text{Tan}\delta_m=0.0$ 35	(W=110m m, L=50 mm)	748-960	-20	53	-0.03	Mobil e antenn a

5.6 Summary

A performance comparison has been done between the performance of antenna designed and fabricated on a commercial dielectric substrate (Rogers RO3010) and on a magnetic composite (Ni-Co-Zn/epoxy with a 47 vol% ferrite particle loading) substrate using HFSS 3D EM simulations and measurement results. Variation of antenna parameters with substrate thickness and material properties have also been studied for better understanding the correlation of antenna performance with physical parameters and electromagnetic properties. It can be concluded from the results that magneto-dielectric substrates exhibit better performance than that of pure dielectric substrates for the purpose of increasing bandwidth and reducing patch antenna size. To achieve higher antenna gain and efficiency, thicker magnetic composite substrates with strategically chosen ferrite loading volume ratio can be used depending on the application. For example, in biomedical implants, antenna should be designed based on parameters such as antenna size, bandwidth and return loss, while not compromising the antenna gain. Based on the microwave properties and performance of

prototype antenna in this preliminary study, Ni-Co-Zn/epoxy based magnetic substrates have shown great promises as a suitable candidate for biomedical implants, RFID and MICS band antenna applications.

Chapter 6: Conclusion and Future Work

6.1 Conclusion

Ni-Cu-Zn and Ni-Co-Zn ferrite materials have been used for RFID and NFC applications since 2004 because of their superb magnetic and loss properties. This technology is still at its infancy and there are lots of unfilled potentials for wireless sensor and wireless communication applications, which span a wide range of applications in our daily life ranging from electronics to health care (particularly in the form of personalized medicine). There is ongoing research to make RFID and NFC technology more and more affordable, easy to use, as well as more compact in size. There is a strong desire to further increase the efficiency of these wireless devices and systems. The relatively short operation range with a typical distance of communication between RFID and NFC devices limited to few cm's is another problem, which can be mitigated further by increasing resonance frequency of the soft-magnetic ferrite materials and tailoring the magnetic properties at the targeted RFID and NFC operation frequencies.

To prepare a magnetic composite substrate for the aforementioned communication RFID and NFC devices, the synthesized ferrite powders should exhibit high permeability, low magnetic loss (or high Q-factor), which in turn demands strategic optimization of all the key processing parameters detailed in this chapter. For instance, it is very important to retain uniform grain sizes among all ferrite particles in order to make functional Ni-Cu-Zn and Ni-Co-Zn ferrite slurry before introducing organic additives. Until now, fabrication techniques such as tape casting and molding is most widely used for mass production of the magnetic composite substrates. 3-D printing is also an emerging new technique, which can open a new avenue for making thin flexible or conformal

sheets or other three-dimensional components for more future applications such as embedded NFC and RFID chips, as well as biomedical devices such as wearable or implantable medical sensors and body networked communication devices.

6.2 Future Research

Based on the promising results of the present work, the future work should be focused on developing more robust and complicated NFC devices using advanced emerging techniques such as 3-D printing (also known as additive manufacturing). And subsequently, testing those platforms for relevant applications such as biotelemetry for biomedical implants has also attracted a great deal of interests. Here are some of the things that can be explored in near future to further improve the magneto-dielectric properties of the material and explore the applications of Ni-Cu-Zn ferrite materials/sheets:

- Explore the effect of doping materials such as rare earth elements- MoO_3 , WO_3 and IrO_2 on electromagnetic properties of Ni-Co-Zn ferrite powders.
- Explore the effect of new solvents and dispersants for the uniform mixing of ferrite powders and epoxy in magnetic slurry, which in turn enhances the magnetic and dielectric as well as loss properties.
- Conduct more detailed studies on the effect of temperature variation on morphology and electromagnetic properties of Ni-Co-Zn ferrite powders.
- Explore biocompatible epoxies, which can be 3-D printed to form the antenna substrate.
- Develop coil based planar antenna design for biomedical implant application using additive manufacturing techniques.
- Explore photonic curing for the 3-D printed magnetic composite substrates, which can be cured in the presence of externally applied magnetic fields.

Out of so many perspective applications, medical applications are of great interest. Due to rapid advancement in electronic industry, medical field is changing rapidly. The present challenges in medical devices include bulky size, high power consumption and biocompatibility. Currently, most medical devices (testing, diagnostic and implantable devices) use the battery. And due to limited capacity of lithium ion-based batteries, it is not possible to achieve the desired functionality with existing devices and systems. Wireless power/data transfer using RFID and NFC technology can address these problems. High-speed data communication at VHF and UHF frequencies over longer distances can lead to early intervention for various pathologies and make personalized medicine a reality in near future. According to a report issued by Transparency Market Research (TMR), healthcare is the fastest growing part of wireless communications, representing a CAGR of 20.4% [87, 88] .

NFC and RFID based wireless communication provides user friendly benefits in healthcare e.g., secure physical access to buildings, medications and equipment, medical information, real time updates on patient care, medical alerts, home monitoring of patients, safer medications [89-92], storage of encrypted medical tags [93], adverse drugs and allergy detection system in hospitals [94] and electronic data recording services [95]. For example, recently Xiaomi launched Mi Band 5 wrist band, which supports NFC based payments and transactions through the band. Currently, in the time of COVID-19 pandemic, Silicon Craft Technology PLC (SICT) has launched an NFC enabled wearable band to track COVID-19 patients and those are under self-quarantine [96]. There are more complex implementations of NFC technology in wearable and/or implantable health prognostic and prosthesis devices, such as heart monitors [97] and cochlea implants [98-100]. NFC and RFID enabled devices are also employed in fitness and nutrition programs to promote overall health and wellness of users, such as, Apple watch, FitBit, Sony's Smart Band and Samsung

Galaxy watch, etc. There are affirmative studies that focus on improvement of health applications using NFC based wireless communication, such as self-diagnosis and medication, specific applications for the disabled, elderly and people with chronic diseases, and so on [101]. This is just the beginning of wireless communication applications in the healthcare sector, a lot more will follow in coming years. In summary, a multidisciplinary research approach involving material scientists, electrical engineers, and biomedical engineers can lead to development of next generation biomedical wearable diagnostics and implantable devices, while advancing the RFID-NFC wireless sensing and wireless communication applications.

References

- [1] P. Lathiya, J. J. W. P. T. R. D. Wang, Applications, and N. Perspectives, "Near-Field Communications (NFC) for Wireless Power Transfer (WPT): An Overview," 2021.
- [2] D.-W. Seo, J.-H. Lee, H. J. I. J. o. A. Lee, and Propagation, "Integration of resonant coil for wireless power transfer and implantable antenna for signal transfer," vol. 2016, 2016.
- [3] E. Y. Chow, M. M. Morris, and P. P. J. I. M. M. Irazoqui, "Implantable RF medical devices: The benefits of high-speed communication and much greater communication distances in biomedical applications," vol. 14, no. 4, pp. 64-73, 2013.
- [4] R. C. J. P. o. t. I. Hansen, "Fundamental limitations in antennas," vol. 69, no. 2, pp. 170-182, 1981.
- [5] Y. Hwang, Y. Zhang, G. Zheng, and T. K. J. E. L. Lo, "Planar inverted F antenna loaded with high permittivity material," vol. 31, no. 20, pp. 1710-1712, 1995.
- [6] A. K. Skrivervik, J.-F. Zurcher, O. Staub, J. J. I. A. Mosig, and p. Magazine, "PCS antenna design: The challenge of miniaturization," vol. 43, no. 4, pp. 12-27, 2001.
- [7] E. Le Guen, A.-C. Tarot, and J.-L. Mattei, "Half-massive ceramics for antenna downsizing: improvement of a smart magneto-dielectric material with matching permeability and permittivity, and with enhanced low-loss frequency range," in *Antennas and Propagation (EuCAP), 2015 9th European Conference on*, 2015, pp. 1-5: IEEE.
- [8] S.-E. Lee, S. P. Choi, K.-S. Oh, J. Kim, S. M. Lee, and K. R. J. M. Cho, "Flexible Magnetic Polymer Composite Substrate with Ba_{1.5}Sr_{1.5}Z Hexaferrite Particles of VHF/Low UHF Patch Antennas for UAVs and Medical Implant Devices," vol. 13, no. 4, p. 1021, 2020.
- [9] K. Han *et al.*, "Magneto-dielectric nanocomposite for antenna miniaturization and SAR reduction," vol. 15, pp. 72-75, 2015.
- [10] G. Gan *et al.*, "Low loss, enhanced magneto-dielectric properties of Bi₂O₃ doped Mg-Cd ferrites for high frequency antennas," vol. 735, pp. 2634-2639, 2018.

- [11] A. Saini, K. Rana, A. Thakur, P. Thakur, J. L. Mattei, and P. J. M. R. B. Queffelec, "Low loss composite nano ferrite with matching permittivity and permeability in UHF band," vol. 76, pp. 94-99, 2016.
- [12] E. Le Guen, A.-C. Tarot, and J.-L. Mattei, "Half-massive ceramics for antenna downsizing: improvement of a smart magneto-dielectric material with matching permeability and permittivity, and with enhanced low-loss frequency range," in *2015 9th European Conference on Antennas and Propagation (EuCAP)*, 2015, pp. 1-5: IEEE.
- [13] R. J. I. p. c. Want, "An introduction to RFID technology," vol. 5, no. 1, pp. 25-33, 2006.
- [14] H.-J. Kim, H. Hirayama, S. Kim, K. J. Han, R. Zhang, and J.-W. J. I. A. Choi, "Review of near-field wireless power and communication for biomedical applications," vol. 5, pp. 21264-21285, 2017.
- [15] L. Atzori, A. Iera, and G. Morabito, "The Internet of Things: A survey Comput. Netw," 2010.
- [16] M. Y. ZARE, "RFID: a bibliographical literature review with future research directions," 2014.
- [17] W. Suparta, "Application of near field communication technology for mobile airline ticketing," vol. 8, no. 8, p. 1235, 2012.
- [18] R. Want, "An introduction to RFID technology," no. 1, pp. 25-33, 2006.
- [19] M. Gebhart, R. Neubauer, M. Stark, and D. Warnez, "Design of 13.56 MHz smartcard stickers with ferrite for payment and authentication," in *Near Field Communication (NFC), 2011 3rd International Workshop on*, 2011, pp. 59-64: IEEE.
- [20] S. Yan, W. Liu, Z. Chen, Y. Nie, X. Wang, and Z. Feng, "Preparation and characterization of ferrite with Co substituted NiCuZn sheets application for 13.56 MHz radio frequency identification communication," *Journal of Applied Physics*, vol. 115, no. 17, p. 17A529, 2014.
- [21] W. Lee *et al.*, "A simple wireless power charging antenna system: Evaluation of ferrite sheet," *IEEE Transactions on Magnetics*, vol. 53, no. 7, pp. 1-5, 2017.
- [22] C. Stergiou, E. Eleftheriou, and V. Zaspalis, "Enhancement of the near-field UHF RFID with ferrite substrates," *IEEE Transactions on Magnetics*, vol. 48, no. 4, pp. 1497-1500, 2012.

- [23] H.-P. Huang, C.-S. Chen, and T.-Y. Chen, "Mobile diagnosis based on RFID for food safety," in *2006 IEEE International Conference on Automation Science and Engineering*, 2006, pp. 357-362: IEEE.
- [24] K. Finkenzeller, *RFID handbook: fundamentals and applications in contactless smart cards, radio frequency identification and near-field communication*. John wiley & sons, 2010.
- [25] S. Atluri and M. Ghovanloo, "Design of a wideband power-efficient inductive wireless link for implantable biomedical devices using multiple carriers," in *Conference Proceedings. 2nd International IEEE EMBS Conference on Neural Engineering, 2005.*, 2005, pp. 533-537: IEEE.
- [26] B. Lee, B. Kim, F. J. Harackiewicz, B. Mun, and H. Lee, "NFC antenna design for low-permeability ferromagnetic material," *IEEE Antennas Wireless Propagation Letters*, vol. 13, pp. 59-62, 2014.
- [27] P. Lathiya, M. Kreuzer, J. J. J. o. M. Wang, and M. Materials, "RF complex permeability spectra of Ni-Cu-Zn ferrites prepared under different applied hydraulic pressures and durations for wireless power transfer (WPT) applications," vol. 499, p. 166273, 2020.
- [28] P. Lathiya and J. Wang, "Influence of Hydraulic Pressure on Dynamic Magnetic Properties of Ni–Cu–Zn Ferrites," *IEEE Magnetics Letters*, vol. 10, pp. 1-5, 2019.
- [29] J. Shrotri *et al.*, "Effect of Cu substitution on the magnetic and electrical properties of Ni–Zn ferrite synthesised by soft chemical method," *Materials Chemistry Physics*, vol. 59, no. 1, pp. 1-5, 1999.
- [30] P. Lathiya and J. J. I. T. o. M. Wang, "Effects of the sintering temperature on RF complex permeability of NiCuCoZn ferrites for near-field communication applications," vol. 55, no. 2, pp. 1-4, 2018.
- [31] P. Lathiya and J. J. J. o. t. A. C. S. Wang, "Enhancement in magnetic permeability of Ni-Co-Zn ferrites using CuO doping for RF and microwave devices," vol. 105, no. 4, pp. 2678-2689, 2022.
- [32] A. Paduraru, M. Feder, and O. Caltun, "Magnetic properties of some permivar ferrites," *Journal of Optoelectronics Advanced Materials*, vol. 5, no. 4, pp. 945-950, 2003.
- [33] F. Xie, Y. Chen, M. Bai, and P. Wang, "Co-substituted LiZnTiBi ferrite with equivalent permeability and permittivity for high-frequency miniaturized antenna application," *Ceramics International*, vol. 45, no. 14, pp. 17915-17919, 2019.

- [34] Y. Shirakata, N. Hidaka, M. Ishitsuka, A. Teramoto, and T. Ohmi, "High permeability and low loss Ni–Fe composite material for high-frequency applications," *IEEE Transactions on Magnetics*, vol. 44, no. 9, pp. 2100-2106, 2008.
- [35] L. Kong, Z. Li, G. Lin, and Y. Gan, "Ni-Zn ferrites composites with almost equal values of permeability and permittivity for low-frequency antenna design," *IEEE Transactions on Magnetics*, vol. 43, no. 1, pp. 6-10, 2006.
- [36] M. Drogenik, A. Znidarsic, and D. Makovec, "Influence of the addition of Bi₂O₃ on the grain growth and magnetic permeability of MnZn ferrites," *Journal of the American Ceramic Society*, vol. 81, no. 11, pp. 2841-2848, 1998.
- [37] P. Gelin, P. Quéffélec, and F. Le Pennec, "Effect of domain and grain shapes on the dynamical behavior of polycrystalline ferrites: Application to the initial permeability," *Journal of Applied Physics*, vol. 98, no. 5, p. 053906, 2005.
- [38] J. Bouchaud and P. Zerah, "The initial susceptibility of ferrites: A quantitative theory," *Journal of Applied Physics*, vol. 67, no. 9, pp. 5512-5514, 1990.
- [39] T. Nakamura, "Snoek's limit in high-frequency permeability of polycrystalline Ni–Zn, Mg–Zn, and Ni–Zn–Cu spinel ferrites," *Journal of Applied Physics*, vol. 88, no. 1, pp. 348-353, 2000.
- [40] J. Snoek, "Dispersion and absorption in magnetic ferrites at frequencies above one Mc/s," *Physica*, vol. 14, no. 4, pp. 207-217, 1948.
- [41] N. Abu-Elsaad, A. Nawara, and S. Mazen, "Synthesis, structural characterization, and magnetic properties of Ni–Zn nanoferrites substituted with different metal ions (Mn²⁺, Co²⁺, and Cu²⁺)," *Journal of Physics Chemistry of Solids*, p. 109620, 2020.
- [42] S. J. Kumar, P. Prameela, K. S. Rao, J. Kiran, and K. Rao, "Structural and Magnetic Properties of Copper-Substituted Nickel–Zinc Nanoparticles Prepared by Sol-Gel Method," *Journal of Superconductivity Novel Magnetism*, vol. 33, no. 3, pp. 693-705, 2020.
- [43] Z. Zheng, Y. Li, T. Liu, and Q. Feng, "Novel high-frequency magneto-dielectric properties of CaO–SiO₂ Co-doped NiZnCo spinel ferrites for RF and microwave device applications," *IEEE Transactions on Magnetics*, vol. 54, no. 11, pp. 1-4, 2018.
- [44] C. Stergiou, "Magnetic, dielectric and microwave absorption properties of rare earth doped Ni–Co and Ni–Co–Zn spinel ferrites," *Journal of Magnetism Magnetic Materials*, vol. 426, pp. 629-635, 2017.

- [45] Q. Li, Y. Chen, and V. G. Harris, "Particle-size distribution modified effective medium theory and validation by magneto-dielectric Co-Ti substituted BaM ferrite composites," *Journal of Magnetism Magnetic Materials*, vol. 453, pp. 44-47, 2018.
- [46] Z. Su *et al.*, "Low loss factor Co₂Z ferrite composites with equivalent permittivity and permeability for ultra-high frequency applications," *Applied Physics Letters*, vol. 105, no. 6, p. 062402, 2014.
- [47] Z. Zheng, Q. Feng, and V. G. Harris, "Low-loss Z-type barium hexaferrite composites from nanoscale ZnAl₂O₄ addition for high-frequency applications," *AIP Advances*, vol. 8, no. 5, p. 056107, 2018.
- [48] Z. Zheng, Q. Feng, Y. Chen, and V. G. Harris, "High-frequency magnetic properties of Ca-substituted Co₂Z and Co₂W barium hexaferrite composites," *IEEE Transactions on Magnetics*, vol. 54, no. 6, pp. 1-6, 2018.
- [49] T. Y. Byun, S. C. Byeon, K. S. Hong, and C. K. Kim, "Factors affecting initial permeability of Co-substituted Ni-Zn-Cu ferrites," *IEEE Transactions on Magnetics*, vol. 35, no. 5, pp. 3445-3447, 1999.
- [50] S. B. Waje, M. Hashim, and I. Ismail, "Effects of sintering temperature on grain growth and the complex permeability of Co_{0.2}Ni_{0.3}Zn_{0.5}Fe₂O₄ material prepared using mechanically alloyed nanoparticles," *Journal of Magnetism Magnetic Materials*, vol. 323, no. 11, pp. 1433-1439, 2011.
- [51] S. Kumar, T. Shinde, and P. Vasambekar, "Engineering High Permeability: M_n-Z_n and Ni-Z_n Ferrites," *International Journal of Applied Ceramic Technology*, vol. 12, no. 4, pp. 851-859, 2015.
- [52] T. J. J. o. C. S. AlSharabati and Systems, "Microstrip Patch Antenna Miniaturization Using Magneto-Dielectric Substrates for Electromagnetic Energy Harvesting," vol. 17, no. 2, pp. 116-123, 2021.
- [53] Z. Zheng and X. J. I. T. o. M. Wu, "A miniaturized UHF Vivaldi antenna with tailored radiation performance based on magneto-dielectric ferrite materials," vol. 56, no. 3, pp. 1-5, 2020.
- [54] Z. Luan, L. Liu, W.-H. Zong, Z. Jin, and S. J. P. I. E. R. L. Li, "Design of an Implantable Antenna Operating at ISM Band Using Magneto-Dielectric Material," vol. 82, pp. 65-72, 2019.

- [55] E. Koohkan, S. Naimolhoda, and M. Bod, "A Miniaturized Tunable Blade Antenna for UHF Frequencies," in *2019 27th Iranian Conference on Electrical Engineering (ICEE)*, 2019, pp. 1461-1464: IEEE.
- [56] J. Kim *et al.*, "A wireless power transfer based implantable ECG monitoring device," vol. 13, no. 4, p. 905, 2020.
- [57] Z. Chen *et al.*, "UHF tunable compact antennas on Co₂Z hexaferrite substrate with 2.5/1 tunable frequency range," in *2015 IEEE International Symposium on Antennas and Propagation & USNC/URSI National Radio Science Meeting*, 2015, pp. 2287-2288: IEEE.
- [58] L. Mo, C. J. I. J. o. A. Qin, and Propagation, "Tunable compact UHF RFID metal tag based on CPW open stub feed PIFA antenna," vol. 2012, 2012.
- [59] J. Jeong, Y. H. Han, and B. C. Moon, "Effects of Bi₂O₃ addition on the microstructure and electromagnetic properties of NiCuZn ferrites," *Journal of Materials Science: Materials in Electronics*, vol. 15, no. 5, pp. 303-306, 2004.
- [60] P. Lathiya and J. Wang, "Effects of the Sintering Temperature on RF Complex Permeability of NiCuCoZn Ferrites for Near-Field Communication Applications," *IEEE Transactions on Magnetics*, vol. 55, no. 2, pp. 1-4, 2018.
- [61] W. Lee *et al.*, "A simple wireless power charging antenna system: Evaluation of ferrite sheet," *IEEE Transactions on Magnetics*, vol. 53, no. 7, pp. 1-5, 2017.
- [62] B. P. Rao, C.-O. Kim, and C. J. M. L. Kim, "Influence of V₂O₅ additions on the permeability and power loss characteristics of Ni–Zn ferrites," vol. 61, no. 7, pp. 1601-1604, 2007.
- [63] K. Sun, Z. Lan, Z. Yu, L. Li, J. Huang, and X. Zhao, "Grain growth, densification and magnetic properties of NiZn ferrites with Bi₂O₃ additive," *Journal of Physics D: Applied Physics*, vol. 41, no. 23, p. 235002, 2008.
- [64] K. Kawano, M. Hachiya, Y. Iijima, N. Sato, Y. J. J. o. M. Mizuno, and M. materials, "The grain size effect on the magnetic properties in NiZn ferrite and the quality factor of the inductor," vol. 321, no. 16, pp. 2488-2493, 2009.
- [65] T. Tsutaoka, "Frequency dispersion of complex permeability in Mn–Zn and Ni–Zn spinel ferrites and their composite materials," *Journal of Applied Physics*, vol. 93, no. 5, pp. 2789-2796, 2003.

- [66] S. Kumar, T. Shinde, and P. Vasambekar, "Engineering High Permeability: Mn–Zn and Ni–Zn Ferrites," *International Journal of Applied Ceramic Technology*, vol. 12, no. 4, pp. 851-859, 2015.
- [67] T. Nakamura and M. Materials, "Low-temperature sintering of NiZnCu ferrite and its permeability spectra," *Journal of Magnetism Magnetic Materials*, vol. 168, no. 3, pp. 285-291, 1997.
- [68] B. P. Rao and K. Rao, "Effect of sintering conditions on resistivity and dielectric properties of Ni-Zn ferrites," *Journal of Materials Science*, vol. 32, no. 22, pp. 6049-6054, 1997.
- [69] H. Su, X. Tang, H. Zhang, L. Jia, and Z. Zhong, "Influences of Bi₂O₃ additive on the microstructure, permeability, and power loss characteristics of Ni–Zn ferrites," *Journal of Magnetism Magnetic Materials*, vol. 321, no. 19, pp. 3183-3186, 2009.
- [70] X. Wu, S. Yan, W. Liu, Z. Feng, Y. Chen, and V. G. Harris, "Influence of particle size on the magnetic spectrum of NiCuZn ferrites for electromagnetic shielding applications," *Journal of Magnetism and Magnetic Materials*, vol. 401, pp. 1093-1096, 2016.
- [71] TDK, "Magnetic sheets for RFID," *IFL/IBF series datasheet*, June 2016.
- [72] Laird, "Flexible ferrite sheets for NFC & wireless charging," *MCP-DSMHLL datasheet*, August 2014.
- [73] S. Yan, L. Deng, Z. Feng, J. He, Y. Li, and M. Hu, "Effect of Co₂O₃ Addition on Stability of Permeability to an Impulse Magnetic Field in NiCuZn Ferrites," *IEEE Transactions on Magnetics*, vol. 53, no. 8, pp. 1-4, 2017.
- [74] C. Clausell, A. Barba, L. Nuño, and J. C. Jarque, "Effect of average grain size and sintered relative density on the imaginary part- μ'' of the complex magnetic permeability of (Cu_{0.12}Ni_{0.23}Zn_{0.65})Fe₂O₄ system," *Ceramics International*, vol. 42, no. 3, pp. 4256-4261, 2016.
- [75] W. Shen, H. Zhu, Y. Jin, H. Zhou, and Z. Xu, "Sintering, microstructure and magnetic properties of low-temperature-fired NiCuZn ferrites doped with B₂O₃," *Ceramics International*, vol. 40, no. 7, pp. 9205-9209, 2014.
- [76] M. F. Yan, R. Cannon Jr, H. Bowen, U. J. M. s. Chowdhry, and engineering, "Effect of grain size distribution on sintered density," vol. 60, no. 3, pp. 275-281, 1983.
- [77] A. Taghvaei, H. Shokrollahi, M. Ghaffari, K. J. J. o. P. Janghorban, and C. o. Solids, "Influence of particle size and compaction pressure on the magnetic properties of iron-phenolic soft magnetic composites," vol. 71, no. 1, pp. 7-11, 2010.


- [78] H. Igarashi and K. Okazaki, "Effects of porosity and grain size on the magnetic properties of NiZn ferrite," *Journal of the American Ceramic Society*, vol. 60, no. 1-2, pp. 51-54, 1977.
- [79] M. Molaahmadi, S. Baghshahi, and A. Ghasemi, "Effect of Cu 2+ substitution on structural and magnetic properties of Ni–Zn ferrite nanopowders," *Journal of Materials Science: Materials in Electronics*, vol. 27, no. 11, pp. 11447-11456, 2016.
- [80] A. Globus, "Magnetization Mechanismssome Physical Considerations About the Domain Wall Size Theory of Magnetization Mechanisms," *Le Journal de Physique Colloques*, vol. 38, no. C1, pp. C1-1-C1-15, 1977.
- [81] T. Tsutaoka, T. Nakamura, and K. Hatakeyama, "Magnetic field effect on the complex permeability spectra in a Ni–Zn ferrite," *Journal of Applied Physics*, vol. 82, no. 6, pp. 3068-3071, 1997.
- [82] Q. Li, Y. Chen, C. Yu, K. Qian, and V. G. Harris, "Permeability spectra of planar M-type barium hexaferrites with high Snoek's product by two-step sintering," *Journal of the American Ceramic Society*, 2020.
- [83] A. Barba, C. Clausell, J. Jarque, and L. Nuño, "Magnetic complex permeability (imaginary part) dependence on the microstructure of a Cu-doped Ni–Zn-polycrystalline sintered ferrite," *Ceramics International*, vol. 46, no. 10, pp. 14558-14566, 2020.
- [84] H. Su, H. Zhang, X. Tang, Y. Jing, and Z. Zhong, "Complex permeability and permittivity spectra of polycrystalline Ni–Zn ferrite samples with different microstructures," *Journal of Alloys Compounds*, vol. 481, no. 1-2, pp. 841-844, 2009.
- [85] L. J. Martin, *Flexible magnetic composite for antenna applications in radio frequency identification (RFID)*. Georgia Institute of Technology, 2008.
- [86] B.-Y. Park, M.-H. Jeong, S.-O. J. I. A. Park, and W. P. Letters, "A magneto-dielectric handset antenna for LTE/WWAN/GPS applications," vol. 13, pp. 1482-1485, 2014.
- [87] C. Ardila. (November 18, 2015). *Six ways NFC Helps Healthcare*. Available: <https://www.nxp.com/company/blog/six-ways-nfc-helps-healthcare:BL-6-WAYS-NFC-HELPS-HEALTHCARE>
- [88] T. M. Research. (August 01, 2017). *INCREASED DEMAND FOR SAFETY AND SECURITY BOOSTS ACCESS CONTROL AND AUTHENTICATION MARKET*.


- [89] J. Fontecha, R. Hervás, J. Bravo, and V. Villarreal, "An NFC approach for nursing care training," in *2011 Third International Workshop on Near Field Communication*, 2011, pp. 38-43: IEEE.
- [90] A. Marcus *et al.*, "Using NFC-enabled mobile phones for public health in developing countries," in *2009 First International Workshop on Near Field Communication*, 2009, pp. 30-35: IEEE.
- [91] R. Iglesias, J. Parra, C. Cruces, and N. G. de Segura, "Experiencing NFC-based touch for home healthcare," in *Proceedings of the 2nd international conference on pervasive technologies related to assistive environments*, 2009, pp. 1-4.
- [92] J. Bravo *et al.*, "Touch-based interaction: An approach through NFC," in *2007 3rd IET International Conference on Intelligent Environments*, 2007, pp. 440-446: IET.
- [93] S. Dunnebeil, F. Kobler, P. Koene, J. M. Leimeister, and H. Krcmar, "Encrypted NFC emergency tags based on the German telematics infrastructure," in *2011 Third International Workshop on Near Field Communication*, 2011, pp. 50-55: IEEE.
- [94] A. J. Jara, A. F. Alcolea, M. Zamora, A. G. Skarmeta, and M. Alsaedy, "Drugs interaction checker based on IoT," in *2010 Internet of Things (IOT)*, 2010, pp. 1-8: IEEE.
- [95] J. Morak, D. Hayn, P. Kastner, M. Drobics, and G. Schreier, "Near field communication technology as the key for data acquisition in clinical research," in *2009 First International Workshop on Near Field Communication*, 2009, pp. 15-19: IEEE.
- [96] A. Hegde. (December 28, 2020). *NFC Latest Trends 2021: 7 NFC Technology Trends to Watch Out for!* Available: <https://blog.beaconstac.com/2020/10/nfc-latest-trends/>
- [97] A. J. Jara, P. López, D. Fernández, B. Úbeda, M. A. Zamora, and A. F. Skarmeta, "Heart monitoring system based on NFC for continuous analysis and pre-processing of wireless vital signs," in *Proc. Int. Conf. Health Informatics (HEALTHINF)*, 2012.
- [98] M. Yip, A. Chandrakasan, and K. Stankovic, "Low power cochlear implants," ed: Google Patents, 2018.
- [99] G. Erráez Castelltort, "Design of an electrical nerve stimulator using wireless power transmission through NFC," Universitat Politècnica de Catalunya, 2018.
- [100] P. Bazard, R. D. Frisina, J. P. Walton, and V. R. J. S. r. Bhethanabotla, "Nanoparticle-based plasmonic transduction for modulation of electrically excitable cells," vol. 7, no. 1, pp. 1-13, 2017.

- [101] V. Coskun, B. Ozdenizci, and K. J. S. Ok, "The survey on near field communication," vol. 15, no. 6, pp. 13348-13405, 2015.

Appendix A: Copyright Permissions

The permission below is for the use of published content in Chapter 3, Section 3.2, 3.3, 3.4 and 3.5.

Home ? Email Support Sign in Create Account



Requesting permission to reuse content from an IEEE publication

Effects of the Sintering Temperature on RF Complex Permeability of NiCuCoZn Ferrites for Near-Field Communication Applications
Author: Poonam Lathiya
Publication: IEEE Transactions on Magnetics
Publisher: IEEE
Date: Feb. 2019
Copyright © 2019, IEEE

Thesis / Dissertation Reuse

The IEEE does not require individuals working on a thesis to obtain a formal reuse license, however, you may print out this statement to be used as a permission grant:

Requirements to be followed when using any portion (e.g., figure, graph, table, or textual material) of an IEEE copyrighted paper in a thesis:

- 1) In the case of textual material (e.g., using short quotes or referring to the work within these papers) users must give full credit to the original source (author, paper, publication) followed by the IEEE copyright line © 2011 IEEE.
- 2) In the case of illustrations or tabular material, we require that the copyright line © [Year of original publication] IEEE appear prominently with each reprinted figure and/or table.
- 3) If a substantial portion of the original paper is to be used, and if you are not the senior author, also obtain the senior author's approval.

Requirements to be followed when using an entire IEEE copyrighted paper in a thesis:


- 1) The following IEEE copyright/ credit notice should be placed prominently in the references: © [Year of original publication] IEEE. Reprinted, with permission, from [author names, paper title, IEEE publication title, and month/year of publication]
- 2) Only the accepted version of an IEEE copyrighted paper can be used when posting the paper or your thesis on-line.
- 3) In placing the thesis on the author's university website, please display the following message in a prominent place on the website: In reference to IEEE copyrighted material which is used with permission in this thesis, the IEEE does not endorse any of [university/educational entity's name goes here]'s products or services. Internal or personal use of this material is permitted. If interested in reprinting/republishing IEEE copyrighted material for advertising or promotional purposes or for creating new collective works for resale or redistribution, please go to http://www.ieee.org/publications_standards/publications/rights/rights_link.html to learn how to obtain a License from RightsLink.


If applicable, University Microfilms and/or ProQuest Library, or the Archives of Canada may supply single copies of the dissertation.

BACK

CLOSE WINDOW

© 2022 Copyright - All Rights Reserved | Copyright Clearance Center, Inc. | Privacy statement | Terms and Conditions
Comments? We would like to hear from you. Email us at customer-care@copyright.com

Home ? Email Support Poonam Lathiya



Requesting permission to reuse content from an IEEE publication

Influence of Hydraulic Pressure on Dynamic Magnetic Properties of Ni-Cu-Zn Ferrites
Author: Poonam Lathiya
Publication: IEEE Magnetics Letters
Publisher: IEEE
Date: 2019
Copyright © 2019, IEEE

Thesis / Dissertation Reuse

The IEEE does not require individuals working on a thesis to obtain a formal reuse license, however, you may print out this statement to be used as a permission grant:

Requirements to be followed when using any portion (e.g., figure, graph, table, or textual material) of an IEEE copyrighted paper in a thesis:

- 1) In the case of textual material (e.g., using short quotes or referring to the work within these papers) users must give full credit to the original source (author, paper, publication) followed by the IEEE copyright line © 2011 IEEE.
- 2) In the case of illustrations or tabular material, we require that the copyright line © [Year of original publication] IEEE appear prominently with each reprinted figure and/or table.
- 3) If a substantial portion of the original paper is to be used, and if you are not the senior author, also obtain the senior author's approval.

Requirements to be followed when using an entire IEEE copyrighted paper in a thesis:

- 1) The following IEEE copyright/ credit notice should be placed prominently in the references: © [Year of original publication] IEEE. Reprinted, with permission, from [author names, paper title, IEEE publication title, and month/year of publication]
- 2) Only the accepted version of an IEEE copyrighted paper can be used when posting the paper or your thesis on-line.
- 3) In placing the thesis on the author's university website, please display the following message in a prominent place on the website: In reference to IEEE copyrighted material which is used with permission in this thesis, the IEEE does not endorse any of [university/educational entity's name goes here]'s products or services. Internal or personal use of this material is permitted. If interested in reprinting/republishing IEEE copyrighted material for advertising or promotional purposes or for creating new collective works for resale or redistribution, please go to http://www.ieee.org/publications_standards/publications/rights/rights_link.html to learn how to obtain a License from RightsLink.

If applicable, University Microfilms and/or ProQuest Library, or the Archives of Canada may supply single copies of the dissertation.

BACK

CLOSE WINDOW

© 2022 Copyright - All Rights Reserved | Copyright Clearance Center, Inc. | Privacy statement | Terms and Conditions
Comments? We would like to hear from you. Email us at customer-care@copyright.com



RF complex permeability spectra of Ni-Cu-Zn ferrites prepared under different applied hydraulic pressures and durations for wireless power transfer (WPT) applications

Author: Poonam Lathiya, Marcel Kreuzer, Jing Wang
 Publication: Journal of Magnetism and Magnetic Materials
 Publisher: Elsevier
 Date: 1 April 2020

© 2019 Elsevier B.V. All rights reserved.

Journal Author Rights

Please note that, as the author of this Elsevier article, you retain the right to include it in a thesis or dissertation, provided it is not published commercially. Permission is not required, but please ensure that you reference the journal as the original source. For more information on this and on your other retained rights, please visit: <https://www.elsevier.com/about/our-business/policies/copyright#Author-rights>

BACK

CLOSE WINDOW

The permission below is for the use of published content in Chapter 4, Section 4.2.



Enhancement in magnetic permeability of Ni-Co-Zn ferrites using CuO doping for RF and microwave devices

Author: Poonam Lathiya, Jing Wang
 Publication: Journal of the American Ceramic Society
 Publisher: John Wiley and Sons
 Date: Dec 7, 2021

© 2021 The American Ceramic Society

Order Completed

Thank you for your order.

This Agreement between University of south florida - Poonam Lathiya ("You") and John Wiley and Sons ("John Wiley and Sons") consists of your license details and the terms and conditions provided by John Wiley and Sons and Copyright Clearance Center.

Your confirmation email will contain your order number for future reference.

License Number: 5265610343704
 License date: Mar 10, 2022

Printable Details

Licensed Content

Licensed Content Publisher: John Wiley and Sons
 Licensed Content Publication: Journal of the American Ceramic Society
 Licensed Content Title: Enhancement in magnetic permeability of Ni-Co-Zn ferrites using CuO doping for RF and microwave devices
 Licensed Content Author: Poonam Lathiya, Jing Wang
 Licensed Content Date: Dec 7, 2021
 Licensed Content Volume: 105
 Licensed Content Issue: 4
 Licensed Content Pages: 12

Order Details

Type of use: Dissertation/Thesis
 Requestor type: Author of this Wiley article
 Format: Electronic
 Portion: Full article
 Will you be translating?: No

About Your Work

Title: Soft Magnetic Composite Substrates for RF/Microwave Applications
 Institution name: University of South Florida
 Expected presentation date: Apr 2022

Additional Data